Precision Mass Measurements of Selected Isotopes of Platinum.

A Thesis
Submitted to the Faculty of Graduate Studies
University of Manitoba

In partial fulfillment
Of the Requirements for the Degree
Doctor of Philosophy

by
Joseph V. F. Vaz
Winnipeg, Canada

THE UNIVERSITY OF MANITOBA

FACULTY OF GRADUATE STUDIES
*****
COPYRIGHT PERMISSION

Precision Mass Measurements of Selected Isotopes of Platinum

BY

Joseph V.F. Vaz

A Thesis/Practicum submitted to the Faculty of Graduate Studies of The University of

Manitoba in partial fulfillment of the requirement of the degree

of

DOCTOR OF PHILOSOPHY

Joseph V.F. Vaz © 2002

Abstract

A systematic study of atomic masses in the A=180 to A=200 range was undertaken by the University of Manitoba, Atomic Mass Determinations (AMD) Group during the early 1990's. The absence of a large body of mass spectrometric data in this region gives rise to obvious discrepancies in the published mass data. A case of this is the "Mercury (Hg) problem". Mass measurements done on four Platinum isotopes in this body of work will help set "boundary markers" in that region (A~200).

This thesis describes work done on the Manitoba II High Resolution deflection spectrometer as well as the Canadian Penning Trap Mass Spectrometer (CPTMS), sited at Argonne National Laboratory, Illinois, USA. The Platinum (Pt) absolute mass measurements performed with the CPTMS uses the technique of radio frequency (RF) excitation of ion resonant frequencies compared to the Manitoba II, a "classical" deflection machine, employing static electric/magnetic fields to effect ion trajectories. The masses of the four Platinum isotopes have been determined to a precision of 20 parts per billion (ppb). These results are linked to Hg data from Manitoba II form a detailed mass spectroscopic evaluation series for the A=194-204 region. A new mass value for ^{197}Au is also computed.

Various systematic effects in the CPTMS have been examined and a blueprint for a thrust towards even higher precision work has been developed. These measurements also provide a test platform to ascertain the higher end precision possible through the implementation of several novel techniques/devices. This is in anticipation of a planned series of high-precision online mass measurements of very short-lived nuclei.

Acknowledgements

The Atomic Mass Determinations (AMD) Group

Barber, R. C., Barillari, D. K., Duckworth, H. E., Sharma, K. S., Vaz, J. V.

The Canadian Penning Trap (CPT) Collaboration

UNIVERSITY OF MANITOBA
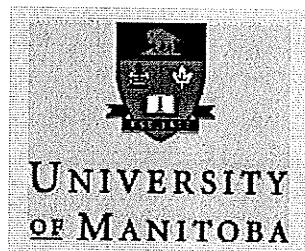
Barber, R. C., Clark, J. A., Fukutani, H., Sharma, K. S., Vaz, J. V and Wang, J.C.

McGill

Boudreau, C., Buchinger, F., Crawford, J., Lee, J. K. P, Moore, R. and Gulick, S.,

ANL Physics Division

Savard, G., Schwartz, J., Heinz, A., Caggiano, J. A., Sewernyniak, D.,

Hardy, J.

Contents

List of Figures

Chapter 4.

Chapter 5.

Chapter 6.

Chapter 7.

Chapter 8.

Appendix A1.

List of Tables

Chapter 8. (tables only appear in Chapter 8)

1. Introduction

The pursuit of knowledge in nuclear physics deals with understanding the fundamental nature of matter. The "atom" has long been considered the basic building block. Democritus, a Greek philosopher in the fourth century B. C. postulated that all matter could be dissected until an indivisible unit is attained. This unit, invisible to the naked eye, was termed the "atom". For centuries this remained just a speculation. Scientists of every era tried to understand the properties of the multitude of existing elements, and relate them to fundamental differences in their basic structure. In the nineteenth century, with Mendeleev's periodic table, the elements were first classified in a systematic manner. Human curiosity continued to probe the "atom" further to reveal the existence of even smaller units, the charged proton, electron and the neutral neutron. The indivisible atom had been divided and shown to consist of a distinct combination of numbers of protons, neutrons and electrons. This systematic picture is illustrated in the chart of nuclides, where the different elements are arranged in order of ascending numbers of N (neutron number) and Z (proton number).
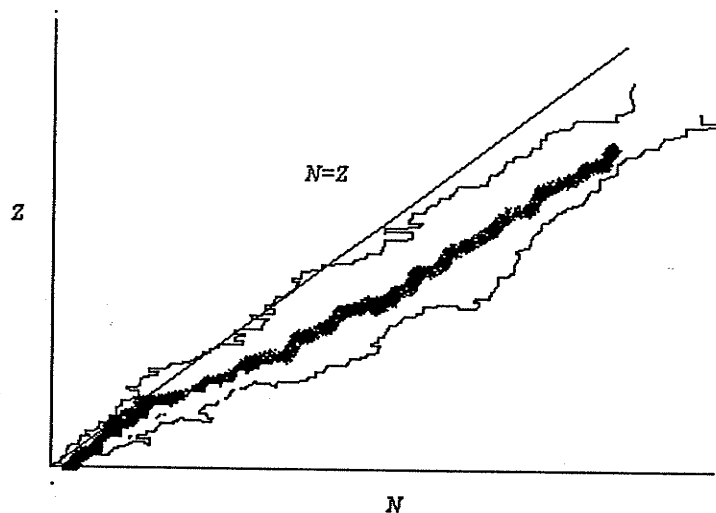
Fig. 1.1. Chart of nuclides. The line of β stability is the shaded region.

This chart (Fig 1.1) reveals interesting nuclear facts at a glance. The instability (extremely short lifetimes) becomes more pronounced for "exotic" elements further from the "valley of stability". The line N=Z is added for further clarity. The line of β-stability can be observed to deviate from $N=Z$ at $N=Z=20$. Thus no stable nuclides that have equal numbers of protons and neutrons exist after $^{40}_{20}Ca$. The heaviest stable nuclide is $^{209}_{83}Bi$, all heavier elements undergo spontaneous fission, breaking apart into two or more smaller components. There is expected to be an island of "superheavy" elements around the N+Z=A≈300.

A small but finite fission barrier provides the necessary stability. There exist pockets of deformed nuclides in various regions where nuclear shapes deviate from being spherical. These "nuclear traits" arise for specific combination of the numbers of neutrons and protons in the various nuclei. The binding energy (B.E) that is the "mass difference" between the bound nucleus $m_N\left(_Z^A X\right)$ and the free protons m_p and neutrons m_n (masses and rest masses are related and used interchangeably):

$$B.E = Zm_p + (A-Z)m_n - m_N\left(_Z^A X\right). \tag{1.0}$$

The commonly used "binding energy per nucleon" is therefore merely $B.E/A$. A positive binding energy denotes stability, as energy input is required to break apart the nucleus. It is the reverse for instability, as now the nucleus will attain a lower energy state by breaking apart through some form of spontaneous decay process. Mapping of the binding energy is thus a probe to understanding nuclear structure. One method of this is through direct atomic mass measurements $m_{atomic}\left(_Z^A X\right)$:

$$m_N\left(_Z^A X\right) = m_{Atomic}\left(_Z^A X\right) - Zm_e + \sum_{i=1}^{Z} B_i \tag{1.1}$$

B_i denotes the electron binding energy of the ith electron. The mass of the nucleus can be extracted from the atomic mass, corrected for the mass and binding energy of the atomic electrons (Duckworth 1990).

Theoretical models serve as bases to explain the variation of binding energies according to the (N, Z) dependence. The variety of different models use the currently available mass data from direct mass determinations or from reaction Q-value measurements to check correspondence in the aim of extending the models to regions far from stability. The terms reflect possible modes of attraction/repulsion between nucleons. The simplest model is the "semi empirical" mass formula. In this scheme, the nucleus is described as a configuration of particles interacting primarily with a short ranged nuclear attraction and a long ranged Coulomb repulsion. The remaining terms reflect some aspects in the pairing/symmetry in neutron/proton number. Other models with more elaborate parametrization techniques exist in a similar spirit- the pursuit of a comprehensive theoretical description that is valid over the entire mass surface!

The very successful Shell Model, borrowing ideas from atomic physics, describes the nucleus as an ever-increasing layer of "shells". Sequential filling of the shells leads to the "magic numbers", which demarcate the various shell levels. Separate shells for neutrons and protons provide for "doubly magic" nuclei, which possess closed shells for both neutrons and protons. This model had its humble beginnings with the phenomenological harmonic oscillator.
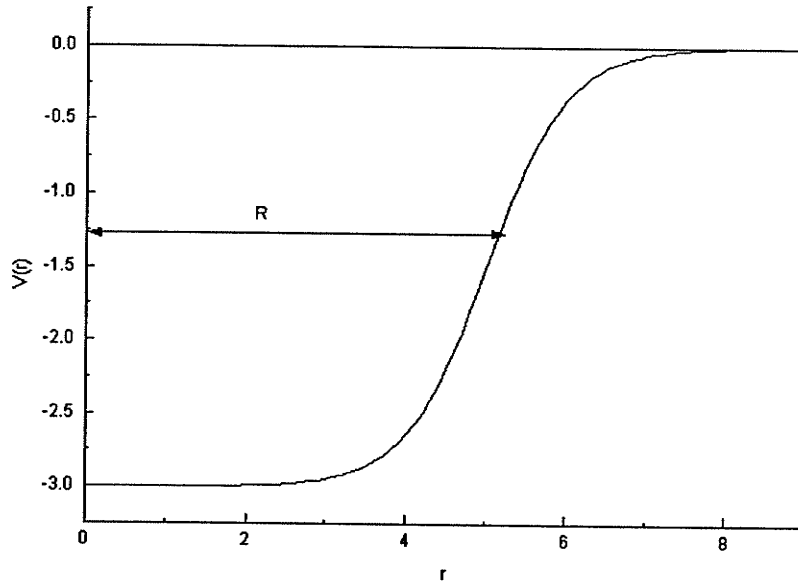
Fig. 1.2. Saxon-Woods potential illustrating the "finite extent" of this potential model

This was later extrapolated to the Saxon-Woods potential distribution (Fig 1.2) to account for finite particle separation energy:

$$V(r) = \frac{-V_0}{1 + e^{\frac{r-R}{a}}}.$$

(1.2)

The inclusion of a velocity dependent spin-orbit interaction term, -C l.s, makes the final corrections. The "magic" numbers 2, 8, 20, 28, 50, 82, 126... then came into existence (Mayer 1948). On the other extreme, complicated methods based on a Hartree-Fock approximation strive to provide a unified "mass theory" valid over the entire mass surface through the description of microscopic effective interactions. Precision mass measurements provide anchor points to test all available theories and explore discrepancies. Mass values far from stability help extend "possible test space" to a much larger extent of mass surface.

Early attempts to understand and characterize nuclear structure trends took very simple approaches. An example of this is the attempt by Dempster (Dempster 1938) to introduce the "packing fraction curve" (Fig 1.3). The packing fraction f defined as:

$$f = \frac{^A_Z M - A}{A}.$$

(1.3)

A quick examination shows the packing fraction as a measure of the "mass excess" over the mass surface. The greatest binding energy signals the minimum in the packing fraction curve. This is illustrated in the binding energy/packing fraction graph shown below. Local variation in nuclear structure can be ascertained by observing the packing fraction even more closely. A disproportionate variation in the packing fraction with respect to A, indicated by a gradient change over a local region, signals some form of new nuclear

binding mechanism. The abrupt change in slope near *A*=90, for example, is due to the shell closure at *N*=50. Similar effects can be found at the other "magic numbers".
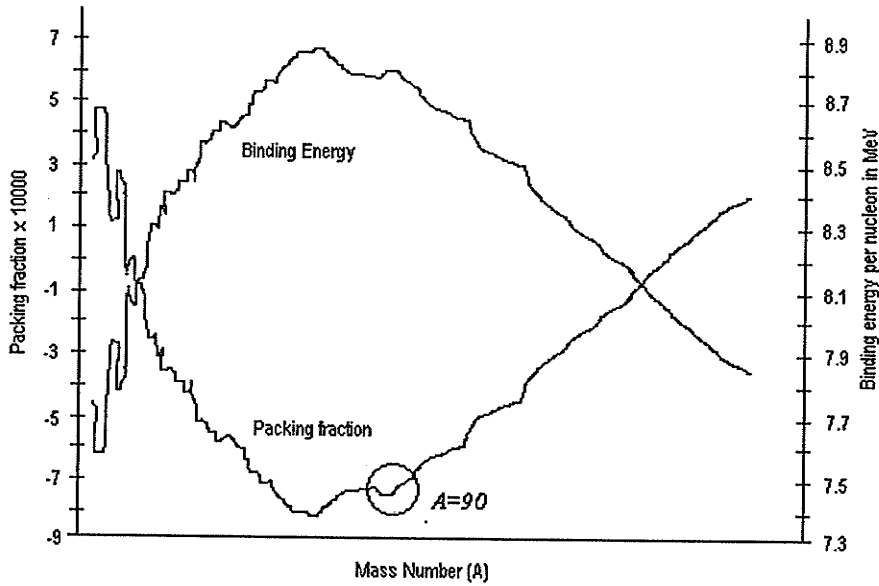
Fig. 1.3. Packing fraction and Binding energy per nucleon showing local region of "extra stability" at A=90 due to the N=50 magic number.

The Shell Model was calculated with the presumption of a spherical nucleus. Nuclear deformation exists for certain nuclei. Oblate or prolate deformation removes any simplicity of a spherical nuclear potential. A more elaborate model relates the deformed nucleus wavefunction $\psi'(\Omega)$, as a superposition of the well-known spherical wavefunctions, $\psi_{N,l,j}$.

$$\psi'(\Omega) = \sum_{lj} a(Nlj)\psi_{Nlj} \qquad (1.4)$$

S. G. Nilsson first solved the coefficients *a (Nlj)* in 1955. The energy levels arising from this computation were aptly termed as the "Nilsson particle levels". Double neutron separation energy, S_{2n}, is another means to ascertain nuclear characteristics. S_{2n} values show a smooth variation with neutron number until some nuclear "structure effect" is encountered. Abrupt gradient changes indicate major shell closures while "kinks" show deformation regions where there exists extra stability. This phenomenon of nuclear deformation around the region *A*=88 was first discovered by the Manitoba Atomic Mass Determinations (AMD) group in 1964 through the accumulation and subsequent analysis of mass spectrometric data (Barber *et. al.* 1964).

The earliest documented attempt at practical mass spectrometry can be attributed to both F. W. Aston (1919). A combination of electric and magnetic fields was used to achieve the "mass dispersion" that is characteristic of all mass spectrometers. These early machines, constructed with limited knowledge in ion optics, possessed either "velocity focusing" or "direction focusing" (Duckworth 1990*a*). With the

4

limited resolution of the early machines, Aston managed to extract mass measurements that deviated from the "whole number" rule. This prompted a formulation one of the earliest experimental probes into nuclear structure, the packing fraction, described above. The introduction of " double focusing" mass spectrometers, employing the theory of Herzog, ushered the era of high-resolution mass measurements. The Dempster-type double focusing mass spectrometer consists of a 90° radial electrostatic analyzer followed by a semicircular magnetic analyzer. This spirit was adopted in the Manitoba I (University of Manitoba) machine (affectionately known as "Big Ed") that was moved from McMaster University in the early sixties. The large instrument, r_e =2.73m, was routinely operated with a resolving power of 100,000. This machine can effectively distinguish two different ions whose masses differ by $1x10^{-5}$! Atomic mass measurements to a precision of up to 3 parts per billion (ppb) using "doublets" (Barber et al., 1964) were made using this apparatus. Deflection type mass spectrometers enjoyed unparalleled success, achieving very high precision with resolving powers of less than 500,000. Scientific endeavors were then logically directed to build compact machines with improved performance. Large magnets are cumbersome and expensive; therefore designs employing magnetic sectors became attractive. Manitoba II ("Betsy") is one such machine. Designed and built in the mid-sixties, it employs sector fields in a relatively compact configuration. The second order, double focusing design as prescribed by the theory of Hintenberger and Koenig (1959) is used as the construction basis (Barber et al. 1971, see also Chapter 2, this work).

Online mass spectrometry soon became a means to perform mass measurements on nuclei far from the line of stability or aptly termed as exotic nuclei. The principle was relatively straightforward; creation of exotic species, exotic species "selection", transport of exotics to spectrometer and finally, the mass measurement process itself. This principle remains the cornerstone in today's state-of-art "exotic mass measurement systems". The collection/ transport process must be efficient in low yield processes.
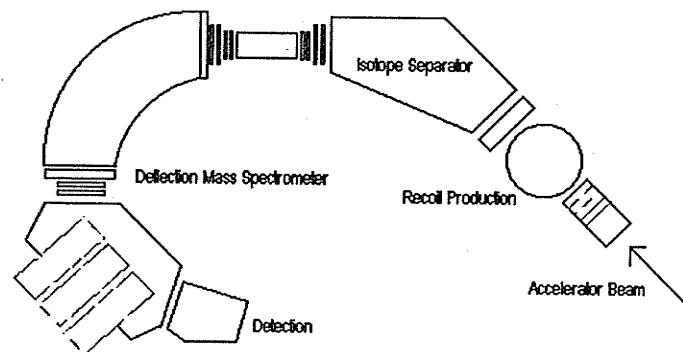
Fig. 1.4. Schematic of the typical "early" online mass measurement system

The "lifetime" of exotic nuclei imposes a time limit on the entire process from "creation" to "measurement". The mass "selection" is achieved through the use of a single magnet mass separator (ISOL -Isotope Separator OnLine) (Nielsen 1970). This was improved upon with the introduction of the Gas-

Filled Magnetic Separator (Cohen and Fulmer (1958), Armbruster (1964)) that achieves the charge/mass dispersion coupled with charge-state "normalization". The charge normalization was attained through the numerous charge-exchange collisions between the ions of interest and a buffer gas. Initial online mass measurement attempts merely consisted of positioning a deflection mass spectrometer after an isotope separator (Fig 1.4). Other early configurations consisted of a helium jet transport line to transfer the exotics to remote mass spectrometers. The early work of Bernas at Orsay (Bernas 1970) was done in a truly "online" fashion. An accelerator proton beam was made incident on a special ion source consisting of alternating foils of graphite and target material enclosed in an oven. The recoils produced are stopped in the graphite. The oven was continuously heated so that the recoil atoms diffused to the exit slit where they were ionized by surface ionization. The ions were then extracted into a mass spectrometer. It was discovered here that this heating technique proved efficient only for the alkali elements. The ion source that was previously operated by ISOLTRAP at CERN had very similar characteristics (Bollen *et al.* 1996).

Mass measurements on nuclei far from stability, termed as "exotic" nuclei, have been of interest in recent years. Apart from establishing mass points on the mass surface, exotic nuclei mass measurements are crucial in exploring the astrophysical rp-processes. To be of any effect, measurements must be performed at the 10^{-7}- 10^{-8} level of precision. New methods have been developed to tackle this issue. One such method is the coupling of a Penning Trap Mass Spectrometer to an accelerator system. The ISOLTRAP at CERN, Geneva, commissioned in the late eighties, was the first such instrument (Bollen *et al* 1990). The exotic production system had high efficiency initially only for the alkali elements. The current ISOLTRAP configuration has a far more "universal" ion source extending its capabilities even to noble gases (Herfurth 2001). The Canadian Penning Trap Mass Spectrometer (CPTMS) coupled to the Argonne Tandem Linac Accelerator System (ATLAS) at ANL stands poised to accept exotic species over the entire mass surface, limited only by the half-life constraint of 20ms. Exotic nuclei mass measurements will open a new window into nuclear structure. The neutron and proton-rich isotopes present unsurpassed opportunities to explore nuclear structure at the extremes of proton/neutron asymmetry.

Deflection mass spectrometers have set the benchmark in precision mass measurement at the part per billion levels (Duckworth, 1970). Any new technique must equal or exceed this time tested standard. The performance must also be maintained for heavy ions. Penning Trap instruments have become feasible in the arena of precision mass measurements in recent years due to technological progress. The introduction of compact superconducting magnets provides for a highly homogenous field over a small region. Ultra high vacuum (UHV) generation systems like turbomolecular and cryogenic pumps provide for experimental chambers evacuated to 10^{-9} to 10^{-10} torr in which circulating ions would have a low probability of scatter. Very low magnetic susceptibility materials allow for the device to be placed in a magnetic field without much concern for field modifying effects. Certain groups have shown that highly precise mass measurements are possible with the Penning Trap, with resolutions exceeding 1 million. Van Dyck, Schwinberg and Dehmelt used the Penning trap to measure the magnetic moment of the electron to an accuracy of 4 x 10^{-12} (Van Dyck *et al.* 1990). Mass measurements on light nuclei (A<50) have been performed using Penning traps in the regime of sub ppb accuracy (Cornell *et. al.* 1989). Extension of this

technique to heavy ions (A>100) was first done by the ISOLTRAP collaboration at CERN. The interest in this technique was specifically geared towards the measurement of exotic nuclides created online. The low yield of the species being investigated requires a mass measurement system that can work with a single ion! The Canadian Penning Trap (CPT) situated at the ATLAS beam line at Argonne National Laboratory, Illinois; USA is another exotic mass measurement system. The underlying principle in both these systems is the conversion of a continuous exotic beam into a series of bunched and cooled ion pulses. The ion pulses are then injected into the Penning trap for mass measurement. Second generation exotic trap systems are being constructed at Jyvaskyla, Finland (JYFL) and being proposed at TRIUMF, Vancouver, Canada.

The measurements performed in the course of this work involved both the deflection mass spectrometer "Manitoba II" and the Canadian Penning Trap Mass Spectrometer (CPTMS). These two devices were used to systematically measure heavy masses in the region A=180-200, a region with long standing discrepancies. The Mercury/Tungsten mass measurements (Barillari 1999) performed on "Manitoba II" provided crucial information in the A~200 mass region. The current complementary CPTMS measurements on Platinum isotopes are expected to provide additional "mass anchor points" in this region. These measurements also constitute a comprehensive high-precision systems test of the CPTMS, which is a precursor to our planned high-precision online mass measurements.

Chapter 1 References

- Armbruster, P., Hovestadt, D., Meister, H. and Specht, H. J. (1964). *Nuclear Physics,* **54,** 586.
- Barber, R. C., Bishop, R. L., Cambey, L. A., Duckworth, H. E., Macdougall, J. D., McLatchie, W., Ormrod, J. H. & van Rookhuyzen, P. (1964). *Proceedings of the Second International Conference on Nuclidic Masses,* ed. Johnson, W. H., pg. 393. Vienna: Springer-Verlag.
- Barber, R.C., Bishop, R. L., Duckworth, H. E., Meredith, J. O., Southon, F. C. G., van Rookhuyzen, P and Williams, P. (1971). *Review of Scientific Instruments,* **42,** 1.
- Barillari, D. (1999). *Ph.D. Thesis, University of Manitoba,* Canada.
- Bernas, R. (1970). *Recent Advances in Mass Spectrometry-Proceedings of the International Conference on Mass Spectroscopy, Kyoto, Japan,* edited by Ogata, K. and Hayakawa, T., pg. 535-537. London: University Park Press.
- Bollen, G., Becker, S, Kluge, H. J, Konig, M, Moore, R. B., Otto, T., Raimbault-Hartman, H, Savard, G, Schweikhard, L., Stolzenberg, H. (1996). *Nuclear Instruments in Physics Research A,* **368,** 675-697.
- Bollen, G., Moore, R. B., Savard, G. and Stolzenberg, H. (1990). *Journal of Applied Physics,* **68,** 9.
- Cohen, B. L. and Fulmer, C. B. (1958). *Nuclear Physics,* **6,** 547.
- Cornell, E. A., Weisskoff, R. M., Boyce, K. R., Flanagan, R. W., Jr., Lafyatis, G. P. and Pritchard, D. E. (1989). *Physics Review Letters,* **63,** 1674.

- Dempster, A. J. (1938). *Physical Review,* **53**,64, 869.
- Duckworth, H. E. (1970). *Recent Advances in Mass Spectrometry-Proceedings of the International Conference on Mass Spectroscopy, Kyoto, Japan,* edited by Ogata, K. and Hayakawa, T., pg. 26. London: University Park Press.
- Duckworth, H. E., Barber, R. C., Barber and Venkatasubramaniam, V. S. (1990). *Mass Spectroscopy* (2nd edition), pg. 148. Cambridge University Press.
- Duckworth, H. E., Barber, R. C., Barber and Venkatasubramaniam, V. S. (1990*a*). *Mass Spectroscopy* (2nd edition), pg. 9-14. Cambridge University Press.
- Herfurth, F., Dilling, J., Kellerbaur, A., Audi, G., Beck, D., Bollen, G., Kluge, H. –J., Lunney, D., Moore, R. B., Scheidenberger, C., Schwarz, S., Sikler, G., Szerypo, J. and ISOLDE Collaboration. (2001). *Physics Review Letters*, **87**, 142501.
- Hintenberger, H. and Konig, L. A. (1959). *Advances in Mass Spectrometry* edited by Waldron, J. D., pg.16-35. Pergamon Press.
- Mayer, M. G. (1948). *Physical Review.* **74**. 235.
- Nielsen, K. O. (1970). *Recent Advances in Mass Spectrometry-Proceedings of the International Conference on Mass Spectroscopy, Kyoto, Japan,* edited by Ogata, K. and Hayakawa, T., pg. 506-508. London: University Park Press.
- Van Dyck, R. S., Jr., P. B. Schwinberg and H. G. Dehmelt. (1984). *Atomic Physics 9*, edited by Dyke, R. S, Jr. and Fortson, E. N. World Scientific, Singapore.

2 Deflection Mass Spectrometry

2.1. *Ion Optics*

Deflection type mass spectrometers employ both electric and magnetic fields to deflect ions into a particular mass dependent path. The focusing properties of the fields must first be examined before any design can be evaluated. The ion beam normally has a finite emittance that must be taken into account early in the design stage. It is crucial for any spectrometer design to be relatively insensitive to small deviations in ion energy and angular spread. This is attained by incorporating stringent high order self-corrections in the design. An introduction to positive ion optics both for magnetic and electric fields will first be examined. The first order focusing properties of double field E, B machines will be extended to the more complex second order double focusing machines.

The homogeneous magnetic field is a momentum selector. Equally charged ions with different momenta are deflected through different paths. The semi circular magnetic analyzer has been replaced by the smaller sector systems ever since the introduction of a theory that predicts direction focusing of sector fields (Herzog 1934). This marked a turning point in spectrometer design as now smaller and cheaper sector magnets could achieve the "natural" direction focusing property of large semi circular systems. The focusing properties will involve the terminology of Herzog so as to maintain consistency even when the properties of radial electrostatic fields are examined. Consider an ion beam of mass M_o originating from point O with a half angular deviation of α. Ions with the median direction enter the field normally after traversing a field free distance of l_m' and are deflected into a path of radius r_m through an angle of Φ_m. The ions then emerge from the field normally and travel a further distance l_m'' to the image point I. The direction focusing is evident from the figure as the divergent beam is made to converge at the image point I.
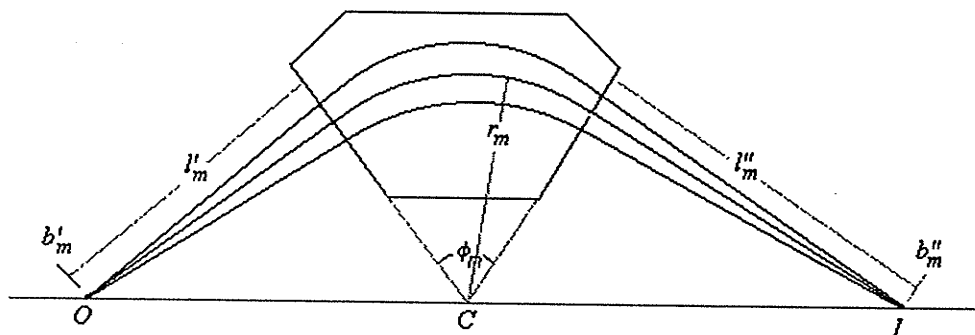
Fig. 2.1 Symmetric arrangement showing object and image points

The focal length of this system is given by:

$$f_m = r_m / sin\Phi_m \qquad (2.1)$$

The object and image distances are related through the expression:

$$(l_m{'}-g_m)(l_m{''}-g_m) = f_m^2 \tag{2.2}$$

where $g_m = f_m cos \Phi_m$, the distance from the boundary of the field to the focal point. Figure 2.1 shows that the center of curvature, image point I and object point O; all lie along a straight line (Barber's Rule, see Barber 1933, Duckworth *et al.* 1990). The image displacement $b_m{''}$ for an object displacement $b_m{'}$, change in ion mass $M = M_o (1+\gamma)$ and ion velocity $v_o (1+\beta)$, with β and γ being small, is given by:

$$b_m{''} = r_m(\beta + \gamma)\left[1 + \left(\frac{f_m}{l_m{'}-g_m}\right)\right] - b_m{'}\frac{f_m}{l_m{'}-g_m} \tag{2.3}$$

The above equation is only valid for field boundaries normal to ion trajectory. Herzog (1934) and Cartan (1937) took this into account and derived respective equations for arbitrary ion entrance and exit angles.
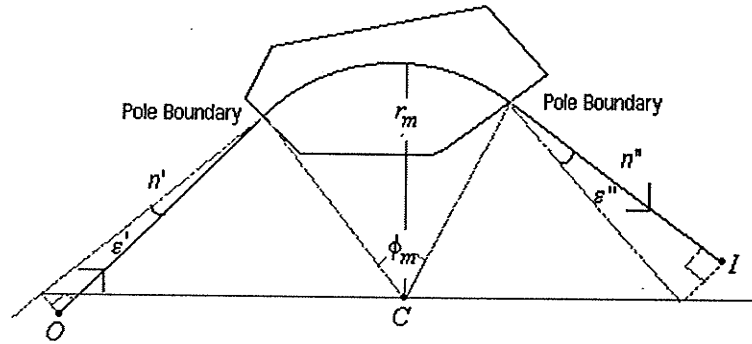
Fig. 2.2. Object and image points for arbitrary field boundaries of a sector magnet.

The Newtonian form for the focus equation is now rewritten as:

$$(l_m{'}-g_m{'})(l_m{''}-g_m{''}) = f_m^2 \tag{2.4}$$

with g'_m, $g_m{''}$ and f_m given by:

$$g'_m = \frac{r_m \cos \varepsilon'_m \cos(\Phi_m - \varepsilon''_m)}{\sin(\Phi_m - \varepsilon'_m - \varepsilon''_m)}$$

$$g''_m = \frac{r_m \cos \varepsilon''_m \cos(\Phi_m - \varepsilon'_m)}{\sin(\Phi_m - \varepsilon'_m - \varepsilon''_m)}$$

$$f_m = \frac{r_m \cos \varepsilon'_m \cos \varepsilon''_m}{\sin(\Phi_m - \varepsilon'_m - \varepsilon''_m)} \tag{2.5}$$

A graphical method (Fig. 2.2) related to the above equation enables the image point to be located through the use of geometrical construction (Cartan construction, Cartan 1937). Focusing in radial electrostatic fields can be determined using the same terminology as with homogeneous magnetic fields. It has been shown that an electrostatic field has focusing conditions similar to the magnetic case except for a factor of $\sqrt{2}$. This can be seen from the focus equations:

$$(l_e{'}-g_e)(l_e{''}-g_e) = f_e^2 \tag{2.6}$$

where

$$f_e = \frac{r_e}{\sqrt{2}} \sin\left(\sqrt{2}\Phi_e\right),$$ (2.7)

and

$$g_e = f_e \cos\left(\sqrt{2}\Phi_e\right)$$ (2.8)

A graphical construction for the electrostatic case in which Barber's rule will still hold if the field extent angle is scaled as $\sqrt{2}\ \Phi_e$ and the radius of curvature is $r_e/\sqrt{2}$. The image displacement b" for the electrostatic field is given by:

$$b_e'' = r_e(\beta + \frac{1}{2}\gamma)\left[1 + \left(\frac{f_e}{l_e' - g_e}\right)\right] - b_e' \frac{f_e}{l_e' - g_e}$$ (2.9)

In the case of a monoenergetic beam, for which, $\beta = -\frac{1}{2}\gamma$, all ions are focused at the same image point regardless of mass. The radial electrostatic analyzer is therefore an energy selector. The radial (cylindrical) electrostatic analyzer is a special case of the toroidal condenser with $r_z \rightarrow \infty$. Another interesting extension is the spherical condenser with $r_z = r_r$. Here there is both radial and axial focusing with equal focal length. The spherical condenser or deflector is routinely used to deflect ion beams while still maintaining a small overall beam spot for effective transmission through apertures.

The implementation of double E, B field configuration can cause the velocity dispersion of one field to be compensated by the other. Together with "direction focusing", this arrangement is termed as double focusing. It is common for the electric field to precede the magnetic field but the inverse arrangement has also been used in some machines. The final image position in the E, B field case is:

$$b_m'' = r_m(\beta + \gamma)\left[1 + \left(\frac{f_m}{l_m' - g_m}\right)\right] - b_m' \frac{f_m}{l_m' - g_m}$$

$$X \quad \left[\ r_e(\beta + \frac{1}{2}\gamma)\left[1 + \left(\frac{f_e}{l_e' - g_e}\right)\right] - b_e' \frac{f_e}{l_e' - g_e}\ \right]$$ (2.10)

Velocity focusing will be possible if the coefficient in β vanishes, that is:

$$r_m\left[\frac{l_m - g_m}{f_m} + 1\right] - r_e\left[1 + \frac{f_e}{l_e' - g_e}\right] = 0.$$ (2.11)

For a particular configuration, the above equation can be satisfied by varying r_m while holding all others physical dimensions constant. The discussion so far has been restricted to first order terms in α and β with higher order terms neglected. Hintenberger & Konig (1959) investigated second order focusing properties with the approximation that the fields were defined with abrupt boundaries and motion restricted to the

median plane. For the present purposes, the discussion will be based on a cylindrical condenser as the electrostatic analyzer in the E, B configuration. As summarized by Duckworth, Barber and Venkatasubramaniam for a tandem combination of electric and magnetic fields, the final image displacement from the optic axis at a distance $x = l_m''$ can be expressed as a power series, viz;

$$y_B = r_m \left(B_1 \alpha_e + B_2 \beta + B_{11} \alpha_e^2 + B_{12} \alpha_e \beta + B_{22} \beta^2 \right) \tag{2.14}$$

The coefficients in the above equation are functions of eight geometric parameters: Φ_m, ε', ε'', Φ_e, d/r_m, r_e/r_m, l_e''/r_m, l_m''/r_m. It can be seen that the terms are arranged in increasing order of α and β. By setting $B_1 = B_2 = 0$, first order double focusing is attained. The solution for second order double focusing can be attained by solving the five simultaneous equations such that $B_1 = B_2 = B_{11} = B_{12} = B_{22} = 0$. Three parameters can be chosen arbitrarily and a self-consistent solution is determined for the other five parameters. Hintenberger and Konig presented a number of geometric arrangements that comply with the second order-focusing criterion. Out of these, arrangement 8, as stated in the table 2.2 (Duckworth 1990a), is the design basis for the Manitoba II mass spectrometer constructed at the University of Manitoba.

2.2. *Manitoba II High Resolution Mass Spectrometer*

The Manitoba II mass spectrometer (Barber *et al.* 1971) was commissioned at the University of Manitoba's Physics Department in 1967. The double focusing nature of this deflection instrument accepts an ion beam with some variation in entry energy and direction and brings it to a focus at the detector. The tandem configuration consists of a 94.65° electrostatic analyzer followed by a 90° sector magnet. The choice of this particular machine specification was prompted by several reasons. The intermediate direction focus formed by the electrostatic sector at the S_β slit enables the operator to check for identical beam paths by varying the ion entry energy of the two species under experiment. This is a crucial test to ensure that Bleakney's Theorem (see below) is satisfied. The relatively compact size of the entire instrument prevents mechanical vibration and stray magnetic fields from being a cause for great concern. The relatively short path length ensures that the probability of scatter from the residual gas molecules remains low. This machine is being used for precise atomic mass measurements with precision in the parts per billion (ppb) levels. A maximum resolution of 900,000 (FWHM) has been documented (Kozier *et al.* 1980).

2.3. *Bleakney's Theorem*

Precision mass measurements performed with the Manitoba II instrument utilize a rather simple relation between the "unknown" mass and a comparison standard (a measurement doublet). This enables a mass difference to be measured. The measurement process involves tracing identical paths for both the measurement and comparison mass (ions) through the E, B fields by merely switching the electric fields according to the relation

$$M_1 V_1 = M_2 V_2; \tag{2.15}$$

A general argument for equation (2.15) can be presented as shown (Bleakney 1936). Consider motion of an ion of mass m in a region of electric field $\vec{E}$ and magnetic field $\vec{B}$ with ion velocity $\vec{v}$, traversing an orbit of distance s. The Lorentz force equation gives:

$$\vec{F} = m\vec{a} = q\vec{E} + q\vec{v} \times \vec{B}. \qquad (2.16)$$

Using the differentiation chain rule the above equation can be written as

$$\vec{F} = m\frac{d\vec{v}}{ds} \cdot \frac{ds}{dt} = mv\frac{d\vec{v}}{ds}, \qquad (2.17)$$

hence,

$$\frac{mv}{q}\frac{d\vec{v}}{ds} = \vec{E} + \vec{v} \times \vec{B}. \qquad (2.18)$$

Assume another ion of mass $m' = (1+\delta)m$ with velocity $v' = (1+\gamma)v$. The magnetic field remains constant while the electric field is changed to $E' = (1+\alpha)E$. In this case, the Lorentz equation (2.18) appears as,

$$(1+\delta)(1+\gamma)^2 \frac{mv}{q}\frac{d\vec{v}}{ds} = (1+\alpha)\vec{E} + (1+\gamma)\vec{v} \times \vec{B}. \qquad (2.19)$$

This ion can be made to traverse the same path described by equation 2.18, if

$$(1+\delta)(1+\gamma)^2 = (1+\alpha) = (1+\gamma). \qquad (2.20)$$

Therefore the following relations must be true,

$$(1+\delta)(1+\gamma) = 1, \qquad (2.21a)$$

$$(1+\alpha) = (1+\gamma). \qquad (2.21b)$$

Hence,

$$(1+\delta)(1+\alpha) = 1. \qquad (2.22)$$

Multiplying both sides of (2.22) by m and E attain,

$$m'E' = mE \qquad (2.23)$$

The electric fields can be expressed as the voltages required to generate these fields. Hence equation 2.23 can be written to resemble (2.15).

$$m'V' = mV \qquad (2.24)$$

In principle, this relationship is required for every electrostatic element in the instrument, such as electrostatic lenses, ion source voltage and of course the voltage applied to the electrostatic analyzer plates. For several of these, the ion beam position is relatively insensitive. However, for the electrostatic analyzer voltage, the peak position is extremely sensitive.

2.4. *Peak Matching*

Suppose that the ions of a specific mass after traversing the tandem E, B fields are incident on the ion detector. Then after the potentials are switched, the other species is incident at the same detector position. The switching when done on alternate sweeps of the oscilloscope would make the display of both peaks appear superimposed on an oscilloscope. By proper selection of the switched voltage, both peaks can appear perfectly superimposed or "matched" on the scope display. Consider M' to be the peak that will be switched so that it is perfectly superimposed or matched to peak M (assuming $M>M'$). The analyzer potential in the *unswitched* state is set to pass ions of mass M along the E, B axis of symmetry. Hence with:

$$\Delta M = M - M',$$
$$\Delta E = E' - E. \tag{2.25}$$

Dividing the equations above by M' and E respectively, attain:

$$\Delta M/M' = M/M' - 1,$$
$$\Delta E/E = E'/E - 1. \tag{2.26}$$

Together with the Bleakney's theorem $ME = M'E'$ attain:

$$\Delta M/M' = \Delta E/E, \tag{2.27}$$

or with the proportional voltages:

$$\Delta M/M' = \Delta V/V \tag{2.28}$$

This procedure of peak matching by switching very accurate small potentials is used in the routine operation of the Manitoba II mass spectrometer.

Computer assisted peak matching is believed to be superior to any attempt to match by "eye" inasmuch as it is independent of the operator. The process has been elaborated elsewhere (Barillari 1999) and used in this work. This involves applying the switched potential such that "close" to a perfect match is achieved. Figure 2.3 shows the different matched positions. A linear relationship is attained provided that D_1 and D_2 are very small and the actual matching potential (D=0) is then determined. This sequence is then repeated by bringing the heavier mass to be matched with the lighter mass. A total of eight different matching modes are used to remove any bias that might arise.
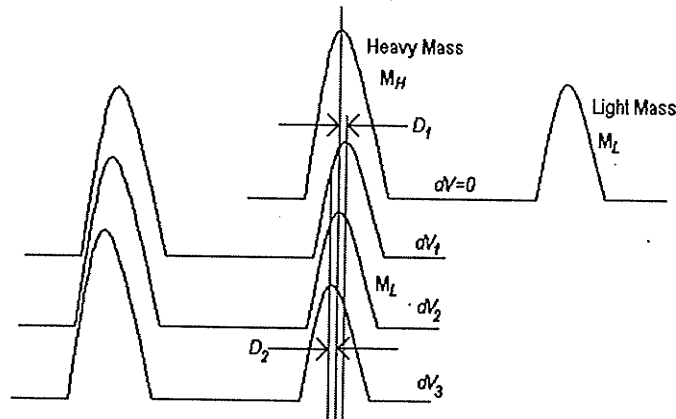
Fig. 2.3. Computer matching where two peaks are matched. The data stored is then analyzed off-line

2.5. Operational Electronics

The Manitoba II spectrometer had undergone a major electronics reconstruction during the period 1994-1998. The improvements are documented with detail in the Ph.D. thesis of D. K. Barillari (1999). The potentials for the electrostatic analyzer plates were, prior to 1995, derived from a stack of extremely stable mercury reference cells. The removal of this product from the market due to environmental concerns had made the change a necessity. The current configuration (Fig. 2.4) uses linear supplies for the base voltage of about +/- 400V (Fluke 1440). The small float voltages ($dV+$, $dV-$) are derived from a microvolt stable supply built in-house. A digital master sequencer provides the trigger signals to perform the various voltage switching processes. The various electrostatic potentials are switched simultaneously and the data scan is triggered after a settling period of 0.5ms. Solid state switches (Precision Monolithics SW02) replaced the aging mechanical switching relays. The performance of these solid state systems even in the "microvolt reproducibility" regime has prompted the author to introduce these devices into the CPT MS system. If the ion beam is swept across the collector slit, the signal at the electron multiplier has a "peak" of the type shown for a single scan in Fig. 2.3. Helmholtz coils driven by a triggered ramp current waveform provides the small time dependent ("saw tooth") magnetic field to perform the above-mentioned scanning. The "saw tooth" waveform originates from the same oscilloscope that is used to view the output of the electron multiplier.

The trigger sequence consists of four distinct "phases". Each phase involves adding or subtracting a small voltage from the ESA plates to bring the mass under experiment and the reference mass into coincidence (peak matching). The resulting four scans are stored into the signal averager memory, which is later retrieved for off-line analysis.
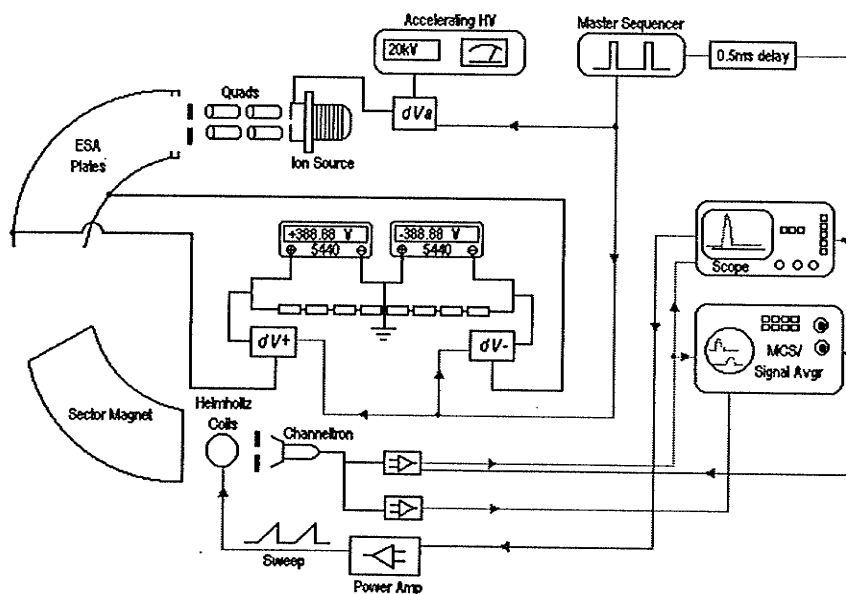
Fig. 2.4. Electrical overview of the Manitoba II High Resolution Mass Spectrometer

Chapter 2 References

- Barber, N. F. (1933). *Proceedings of the Leeds Philosophical and literary Society*, **2**, 427.

- Barber, R.C., Bishop, R. L., Duckworth, H. E., Meredith, J. O., Southon, F. C. G., van Rookhuyzen, P and Williams, P. (1971). *Review of Scientific Instruments*, **42**, 1.

- Barillari, D. K. (1999). *Ph.D. Thesis, University of Manitoba*, Canada.

- Bleakney, W. (1936). *American Physics Teacher*, **4**, 12.

- Cartan, L. (1937). *Journal de Physique et le Radium*, **8**, 453.

- Duckworth, H. E., Barber, R. C., Barber and Venkatasubramaniam, V. S. (1990). *Mass Spectroscopy* (2nd edition), pg. 10. Cambridge University Press.

- Duckworth, H. E., Barber, R. C., Barber and Venkatasubramaniam, V. S. (1990). *Mass Spectroscopy* (2nd edition), pg. 38. Cambridge University Press.

- Herzog, R. (1934). *Zeitschrift für Physik*, **89**, 447.

- Hintenberger, H. and Konig, L. A. (1959). *Advances in Mass Spectrometry* edited by Waldron, J. D., pg.16-35. Pergamon Press.

- Kozier, K. S., Sharma, K. S., Barber, R. C., Barnard, J. W., Ellis, R. J., Derenchuk, V. P. and Duckworth, H. E. (1980). *Canadian Journal of Physics*, **58**, 1311.

3. Radio Frequency Quadrupole Devices

In the work described in this thesis, measurements were made with both a classical deflection mass spectrometer, Manitoba II and with the Canadian Penning Trap Mass Spectrometer (CPT MS). A description of the basic principles of operation of the former is given in Chapter 2, while a summary of the basic principles governing the operation of the three fundamental components of the latter is given in Chapter 3.

Radio Frequency Quadrupole (RFQ) devices include two-dimensional mass filter/ion guides and three-dimensional ion traps. The mentioned dimensions refer to the confining field. The mass filter confines ions in both x and y, with the ions free to move along the z direction. Ion trap, on the other hand, confines ions in both r and z, hence the "trap" terminology. The original patent (Paul 1960) for the RFQ mass filter was awarded to Paul and Steinwedel in 1960 and the Nobel Prize for physics was subsequently awarded to Paul and Dehmelt in 1989 for their work on application of ion traps to atomic physics. The physical construction of the mass filter/ion guide consists of an array of four-rod electrodes. Radio frequency power supplies are configured such that the opposing electrodes (a set) have the same RF phase, while the other set is 180° out of phase. Figure 3.1 shows the very basic setup of an ion guide. A DC offset can be applied to a rod set to allow for mass selectivity.
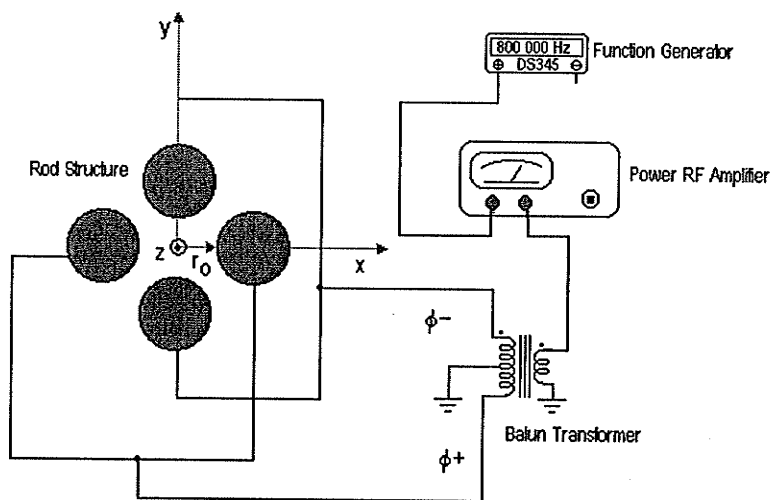
Fig. 3.1. Electrode structure and RF driver for a two dimensional ion guide system

For a given set of parameters like RF/DC voltages, RF frequency and electrode dimensions, ions of a certain m/z ratio will have stable trajectories and traverse the rod structure en route to a detector. Ions with a different m/z ratio will however have unstable trajectories and collide with the electrodes thereby effectively being removed from the system.

The ion trap could be considered as a "solid of revolution" of the mass filter (Todd 1991). That is, if one takes the two-dimensional cross section of the filter (Fig. 3.1) and rotates it about the y-axis, one gets effectively hyperboloids of revolution forming the ring and end caps of the ion trap. Adopting a similar

configuration, it is easy to see that on rotation, one rod set forms the ring while the other set forms the two endcaps. A common mode of ion trap operation is when the RF/DC potentials are applied on the ring electrode with both the endcaps held at ground potential (Todd 1979). The operating principle is once again based on ion trajectory. Ions with stable trajectories remain trapped indefinitely (ideally) while ions with unstable trajectories collide with the electrodes after a couple of oscillations. Ion motion for both the above mentioned RFQ devices are derived from similar mathematical treatments. This section provides an introduction to RFQ device theory and explore the origins of the myriad of device uses.

The CPTMS currently employs a modified (DC gradient), gas filled version of the linear quadrupole in the cooler and a gas filled RFQ trap as a buncher/cooler. A linear trap is also situated in the last section of the cooler. The theory discussed below (section 3.1) will pertain to ion motion in a standard RFQ ion guide/trap.

3.1. *Theory-2 Dimensional RFQ Ion Guide.*

A quadrupolar field of potential ϕ in Cartesian co-ordinates is given by:

$$\phi(x, y, z) = (\phi_o/2r_o^2)(\lambda x^2 + \sigma y^2 + \gamma z^2) \qquad (3.1)$$

where ϕ_o is a constant and r_o is a physical dimension pertaining to the field generating electrode configuration. The constants λ, σ and γ are determined by the nature of the field. The constraint is imposed by the mandatory compliance with Laplace's equation, which yields:

$$\nabla^2\phi = (\phi_o/r_o^2)(\lambda + \sigma + \gamma) = 0 \qquad (3.2)$$

This translates to the non-trivial condition:

$$\lambda + \sigma + \gamma = 0 \qquad (3.3)$$

Consider a two dimensional field which is z independent. This is attained by setting $\gamma=0$ and Laplace's equation dictates that $\lambda =-\sigma$. This condition can be satisfied by the following potential configuration where a DC voltage U and an oscillating radio-frequency voltage $V_o cos\Omega t$ are applied on electrodes (fig 3.1). The RF voltage is applied on the electrodes such that one set of opposing rods is in phase with the other set anti –phased. This potential is given by:

$$\phi(x, y) = ((U - V_o cos\Omega t)/2r_o^2)(x^2 - y^2) \qquad (3.4)$$

The equations of motion can be attained from $F_x = -q\partial\phi/\partial x$, $F_y = -q\partial\phi/\partial y$, hence:

$$x'' + (q/mr_o^2)(U - Vcos\Omega t) x = 0$$
$$y'' - (q/mr_o^2)(U - Vcos\Omega t) y = 0$$
$$z'' = 0 \qquad (3.5)$$

These equations can be parameterized using the following:

$$a_x = a_y = 4qU/mr_o^2\Omega^2$$
$$q_x = q_y = 2qV/mr_o^2\Omega^2$$
$$\Omega t = \xi \qquad (3.6)$$

This enables equation 3.5 to be rewritten as

$$d^2x/d\xi^2 + (a_x - 2q_x cos2\xi) x = 0$$

$$d^2y/d\xi^2 - (a_y - 2q_y \cos 2\xi)\, y = 0 \qquad (3.7)$$

Equation 3.7 is the canonical Mathieu equation (Todd 1991) from which the solutions for motion are obtained. Basically the solutions are classified as *stable* or *unstable* depending on the ion trajectory. The ion trajectories develop in time. Certain trajectories have initial (t=0) stability but instability will set in with time spent in the RF field. The onset of instability occurs when the amplitude of ion oscillation starts increasing. There will come an instant when the amplitude reaches the characteristic dimension r_0 at which time the ions collide with the electrode and are removed from the system. This trajectory development is directly dependent on the time spent in the RF field. This is, in turn, dependent on the rod structure length, frequency of ion oscillation and the axial injection energy. A long rod structure provides an increased path length for the different m/z ions to develop varying exit trajectories. The number of oscillation cycles within the structure also provides effective trajectory development. The axial injection energy determines how long the ions spend in the RF field; thus ions are normally injected with low axial energies. The factors described above determine apparatus resolution. That is, the ability of the apparatus to differentiate between different m/z ions simply by transmission of one species while the other species is filtered out. The analytical solution to Mathieu's equation can be expressed in a form:

$$u(\xi) = A e^{\mu\xi} \sum_n c_{2n} e^{2in\xi} + B e^{-\mu\xi} \sum_n c_{2n} e^{-2in\xi} \qquad (3.8)$$

Where $u = x, y$ and sum n ranges from $+\infty$ to $-\infty$. The constants A and B are determined from the initial conditions. A physical solution should correspond to u being finite as $\xi \to \infty$. This boundary condition determines the various types of solutions:

• μ being real causes unconditional instability due to the $e^{\mu\xi}$ or $e^{-\mu\xi}$ factors.

• $\mu = i\beta$ being purely complex enables a stable oscillating solution (u finite as $\xi \to \infty$).

• $\mu = im$ where m is an integer gives a periodic solution but not bound indefinitely. These are classified as *Mathieu function of integral order* (Dawson 1976). These provide the limits for stability, as time development will ultimately render initially stable solutions unstable. Thus we can limit β to non-integer values for unconditional stability.

$$u(\xi) = A\sum_n c_{2n} e^{(2n+\beta)i\xi} + B\sum_n c_{2n} e^{-(2n+\beta)i\xi} \qquad (3.9)$$

Equation 3.9 shows that the ion motion is composed of discrete frequency components $(2n + \beta)$. This can be rewritten in a more obvious form:

$$\omega_n t = (2n + \beta)\xi$$
$$\omega_n = (2n + \beta)\Omega/2 \qquad (3.10)$$

where Ω is the frequency of the applied RF field, the fundamental RF frequency. Consider the first few frequency components for n = -2, -1, 0, 1, 2. This gives components of $(\beta/2)\Omega$, $(1-\beta/2)\Omega$, $(1+\beta/2)\Omega$, $(2-\beta/2)\Omega$ and $(2+\beta/2)\Omega$ in order of increasing frequency for an operating point $0 < \beta < 1$. The motion is thus composed of a low frequency "secular" component, superimposed upon which is a high frequency ripple ("micromotion") (Fig. 3.2). The dominant secular component is that of n = 0, hence it is termed, the fundamental secular frequency. For the two axes of motion under consideration, we can expect separate values of β for the x and y

axes, β_x and β_y. Hence the motion is a complex combination of secular and micro motions in both axes. Calculations relate β to the a and q parameters in the approximate form $\beta = [a + (q^2/2)]^{\frac{1}{2}}$.
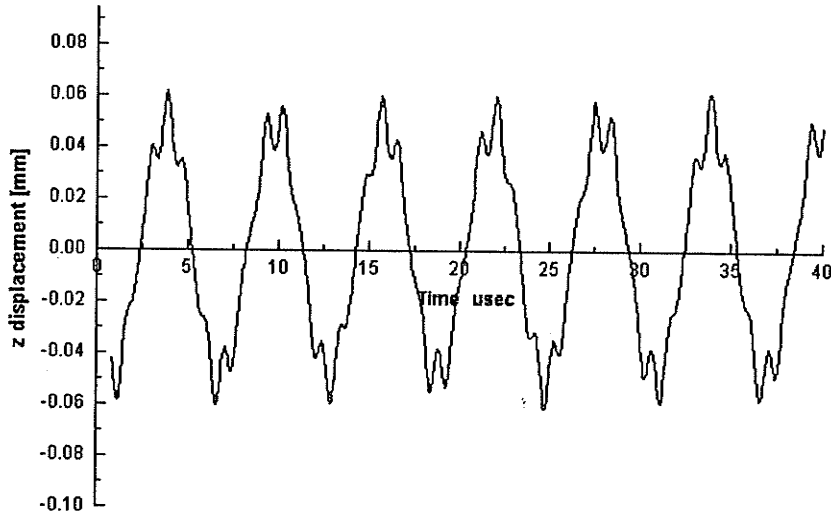
Fig. 3.2. Ion motion showing the secular and micromotion components

For our discussion, this approximation should suffice. Keeping in mind that the unconditionally stable regions of interest are bounded by integer values of β due to the abovementioned Mathieu function of integral order, the stability region can be sketched (Fig. 3.3a). Consider the *first* stability region bounded by the $\beta = 0$ and $\beta = 1$. Now we invert this to attain a similar region for the x-axis (differs by a factor of –1). The overlap defines the region stable in *both* in x and y which thus defines the operating region for successful confinement (Fig. 3.3b). Higher regions of stability also exist but most mass filter operation is confined to the first stability region where the overlap is the greatest.
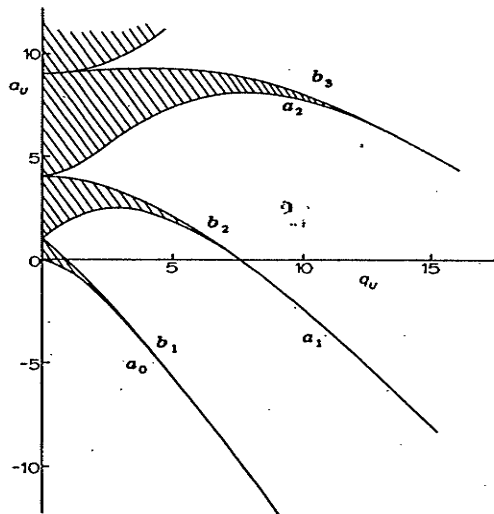
Fig. 3.3a. Stability regions for the 2-dimensional RFQ ion guide
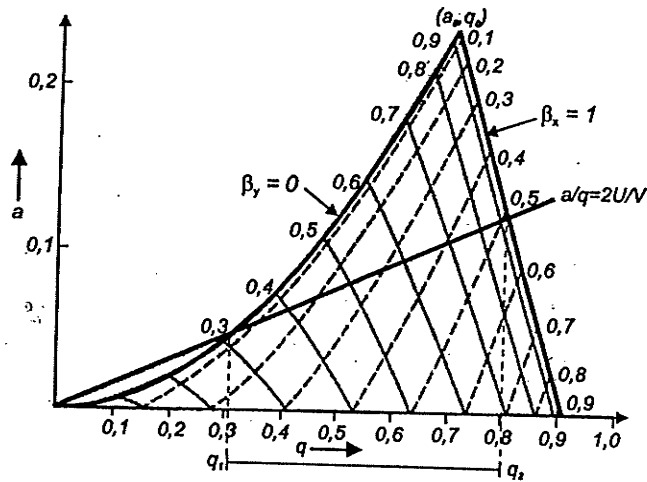
Fig. 3.3b. First stability regions for the 2-dimensional RFQ ion guide

Mass filter operation relies on ion motion discrimination with respect to m/z ratio. The idea is to pass ions of a particular m/z through the analyzer while preventing all others from reaching the detector. From the stability diagram, it should be noted that for effective mass filter operation, the operation point must be selected such that ideally ions with only a particular m/z are transmitted. This ideal operating point is the apex of the stability zone. In reality, mass filter operation is based on setting a constant a/q (U/V) ratio that determines the operating line. The steeper the operating line, the smaller the range of masses transmitted. Increased resolution is possible by making the operating line (mass scan) cut the stability region very close to the apex. An interesting application is to set $a = 0$. Ions over a large m/z range are transmitted; this mode of operation is classified as an ion guide. A separate section is dedicated to RFQ device operation. Here the different methods of operation will be examined in greater detail.
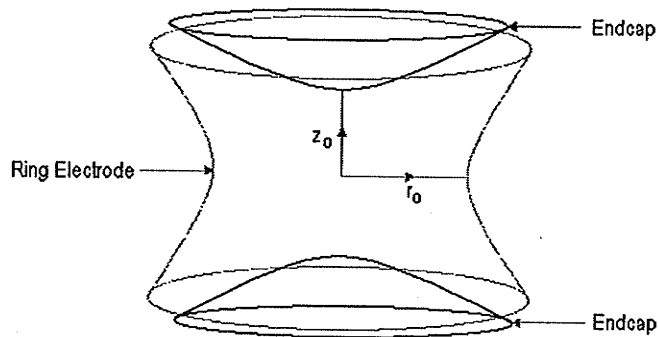
Fig. 3.4. Electrode structure of the RFQ Trap.

3.2. *Theory-3 Dimensional RFQ Ion Trap.*

Radio Frequency Quadrupole Ion Trap theory is just a simple extension of that described for the mass filter. In this case we have three-dimensional confinement in the r and z-axis. A three-dimensional quadrupole field is attained by setting $\lambda = \sigma = -\gamma/2$ in equation 3.3. This field configuration can be realized with the electrode structure shown Fig. 3.4. The dimensional constraint being $r_o^2 = 2z_o^2$. The application of a DC voltage U and an alternating RF voltage of $V\cos\Omega t$ between the end caps and the ring electrode yields a potential in the enclosed region of:

$$\phi (x, y, z) = ((U-V_o\cos\Omega t) /2r_o^2) (x^2 + y^2 - 2z^2) \qquad (3.11)$$

or in cylindrical coordinates (due to azimuthal rotational symmetry):

$$\phi (x, y, z) = ((U-V_o\cos\Omega t) /2r_o^2) (r^2 - 2z^2) \qquad (3.12)$$

For the perfect quadrupole field configuration (no terms in rz), the equations of motion can be obtained in straightforward manner from evaluating $Fr = -q\partial\phi/\partial r$ and $F_z = -q\partial\phi/\partial z$. This yields:

$$r'' + (q/mr_o^2) (U-V\cos\Omega t) r = 0$$
$$z'' -2(q/mr_o^2) (U-V\cos\Omega t) z = 0 \qquad (3.13)$$

Using a similar parameterization as equation 3.6

$$a_z = -2a_r = -8qU/ mr_o^2\Omega^2$$
$$q_z = -2q_r = 4qV/ mr_o^2\Omega^2$$
$$\Omega t = 2\xi \qquad (3.14)$$

yields the canonical Mathieu equation:

$$d^2u/d\xi^2 + (a_u - 2q_u\cos2\xi_u) u = 0 \qquad (3.15)$$

where u can be r or z. The computation so far has been very similar to the 2-D mass filter case.
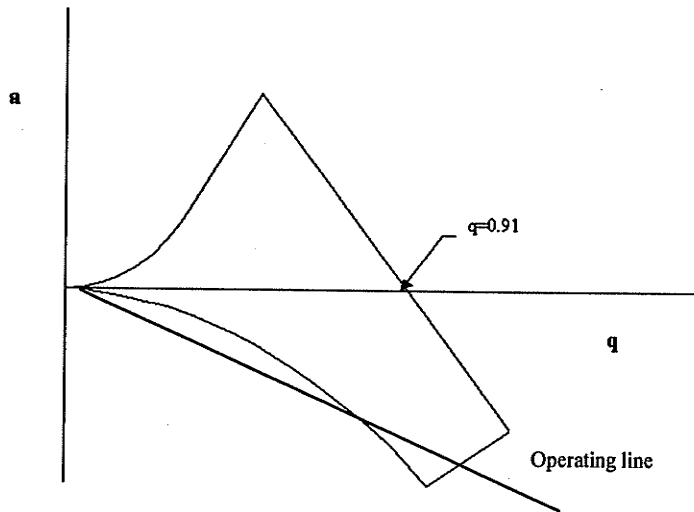
Fig. 3.5. Stability diagram for the 3-dimensional RFQ Trap

The solution is still given by equation 3.9, where the motion consists of a sum of oscillation frequencies. The stability diagram is slightly different because there is a factor of 2 between the a and b parameters for the r and z-axis. The stability diagram is shown in figure 3.5.

The operating line a/b or U/2V determines the ions with m/z ratios that adopt stable trajectories and thus remain confined within the trap enclosure. By increasing the slope of the operating line, a narrow range of m/z can be successfully stored, a criterion for high resolution. Operation along the a = 0 line enables the RFQ trap to act like an universal ion store, where ions over a wide m/z range are stored in the trap (Stafford 1984). This mode of operation is widely used, as no DC component is required. The uses range from a simple ion storage device to a chemical reaction chamber with "post reaction" mass spectrometer capability (Todd 1999). Recent advances in ion trap technology have pushed the RFQ trap to a favorable position amongst mass spectrometric devices. The ability to store ions for a definite period of time provides a suitable coupling to pulsed ion sources. A continuous ion beam can be converted to a pulsed nature through a RFQ ion trap interface. It is common to find complete mass spectrometric (MS) systems composed of consecutive stages of ion guides and ion traps.

3.3 RFQ devices in the CPTMS

The role of RFQ devices in the CPTMS system is tailored towards effective on-line beam transport as well as ion accumulation/cooling. The diverse use of RFQ devices can itself be seen in just this one experimental set-up (Fig. 3.6). At the head of the on-line configuration, there exists a RF funnel gas catcher for stopping highly energetic radioactive ions in a buffer gas (Helium). The high ionization energy of helium ensures that gas-ion collisions do not result in charge neutralization of the ions from stripped electrons. The large gas catcher entrance aperture provides an appreciable acceptance to the largely divergent product ion trajectory. The RF funnel provides a strong focusing force that directs the ions away from the walls of the structure. The Helium gas flow draws the ions towards the exit aperture and into an ion guide. The funnel thus provides an interface between a large acceptance of the gas catcher and the much smaller acceptance of the ion guide.
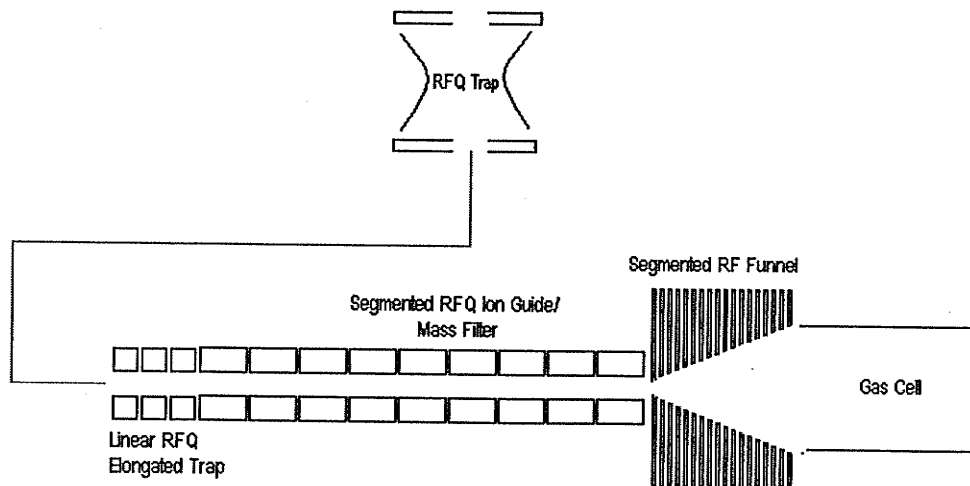
Fig. 3.6. RFQ devices in the CPTMS system

The ion guide is segmented into three sections where one section can be operated as a mass filter. The last or third section is configured as a linear "elongated" trap. Here the ions are collected and are pulsed at a user-defined rate to the CPTMS. Inasmuch as this device incorporates some unconventional features, a more detailed description will follow on the gas catcher/ion guide system in Chapter 5. The present discussion will be restricted to the operation of the RFQ Paul trap as an ion accumulator/cooler in the CPTMS system.

The precision mass measurement time period (around 1second) introduces the need for a device to accumulate ions until the precision trap is ready to accept the next bunch. The ion source pulsing rate is normally higher (approx. 20Hz) than the measurement cycling rate of the precision trap. Efficiency dictates that a method must be in place to ensure that the ions produced during the "closed" portion of the mass measurement cycle (part of the measurement cycle where the precision trap is not able to accept incoming ions) can be contained until such a time that the precision trap is ready for the next injection sequence (Fig. 3.7). The RFQ trap fills the role of a temporary ion store with ease (Franzen 1996). The ion source pulsing at 20Hz can now be effectively coupled to any post apparatus say having a cyclic rate of 1Hz. Multiple ion bunches can now be collected during the wait dictated by the mass measurement process. The inclusion of a small amount of buffer gas "cools" the collected ions through numerous energy moderating ion-atom collisions. These collisions remove energy from the ions so that they settle towards the bottom of the trapping potential (Savard 1997). The accumulated ions form a "new" bunch with energies very different from that during injection. This new bunch can then be ejected with an energy/time spread tailored to suit the acceptance of the post apparatus. To the post apparatus, the RFQ trap appears as an "ion source" delivering an ion beam that is suited to its requirements both in cyclic rate as well as energy/time distribution. The energy/time spread on ejection is normally "modified" in flight using a "pulsed cavity". The pulse is normally a rapidly changing arbitrary high-voltage waveform (see Chapter 6.4 and 6.5).
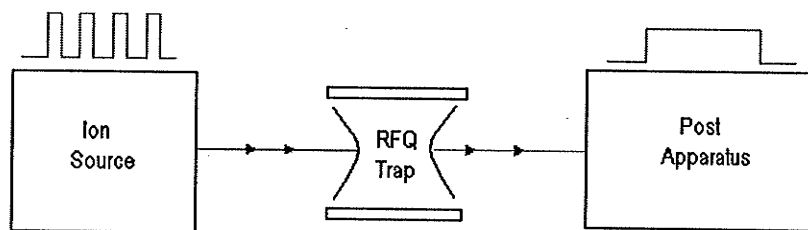
Fig. 3.7. The RFQ Paul trap being an effective interface between the different "duty cycles" of the ion source and the post apparatus

In the CPTMS system, the ions must be injected into the RFQ (Paul) trap from an external source. Conditions are set for efficient capture and subsequent confinement of these ions. In principle some method must be devised to convert the largely axial motion of the ions into a trajectory that is a bound orbit within the trap enclosure (Savard 2000). The first criterion would be to remove as much of the axial energy as possible so that the confining potential can take effect. The next point of consideration (of course linked to the criterion

stated) is to ensure that the phase space coordinates (x, x') of the incoming ions are matched to those of the trap acceptance (Todd 1980). This process is further complicated by the fact that the rapidly changing RF field does not allow for a constant acceptance in time. Therefore injection timing now becomes critical. The ion injection must be timed in such a way that a majority of the ions can have favorable initial phase space coordinates that can be mapped to match the trap acceptance at that instant (Sec. 3.3). The capture process is one in which the motion is damped. Ion entering the trap are subjected to a large retarding potential (~100V) at the trap exit plate endcap (Fig. 3.9). This retardation provides sufficient time for the damping nature of the buffer gas to take effect. The ions rapidly transfer energy to the much lighter buffer gas atoms and settle into a small region at the trap center (Fig. 3.8).
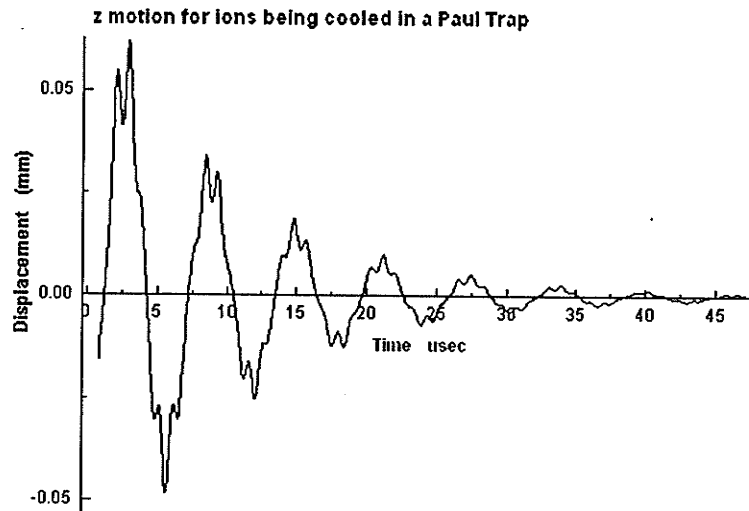
Fig. 3.8. Ion motion in an RFQ trap in the presence of a buffer gas.

The timing is crucial only during the ion entry, before the cooling has taken effect. Ions injected under unfavorable conditions will immediately take on unstable trajectories and be lost to "electrode collision" before the cooling can be effective. Once cooled, the ions take on stable trajectories in the form of small orbits about the trap center and can be confined for an extended period of time with essentially no loss. The accumulation of multiple bunches is a prerequisite of the experimental set-up. The above-mentioned difference of cycling rate between the ion source and the precision measurement system demands the collection of multiple ion bunches in the RFQ trap. This is done with relative ease as the already cooled ions now reside at the bottom of the trapping potential, unaffected by the large voltage pulse applied on the exit endcap to retard the next incoming bunch. The storage period can be anywhere from milliseconds to a few seconds, after which, the ions are ejected as a bunch to post apparatus.

The ejection process also requires certain considerations (Waldren 1979). The goal is to extract the majority of the stored ions as a bunch with minimal energy spread. Temporal spread can be relaxed as the post apparatus can accommodate time spreads of a couple of microseconds. The ejection is executed by a simultaneous "pulse out, suck-out" technique (Waldren 1979a). In this process, a positive going pulse is applied on the endcap furthest from the exit aperture while a negative going pulse is applied at the endcap with

25

the exit aperture (Fig. 3.9D). This push-pull effect draws the ions out. This is an example of fast extraction as opposed to methods of slow extraction where ions are allowed to drift gradually out of the trap. The fast extraction is employed so as to minimize the influence of the rapidly changing RF field on the ions en route to the exit aperture. The ions within the trap occupy a finite volume. A large number of stored ions imply a larger ion cloud that occupies a larger volume in the trap. The RF field is essentially zero at the trap center and increases with distance. This indicates that the ions further from the trap center have more energy pumped into the micromotion (RF heating). Thus a finite sized ion cloud has an intrinsic energy spread due to position.
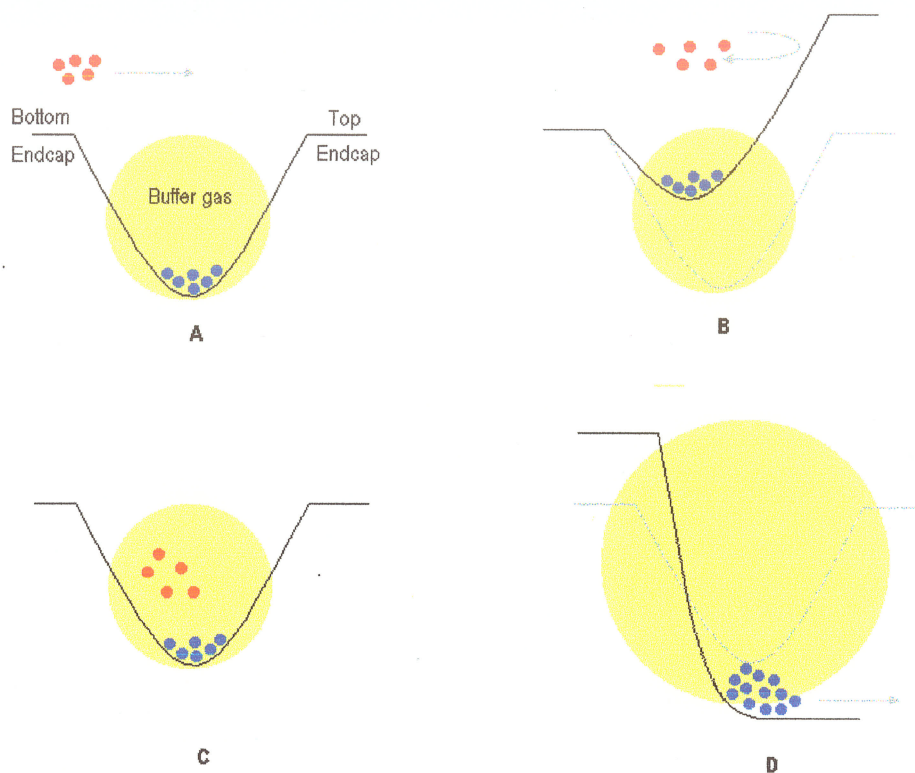
Fig. 3.9. Multiple ion bunch accumulation in the RFQ trap. (A) Incoming ion bunch decelerated prior to RFQ entry. (B) A large positive pulse is applied on the top endcap to slow the ions thereby effectively modifying the instantaneous ion bunch phase space. (C) Collision with buffer gas atoms remove energy and ions settle to the bottom of the trapping potential. (D) Cooled ions are subsequently ejected as a bunch.

During ejection, with the RF in CW mode, the ions leaving the trap earlier experience a different field configuration than the ions leaving later due to the oscillating field. This adds to the intrinsic energy spread discussed above. A device to "blank" or "freeze" the RF field (Fulford 1979, Whetten 1974) during ejection is now incorporated into the system (see Chapter 6.2). The energy spread can be minimized through the use of fast extraction coupled with a stored ion cloud of modest proportions. The energy spread that still persists despite these efforts can be corrected in-flight through the use of an accelerating/retarding time varying potential gap that accelerates the ions with below average energy and vice versa (see Chapter 6.4).

3.4. *Phase Space Methods*

The concepts of phase space dynamics regularly used in accelerator design (Baril 1974) were employed to elucidate ion motion in RFQ devices in the early 1980's. The principle is to use position (u) and velocity (u') (or momentum) coordinates to fully characterize ion motion within the confines of the device in question. The u, u' dimensions are particularly useful during the modeling of ion transfer from one device to another. Accelerator physics routinely involves beam transfer between separate devices like ion source, magnetic quadrupole lens systems, steering magnets and last but not least, the experimental chamber.
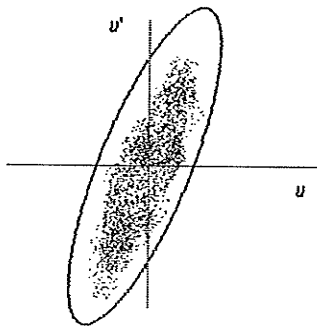
Fig. 3.10. Apparatus acceptance shown by the solid ellipse while the shaded region indicates the incoming beam emittance. In this case we can expect 100% transmission for this dimension.

The notion of beam emittance and acceptance is of prime concern as the goal is to attain 100% transmission between the different devices. This is done by ensuring that the beam emmitance (outgoing character) of a particular section matches the acceptance (incoming character) of the next section. The beam emittance/apparatus acceptance is normally displayed as an area in the *u, u'* axes. The points within this area denotes all the possible combinations of (*u, u'*) for an ion beam under certain device conditions. The overlap between the emmitance/acceptance signifies the transmission efficiency between the two sections (Fig. 3.10). Without going into too much detail, a short discussion on phase space applications in the RFQ trap is warranted before any analysis on optimum conditions for the ion injection/ejection processes can be discussed.

The solution for the Mathieu equations of motions yields a relationship between the position (displacement) *u* and its simultaneous velocity *u'* for a given phase of the RF potential field. This relationship has an elliptical form (similar to the phase space relationship for a simple harmonic oscillator) given as (Todd 1991):

$$\Gamma u^2 + 2Auu' + Bu'^2 = \varepsilon \tag{3.16}$$

The coefficients A, B and Γ are dependent on the RF phase γ and determine the orientation of the ellipse according to:

$$tan2\theta = -2A/B - \Gamma \tag{3.17}$$

with the constraint $B\Gamma - A^2 = 1$ which preserves the area of the ellipse for all phases. Thus we have a family of ellipses with the same area but rotated about the center. As the phase of the RF drive (ψ) changes, the phase-space ellipse rotates, always returning to the same orientation as the phase angle is repeated (Fig. 3.11). The "phase angle" ξ_u refers to the canonical time variable in the Mathieu equation 3.15. The relationship between ξ and ψ is given as follows:

$$\xi = (\psi/2 - \pi/2). \tag{3.18}$$

The boundary of the ellipse denotes the (u, u') coordinates that defines the limits of stability. Ion with phase coordinates outside the ellipse will not be trapped while those with coordinates on the boundary or within the area enclosed will possess trajectories conducive to trapping. It is instructive to observe that during the phase dependent rotation, the ellipse do not always present the same tolerances for the acceptable Δu and $\Delta u'$.
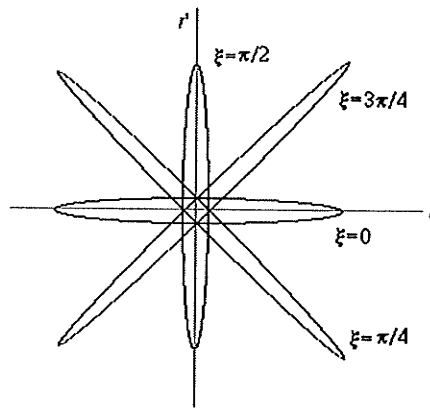
Fig. 3.11. An example of r-dimension phase space for a particular (a, q) operating point

The operating points (a, q) determine ε which in turn is a measure of the phase-space area available for trapping. A suitable phase would be one that presents an appreciable range of acceptance for both u and u' (Waldren 1979). Stability should be defined simultaneously for r and z - axes. Thus we can expect two phase-space ellipses, one for each degree of freedom. Ions should have phase-space coordinates that lie on or within both the respective ellipses to be trapped effectively.

The process of external ion injection is a complicated process whereby ions originating from an external ion source are manipulated towards being trapped in the RFQ. These ions approach the trap entrance aperture with a collection of (u, u') which must match the trap acceptance. The trap acceptance is <u>dynamic</u>, as the phase-space ellipse rotates with the rapidly evolving RF phase. The injection must be timed at a favorable RF phase so that the majority of the ions on entry have phase space coordinates that lie within the trap acceptance ellipse at a particular instant. This implies that the ions must be bunched in time. A wide temporal distribution will result in some ions entering the trap at an unfavorable phase and capture efficiency will be compromised. The accelerating field can be specifically tailored to ensure an adequately time-bunched beam prior to injection. The incoming ions would need to have their phase-space "modified" before a suitable match to the trap acceptance can be attained. The mapping can be done by applying a large positive pulse (capture pulse) over a specific time period on the exit endcap, which retards the ions as they pass through the trap. In this way the instantaneous

phase-space coordinates are changed to match the trap acceptance (Savard 1997). Other methods have been proposed to improve injection efficiency; one of these involves pulsing the RF field. In this process the RF is turned on only after the ions are in the trap (Kishore 1976, Todd 1999). In this instance, the trap acceptance ceases to be dynamic during ion entry, however the ions must possess specific (u, u') during field turn on. This requires that the ions have displacement and velocity components within the phase-space ellipses (both in r and z dimensions) of the respective phase during field activation. As an example consider ions of constant axial velocity z_o', entering the trap. The phase-space ellipse enforces that for effective trapping; the RF field must be turned on at this <u>particular phase</u> at a time t_D such that the ions are in the region between z_1 and z_2 (Fig. 3.12).
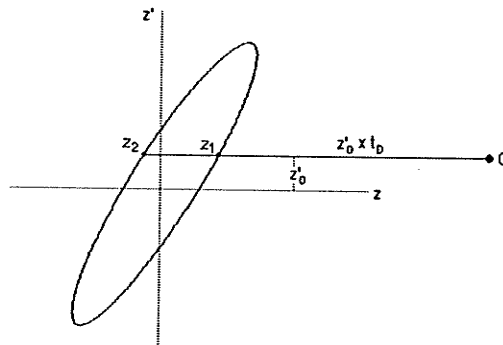
Fig. 3.12. Considerations for "pulsed RF" injection.

To keep the discussion simple we take (r, r') as $(0, 0)$, that is, a purely axial beam with zero emittance. This puts the complete ion beam at the center of the r phase ellipse thereby fulfilling the r acceptance requirement.

The requirement of a pulsed sinusoidal RF field of several kilovolts with a fall time of 100ns for proper phase synchronization is not trivial; hence this technique has practical limitations for the common sinusoidally driven RFQ traps. The HVHF Direct Drive system incorporated into the CPT MS however, offers the opportunity for pulsed RF during the injection process (Chapter 6.2).

Ion ejection simply involves synchronizing the ejection at a particular phase so that the majority of the ions have favorable trajectories to exit the trap via the exit aperture. A suitable phase for ejection is where the radial ion velocities are directed towards the trap center (Fig. 3.11. $\xi=\pi/4$). Thus on application of an axial force (ejection pulses), the resultant ion trajectories would be directed towards the exit aperture. An unfavorable ejection phase (Fig. 3.11. $\xi=3\pi/4$) is where the ion velocities are directed away from the trap center and the resultant trajectory during ejection would be directed towards the electrodes leading to imminent ion loss (Fig 3.13).
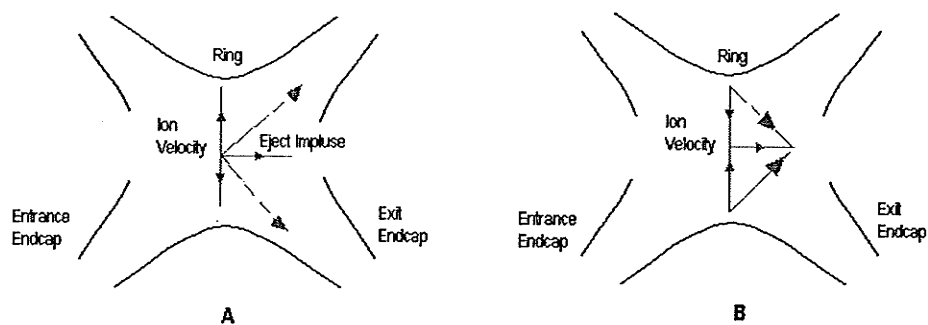
Fig. 3.13. The critical nature of ejection timing. (A) shows an unfavorable phase for ejection where ion velocities are directed away from the trap center, thereby leading to ion loss on application of an ejection impulse from the left. (B) shows good ejection timing. Here ions have velocities directed towards the trap center and therefore would have trajectories directed towards the exit aperture on application of a similar ejection impulse

The oscillating nature of the RF field could be turned off or kept constant during ejection. The RF Pulser is designed specifically for this purpose. The two states of RF "state lock" give confirmation to the above discussion. The HIGH lock state is more "ejection efficient" as with the ring held at approximately 150V. Here the ions would have velocities directed away from the ring and hence towards the trap center. A LOW lock state puts the ring at −150V, here ions are drawn towards the ring and therefore have velocities directed away from the ring leading to ion loss during ejection.

Chapter 3 References

- Baril, M and Septier, A. (1974). *Review of Applied Physics*, **9**, 525.

- Dawson, P. H. (1976). *Quadrupole Mass Spectrometry*, pg. 16. Elsevier Scientific Publishing Company.

- Franzen, J. and Schubert, M. (1996). *US Patent 5,811,800.*

- Fulford, J. E. and March, R. E. (1979). *International Journal of Mass Spectrometry and Ion Physics*, **30**, 373-378.

- Kishore, M. N. and Ghosh, P. K. (1976). *International Journal of Mass Spectrometry and Ion Physics*, **29**, 345.

- Paul, W. and Stiendwedel, H. (1960). *US Patent 2,939,952.*

- Savard, G. (1997). *Nuclear Instruments and Methods in Physics Research B*, **126**, 361-369.

- Savard, G. and Werth, G. (2000). *Annual Review of Nuclear and Particle Science.* **50**, 119.

- Stafford, G. C., Kelly, P. E., Skya, J. E. P., Reynolds, W. E. and Todd, J. F. J. (1984). *International Journal of Mass Spectrometry and Ion Processes*, **60**, 85-98.

- Todd, J. F. J and Waldren, R. M. (1979). *International Journal of Mass Spectrometry and Ion Physics*, **29**, 301-314.

- Todd, J. F. J, Freer, D. A. and Waldren, R. M. (1980). *International Journal of Mass Spectrometry and Ion Physics,* **36**, 371-386.

- Todd, J. F. J. (1991). *Mass Spectrometry Reviews,* **10**, 3-52.

- Todd, J. F. J. and March, R. E. (1999).). *International Journal of Mass Spectrometry and Ion Processes,* **190/191**, 9-35.

- Waldren, R. M. and Todd, J. F. J. (1979). *International Journal of Mass Spectrometry and Ion Physics,* **29**, 337-344.

- Waldren, R. M. and Todd, J. F. J. (1979*a*). *International Journal of Mass Spectrometry and Ion Physics,* **31**, 15-29.

- Whetten, N. R. (1974). *Journal of Vacuum Science and Technology,* **11**, 515.

4. The Penning Trap

The Penning Trap is another variant of the "ion trap". The ion confinement in this instance is achieved through the use of a weak electrostatic field and a strong magnetic field. The confinement principle can be considered to be two-fold. The strong magnetic field confines the ions radially through cyclotron motion, while the electrostatic field provides the axial confinement. The electrode structure of the Penning Trap is similar to that described for the RFQ Trap. A ring together with two endcap electrodes defines the quadrupolar electrostatic field. A large superconducting magnet provides the strong, highly homogeneous magnetic field.
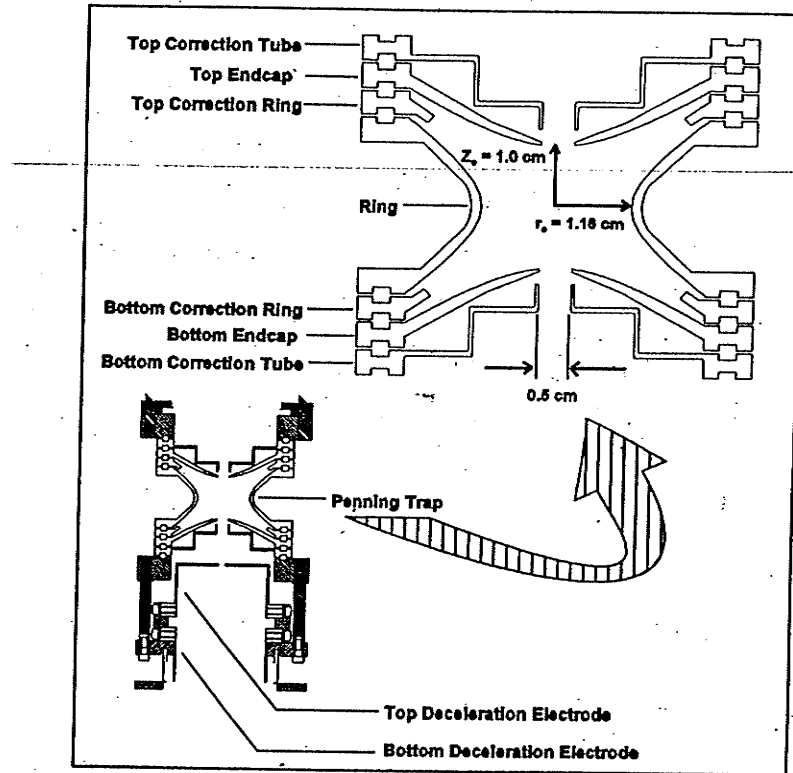
Fig. 4.1. Cross section of the Penning Trap (Fukutani 2000)

4.1. *Theory*

The ideal electrostatic trapping potential is given by:

$$V(z,r) = \frac{A}{2r_o^2}\left(2z^2 + \left(r_o^2 - r^2\right)\right). \tag{4.1}$$

A is the potential between the ring and the endcap electrodes. The electrodes are all hyperboloids of revolution extending ideally to infinity with the relation $r_o = \sqrt{2}z_o$. As an example, consider the Penning trap being operated as a "10V" trap. The endcaps are biased at 6V while the ring electrode sits at −4V. The potential distribution

32

exhibiting cylindrical symmetry is shown in fig. 4.2. It should be noted that the potential well depth is 5V, contrary to the term "10V trap". The trap dimensions used in the computation are r_o =1.16cm and z_o = 1.00cm, the dimensions of the CPT Penning trap. We will assume ideal conditions even for a truncated trap (correction electrodes produces a field close to the ideal quadrupole).
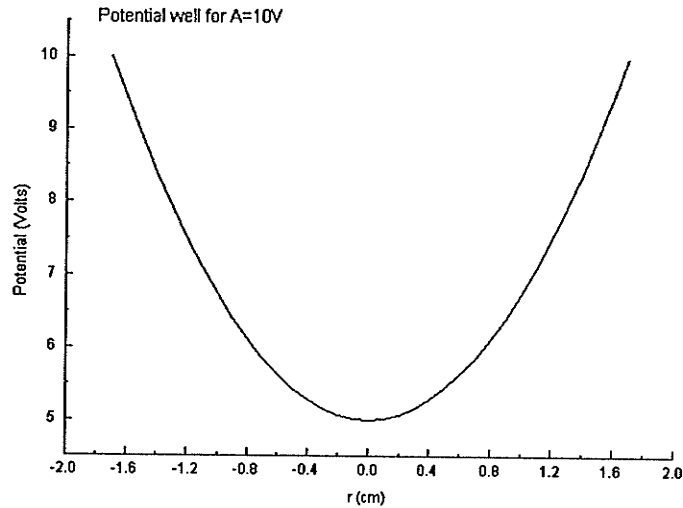
Fig. 4.2. Potential distribution for a "10V" trap

The effective trapping potential depth in this instance is approximately 5V.

Consider a homogeneous magnetic field B directed in the axial direction. Ions will develop a circular path about the field direction called cyclotron motion. The cyclotron frequency ω_c is given by the well-known expression:

$$\omega_c = \frac{qB}{m} \qquad (4.2)$$

The cyclotron motion constitutes radial confinement. Confinement in the axial direction is attained through the electrostatic potential well mentioned above. Ions having axial energies less than the potential well depth will be trapped. Therefore for ions entering the above trap, their incident axial energies must be less than 5eV for effective confinement to occur. The equation of motion is determined by the combination of the magnetic and electric fields. To facilitate computation ease, a characteristic trap dimension d is defined as:

$$d^2 = \frac{1}{2}\left(z_o^2 + \frac{r_o^2}{2}\right) \qquad (4.3)$$

Equation 1 now can be rewritten as:

$$V(z,r) = \frac{V_o}{2d^2}\left(z^2 - \frac{r^2}{2}\right) \qquad (4.4)$$

33

The electric fields directed along the z, r directions given by:

$$E_z = -\frac{\partial V}{\partial z} = -\frac{V_o}{d^2} z \hat{z}$$

$$E_r = -\frac{\partial V}{\partial r} = \frac{V_o}{2d^2} r \hat{r} \qquad (4.5)$$

The forces due to the electric field alone are $F^e{}_i = qE_i$, hence

$$F_z^e = -q \frac{V_o}{d^2} z$$

$$F_r^e = q \frac{V_o}{2d^2} r \qquad (4.6)$$

The magnetic force is only in the radial direction

$$F_r^m = q\left(\dot{r} \times \vec{B}\right) \qquad (4.7)$$

The axial motion is purely electric field dependent and the solution is straightforward.

$$m\ddot{z} + \frac{qV_o}{d^2} z = 0. \qquad (4.8)$$

This equation is pure simple harmonic with the characteristic oscillation frequency given by:

$$\omega_z = \sqrt{\frac{qV_o}{md^2}} \qquad (4.9)$$

The radial motion is a combination of both electric and magnetic contributions.

$$m\ddot{r} = F_r^e + F_r^m$$

$$m\ddot{\vec{r}} = q\left(\dot{\vec{r}} \times \vec{B}\right) - \frac{qV_o}{2d^2} \vec{r} \qquad (4.10)$$

It can be noted that the effect of the small electric field necessary for ion confinement introduces a component that "modifies" the true cyclotron frequency. The equation (4.10) can be rewritten as:

$$\ddot{r} - \omega_c \dot{r} + \frac{\omega_z^2}{2} r = 0. \qquad (4.11a)$$

The radial motion can be solved by substituting $r = e^{-i\omega t}$ into the above equation to attain:

$$2\omega^2 - 2\omega_c \omega + \omega_z = 0. \qquad (4.11b)$$

The two eigenfrequencies are:

$$\omega_\pm = \frac{\omega_c}{2} \pm \sqrt{\frac{\omega_c^2}{4} - \frac{\omega_z^2}{2}} \qquad (4.12)$$

The two frequencies constituting radial motion comprise a slow rotation, magnetron motion (ω_-) and a much more rapid rotation in the same sense, modified cyclotron motion (ω_+). From (4.12):

$$\omega_+ + \omega_- = \omega_c. \tag{4.13}$$

Other relationships between the three frequencies of motion are:

$$\omega_+ \omega_- = \frac{\omega_z^2}{2}, \tag{4.14}$$

$$\omega_+^2 + \omega_-^2 + \omega_z^2 = \omega_c^2 \tag{4.15}$$

The modified cyclotron and magnetron motions are dependent on both the electric and magnetic fields, while the true cyclotron frequency is solely dependent on the magnetic field. High precision mass measurement experiments need hyperstable operating conditions. Superconducting solenoids used in precision NMR spectrometers provide magnetic fields in the 10-50ppb homogeneity over a volume of 1cm³. Electric fields in the ppm level are not easy to generate. Even with such stable voltages, the tolerances in precision electrode machining will ultimately place immense requirements on trying to establish a pure quadrupole field in the ppm level over an appreciable volume. These considerations prompt any precise mass measurement to be made through the detection of the true cyclotron frequency alone.

4.2. *Radio-Frequency Excitation*

In order to present a comprehensive discussion on RF excitation modes in the Penning Trap, it is required that the formalism of Brown and Gabrielese (1986) is adopted. This formalism introduces two vectors $\vec{V}^+$ and $\vec{V}^-$, mathematically defined as:

$$\vec{V}^+ = \vec{r} - \omega_- \hat{z} \times \vec{r} ; \tag{4.16a}$$

$$\vec{V}^- = \vec{r} - \omega_+ \hat{z} \times \vec{r} . \tag{4.16b}$$

The terms $\vec{r}$ and $\dot{\vec{r}}$ denote the radial position and velocity vectors respectively. $\vec{V}^+$ is the velocity vector of the modified cyclotron motion with respect to the reference frame of the magnetron motion. Similarly, $\vec{V}^-$ is the magnetron velocity as observed from the reference frame of the modified cyclotron motion. The RF excitation is an auxiliary electric field applied to the system. The equation of motion now becomes:

$$\dot{\vec{V}}^\pm = \omega_\pm \hat{z} \times \vec{V}^\pm + \frac{q}{m} \vec{E}(r,t). \tag{4.17}$$

In component form, the above equation is written as:

$$\dot{V}_x^\pm = -\omega_\pm V_y^\pm + \frac{q}{m} E_x, \tag{4.18}$$

$$\dot{V}_y^\pm = \omega_\pm V_x^\pm + \frac{q}{m} E_y. \tag{4.19}$$

In the dipole excitation mode, the applied electric field is $E_y = E_d \sin \omega_d t$, $E_x = 0$. In this mode, the first order differential equations for $\vec{V}^+$ and $\vec{V}^-$ are decoupled and the solution is trivial.

$$V_x^\pm = C_1 \cos\omega_d t, \qquad\qquad\text{(4.20a)}$$

$$V_y^\pm = C_2 \sin\omega_d t, \qquad\qquad\text{(4.20b)}$$

with $C_1 = \dfrac{\omega_d}{\omega_\pm}B$ and $C_2 = -\dfrac{\omega_\pm^2}{\omega_\pm^2 - \omega_d^2}\dfrac{q}{m}E_d$.

The system energy, after an excitation period of T_{RF}, is given by the Fourier Transform,

$$I(\omega) = \frac{\sin^2\left(\dfrac{\omega_d - \omega_\pm}{2}T_{RF}\right)}{\left(\dfrac{\omega_d - \omega_\pm}{2}\right)^2} \qquad\qquad\text{(4.21)}$$

The "resonance" condition is easily visible as the amplitude increases when the driving frequency ω_d approaches either ω_+ or ω_-. The solution in Cartesian coordinates is attained through simple vector algebra.

$$v_x = -r_+\omega_+ \sin(\omega_+ t) - r_-\omega_- \sin(\omega_- t) \qquad\qquad\text{(4.22a)}$$

$$v_y = r_+\omega_+ \cos(\omega_+ t) + r_-\omega_- \cos(\omega_- t) \qquad\qquad\text{(4.22b)}$$

The power absorbed, $P = q\vec{v}.\vec{E}$, by an ion moving in a dipole field is therefore,

$$qE_d \cos(\omega_d t)[r_+\omega_+ \cos(\omega_+ t) + r_-\omega_- \cos(\omega_- t)]. \qquad\qquad\text{(4.23)}$$
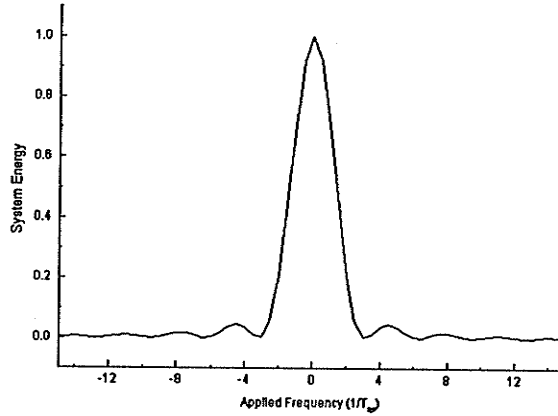
Fig. 4.3. Energy absorption profile for an externally driven resonating system

A similar treatment will be performed for an azimuthal quadrupolar electric field. In this instance the field components are given by,

$$E_x = -E_q y,$$

$$E_y = -E_q x. \qquad\qquad\text{(4.24)}$$

The equation of motion for the quadrupole excitation mode is hence written as,

36

$$\dot{V}_x^{\pm} = -\omega_{\pm} V_y^{\pm} - \frac{q}{m} E_q y \tag{4.25a}$$

$$\dot{V}_y^{\pm} = -\omega_{\pm} V_x^{\pm} - \frac{q}{m} E_q x \tag{4.25b}$$

To solve the above equations, x and y must first be expressed in terms of the velocity vectors, $V_x^{\pm}$ and $V_y^{\pm}$.

$$x = -\frac{V_y^+ - V_y^-}{\omega_+ - \omega_-} \tag{4.26a}$$

$$y = +\frac{V_x^+ - V_x^-}{\omega_+ - \omega_-} \tag{4.26b}$$

The equation of motion above can thus be written as,

$$\dot{V}_x^{\pm} = -\omega_{\pm} V_y^{\pm} + k\left(V_x^+ - V_x^-\right) \tag{4.27a}$$

$$\dot{V}_y^{\pm} = \omega_{\pm} V_x^{\pm} + k\left(V_y^+ - V_y^-\right) \tag{4.27b}$$

$$k = \frac{q}{m} E_q \frac{1}{\omega_+ - \omega_-}$$

The electric field is oscillating at ω_d. This makes k an oscillation term, which can conveniently be expressed as

$$k = k_o \cos \omega_d t. \tag{4.28}$$

The solution for the equations of motion (4.27a,b) can be written in a general form as

$$\vec{V}^{\pm} = \vec{A}^{\pm}(t) e^{\pm i\omega_{\pm} t}, \tag{4.29}$$

where $A^{\pm}(t)$ consists of slowly varying amplitude functions. To present a comprehensive discussion, a little algebraic manipulation is necessary. The oscillation term k (4.28) can be written in an exponential form,

$$k = \frac{k_o}{2}\left(e^{i\omega_d t} + e^{-i\omega_d t}\right). \tag{4.30}$$

Consider the equation of motion for $V_x^{\pm}$. From (4.27a) and (4.29) attain,

$$\dot{A}_x^{\pm} e^{\pm i\omega_{\pm} t} \pm i\omega_{\pm} A_x^{\pm} e^{\pm i\omega_{\pm} t} = -\omega_{\pm} A_y^{\pm} e^{\pm i\omega_{\pm} t} + k(V_x^+ - V_x^-) \tag{4.31}$$

Removing common exponential terms attain,

$$\dot{A}_x^{\pm} \pm i\omega_{\pm} A_x^{\pm} = -\omega_{\pm} A_y^{\pm} + k e^{\mp i\omega_{\pm} t}(V_x^+ - V_x^-). \tag{4.32}$$

The right hand side of the above equation can be expanded to yield,

$$\dot{A}_x^{\pm} \pm i\omega_{\pm} A_x^{\pm} = -\omega_{\pm} A_y^{\pm} + \frac{k_o}{2}\left(e^{i\omega_d t} + e^{-i\omega_d t}\right) \times e^{\mp i\omega_{\pm} t}\left(A_x^+ e^{i\omega_+ t} - A_x^- e^{-i\omega_- t}\right). \tag{4.33}$$

Therefore,

$$\dot{A}_x^+ + i\omega_+ A_x^+ = -\omega_\pm A_y^+ + \frac{k_o}{2}\left(e^{i\omega_d t} + e^{-i\omega_d t}\right)\left(e^{-i\omega_+ t} A_x^+ e^{i\omega_+ t} - e^{-i\omega_- t} A_x^- e^{-i\omega_- t}\right),$$

$$= -\omega_+ A_y^+ + \frac{k_o}{2}\left(e^{i\omega_d t} + e^{-i\omega_d t}\right) \times \left(A_x^+ - A_x^- e^{-i(\omega_+ + \omega_-)t}\right),$$

$$= -\omega_+ A_y^+ + \frac{k_o}{2}\left(e^{i\omega_d t} + e^{-i\omega_d t}\right) \times \left(A_x^+ - A_x^- e^{-i(\omega_o)t}\right), \tag{4.34}$$

where the relation $\omega_o = \omega_+ + \omega_-$ is used. Rearranging terms yields,

$$\dot{A}_x^+ + i\omega_+ A_x^+ = -\omega_+ A_y^+ + \frac{k_o}{2}\left(\; A_x^+\left(e^{i\omega_d t} + e^{-i\omega_d t}\right) - A_x^-\left(e^{i(\omega_d - \omega_o)t} + e^{-i(\omega_d + \omega_o)t}\right)\;\right). \tag{4.35a}$$

Similarly,

$$\dot{A}_x^- - i\omega_- A_x^- = -\omega_- A_y^- + \frac{k_o}{2}\left(\; -A_x^-\left(e^{i\omega_d t} + e^{-i\omega_d t}\right) + A_x^+\left(e^{i(\omega_d - \omega_o)t} + e^{-i(\omega_d + \omega_o)t}\right)\;\right). \tag{4.35b}$$

The above equations (4.35a,b) can be written in a "telescopic" form.

$$\dot{A}_x^\pm \pm i\omega_\pm A_x^\pm = -\omega_\pm A_y^\pm \pm \frac{k_o}{2}\left[A_x^\pm\left(e^{i\omega_d t} + e^{-i\omega_d t}\right) - A_x^\mp\left(e^{i(\omega_d - \omega_o)t} + e^{-(\omega_d + \omega_o)t}\right)\right] \tag{4.36}$$

A similar treatment for the equation of motion for $V_y^\pm$ yields,

$$\dot{A}_y^\pm \pm i\omega_\pm A_y^\pm = -\omega_\pm A_x^\pm \pm \frac{k_o}{2}\left[A_y^\pm\left(e^{i\omega_d t} + e^{-i\omega_d t}\right) - A_y^\mp\left(e^{i(\omega_d - \omega_o)t} + e^{-(\omega_d + \omega_o)t}\right)\right]. \tag{4.37}$$

The equations correspond to equation (50) in (Bollen 1990)

For very weak RF excitations (k_o small) at driving frequency close to ω_o, the motion consists of slowly varying amplitudes at frequency $\sim \omega_d - \omega_o$ plus additional high frequency components of $\sim \omega_d$ and $\sim 2\omega_d$. Considering just the low frequency components,

$$\dot{A}_x^\pm = \mp i\omega_\pm A_x^\pm - \omega_\pm A_y^\pm(t) \mp \frac{k_o}{2} A_x^\mp e^{i(\omega_d - \omega_o)t}, \tag{4.38}$$

$$\dot{A}_y^\pm = \mp i\omega_\pm A_y^\pm - \omega_\pm A_x^\pm(t) \mp \frac{k_o}{2} A_y^\mp e^{i(\omega_d - \omega_o)t}. \tag{4.39}$$

The solution for the above equations is given as,

$$A^+ = \alpha_1 e^{i\left(\frac{k_o}{2}t + \varphi_- + \frac{\pi}{2}\right)} + \alpha_2 e^{i\left(-\frac{k_o}{2}t + \varphi_- - \frac{\pi}{2}\right)} \tag{4.40}$$

$$A^- = \alpha_1 e^{i\left(\frac{k_o}{2}t + \varphi_-\right)} + \alpha_2 e^{i\left(-\frac{k_o}{2}t + \varphi_-\right)} \tag{4.41}$$

The x dimension motion for V^+ and V^- is thus attained from equation (4.29),

$$V_x^+ = \alpha_1 e^{i\left(\left(\omega_+ + \frac{k_o}{2}\right)t + \varphi_- + \frac{\pi}{2}\right)} + \alpha_2 e^{i\left(\left(\omega_+ - \frac{k_o}{2}\right)t + \varphi_- - \frac{\pi}{2}\right)} \qquad (4.42)$$

$$V_x^- = \alpha_1 e^{-i\left(\left(\omega_- - \frac{k_o}{2}\right)t - \varphi_-\right)} + \alpha_2 e^{i\left(\left(-\omega_- - \frac{k_o}{2}\right)t + \varphi_-\right)} \qquad (4.43)$$

Exploring a special case where $\alpha_1 = \pm\alpha_2$ introduces a simple but interesting solution that is shown below,

$$V_x^+ = \alpha_1 e^{i\left(\left(\omega_+ + \frac{k_o}{2}\right)t + \varphi_- + \frac{\pi}{2}\right)} + \alpha_1 e^{i\left(\left(\omega_+ - \frac{k_o}{2}\right)t + \varphi_- - \frac{\pi}{2}\right)},$$

$$V_x^+ \propto e^{-i(\omega_+ t + \varphi_-)}\left(e^{i\left(\frac{k_o}{2}t + \frac{\pi}{2}\right)} + e^{-i\left(\frac{k_o}{2}t + \frac{\pi}{2}\right)} \right),$$

$$V_{x(\alpha_1=\alpha_2)}^+ \propto e^{i(\varphi_- + \omega_+ t)} \cos\left(\frac{k_o}{2}t + \frac{\pi}{2}\right), \qquad (4.44)$$

and similarly

$$V_{x(\alpha_1=\alpha_2)}^- \propto e^{i(\varphi_- - \omega_- t)} \cos\left(\frac{k_o}{2}t\right). \qquad (4.45)$$

The graph, fig. 4.4, illustrates the interesting points about the motion. A "beat pattern" is observed indicating the conversion of magnetron (V^-) to cyclotron (V^+) motion and vice versa. The conversion period is given as,

$$T_{\omega_- \to \omega_+} = \frac{\pi}{k_o}. \qquad (4.46)$$

The driving frequency at $\omega_d = \omega_+ + \omega_-$ therefore effectively couples the radial magnetron and cyclotron motion, converting one completely into the other in a time $T_{conv} = \frac{\pi}{k_o}, \frac{3\pi}{k_o} \ldots \frac{(2n+1)\pi}{k_o}$. The applied RF electric field strength and the excitation period determine the "extent of conversion", where,

$$T_{conv} = B\frac{a^2}{2V_d}\frac{\omega_+ - \omega_-}{\omega_c}\pi. \qquad (4.47)$$
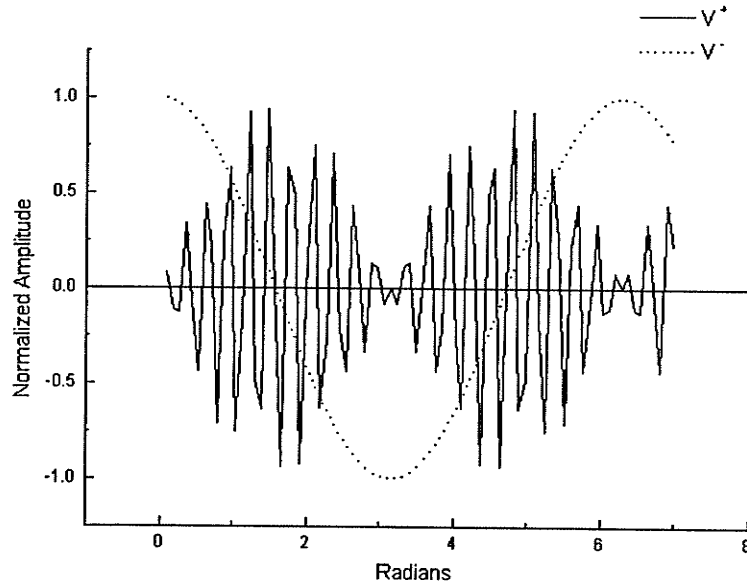
Fig. 4.4. Cyclical conversion mechanism of coupled magnetron and cyclotron motion. The plot is for a fictitious ion that completes 10 cyclotron orbits before completely converting to pure magnetron motion. The reader is advised that the cyclotron motion, in reality, is much more rapid.

The system radial energy is given by,

$$E_r\left(\omega_d\right) \propto V_d^2 \frac{\sin^2\left(\omega_b T_{RF}\right)}{\omega_b^2},\qquad(4.48)$$

with

$$\omega_b = \frac{1}{2}\sqrt{\left(\omega_c - \omega_d\right)^2 + \left(\frac{\pi}{T_{conv}}\right)^2} \ . \qquad(4.49)$$

From the relations (4.47 and 4.48) above it is instructive to note that for **any** T_{RF}, there exists more than one particular value for the RF amplitude V_d that enables complete conversion of the initial magnetron motion to cyclotron motion. The conversion is cyclical, in that, slowly increasing the applied RF field strength will bring about the conversion in distinct cycles. Energy profiles for various applied RF field strengths for a given T_{RF} are plotted in figure 4.5. The four figures show different RF field strengths stated as a ratio to the field strength that achieves complete conversion. It could also be noted that $\omega_- \ll \omega_+$, hence $\omega_+ \approx \omega_c$,

$$\Rightarrow T_{conv} \cdot V_d = \text{Constant} \qquad(4.47a)$$

This is helpful in scaling the RF excitation amplitude for different excitation times.

40
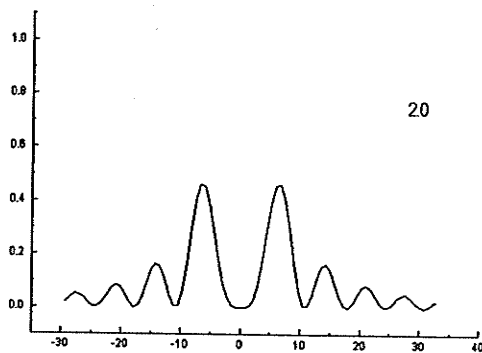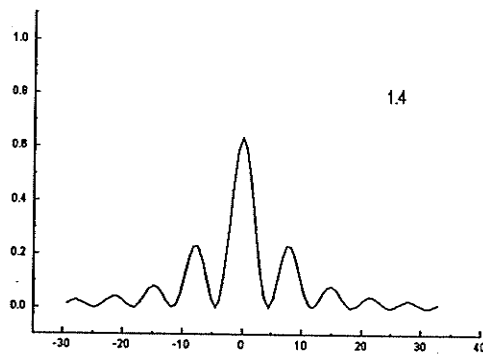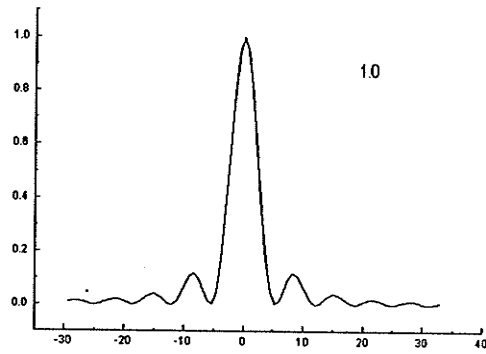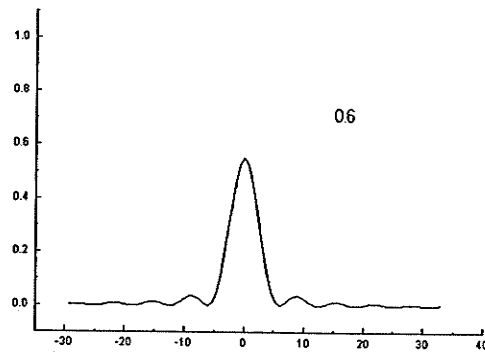
Fig. 4.5. Cyclotron energy variation with applied RF field strength. The RF excitation amplitude is stated on the top right hand corner as a ratio to the amplitude for complete conversion.

4.3. *TOF Detection*

The energy absorbed during RF excitation is implicitly the "measurable" quantity. Detecting the induced image currents due to the circulating charged particles in a Penning Trap is a means whereby mass measurements to $10^{\cdot 10}$ precision are attained on certain light masses (Cornell 1989). This method was not adopted in the CPTMS as "high precision" with the image current method can only result after really long detection times. This long measurement period is contrary to the "prompt" processes required for the mass measurement of nuclei far from stability.

Upon ejection, the cyclotron radial energy gained during resonance excitation is converted to axial energy, which is then detected in the arrival times of the ions at the detector. This conversion is attained when the ions traverse a region of inhomogeneous magnetic field during the exit process (Gräff 1980, Bloch 1953). The spectrum is traced by sequentially exciting at about 40 different frequencies centered on the ion resonant frequency. At the resonant frequency, the ions gain the most energy, and on ejection the resonantly gained energy shows up as a much shorter time of flight (Fig 4.6). The presence of side peaks or "sidebands" is due to the Fourier decomposition of the constant amplitude RF waveform applied for a short excitation time period,

$$\sin \omega_o t_{0 \to T_{RF}} = \sum_{n=0}^{\infty} a_n \sin \omega_n t + \sum_{m=0}^{\infty} b_m \cos \omega_m t \qquad (4.50)$$

Simply stated, even when the applied frequency is <u>not</u> at the resonant frequency, a small component of the resonant frequency is present in the applied waveform. This shows up as small "TOF dips" situated about the central peak.
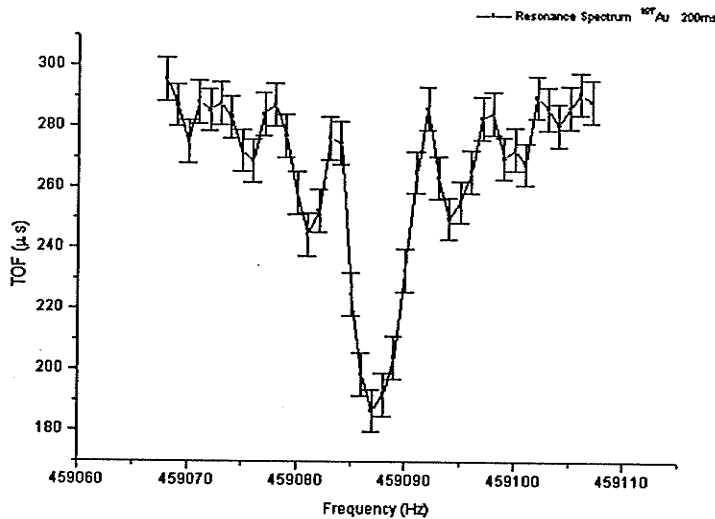
Fig. 4.6. 200ms ω_c excitation TOF spectra for ^{197}Au

Resolution is conveniently defined as the FWHM of the TOF profile. The FWHM is given by,

$$FWHM \sim \frac{0.89}{T_{RF}}. \qquad (4.51)$$

The resolution is therefore given as,

$$resolution = {f_c}\big/{FWHM} \cdot \qquad (4.52)$$

The above result indicates that for high-resolution measurements, the excitation period must be relatively long. Figure 4.7 illustrates this fact showing this difference between a 200ms excitation and a 1 second excitation. Operation at a resolution of 500,000 (1 second excitation) is considered routine with the CPT MS.
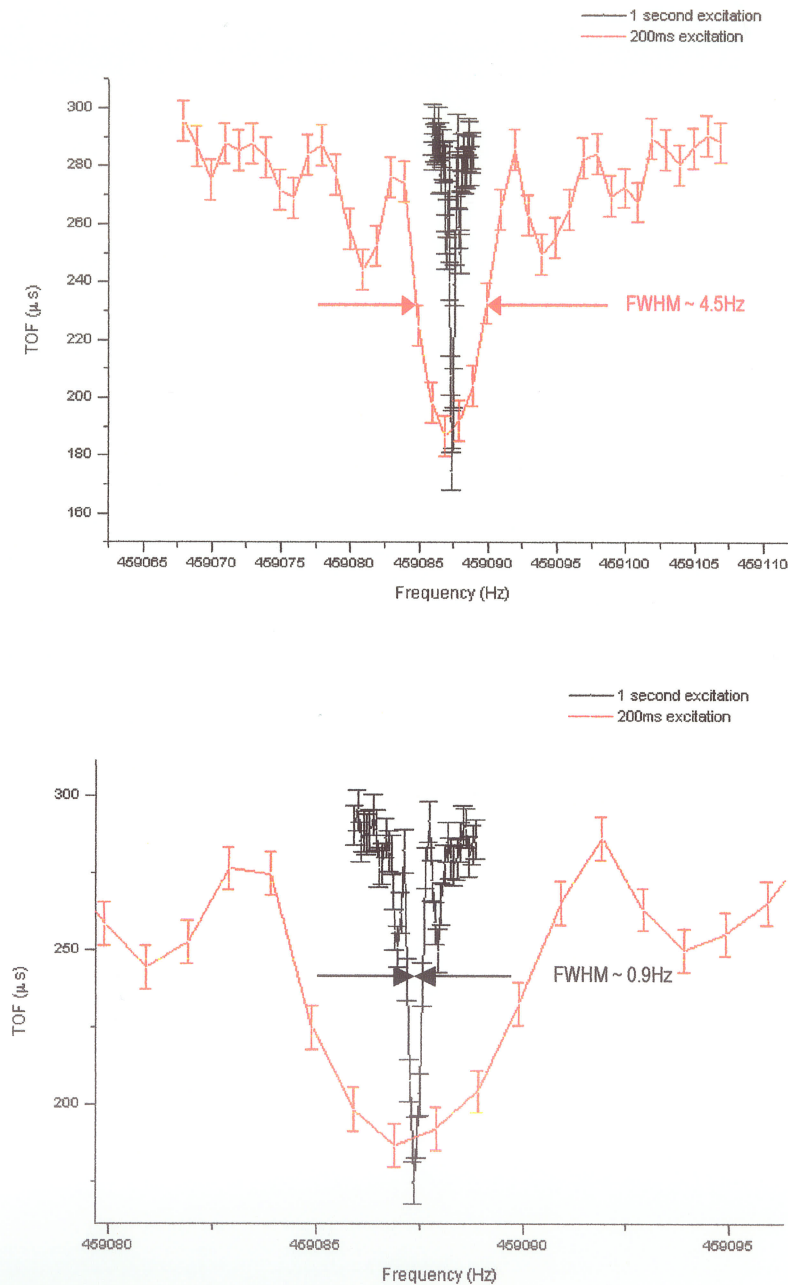
Fig. 4.7. The resolution of Penning Trap mass measurements with relation to excitation times

4.4. *Atomic Mass Determination*

The quantity determined is the cyclotron resonance frequency of the trapped ion species. This is a function of the ion charge q as well as the magnetic field B. It is an extremely complex process to determine the magnetic field to 10^9 precision. Because the field strength changes with time ($\sim 10^{-8}$/hr) a direct determination of the mass from the field strength is difficult if not impossible. Instead the frequency association with a calibration or reference ion species (equal charge) allows an ion frequency ratio $R = v/v_{ref}$ to be determined. The experimental atomic mass m can be attained with the reference atomic mass m_{ref} and the appropriate correction for the electron mass m_e.

$$m = \frac{1}{R} \cdot \left(m_{ref} - m_e\right) + m_e. \tag{4.53}$$

The electron binding energy in the order of a few electron volts may be neglected at the precision attained here. A point to note is that with the progress of Penning Trap mass measurements in the last decade, an upper limit precision of 500eV is readily attainable. An optimistic prediction would entail electron binding energies to be of consequence in the next few years, as much higher precision ($10^{-11} - 10^{-12}$) measurements become a reality.

4.5. *Ion Manipulation in Penning Trap*

Ion capture and ejection with the Penning Trap are vital processes in the overall mass measurement scheme. As elaborated in the instance of the RFQ trap, efficient conditions must be set for the ions to enter and leave the trap vicinity. The capture and ejection methods for the Penning trap bear some similarities to those already described for the RFQ trap. The presence of correction electrodes near the entrance and exit apertures requires some added consideration.
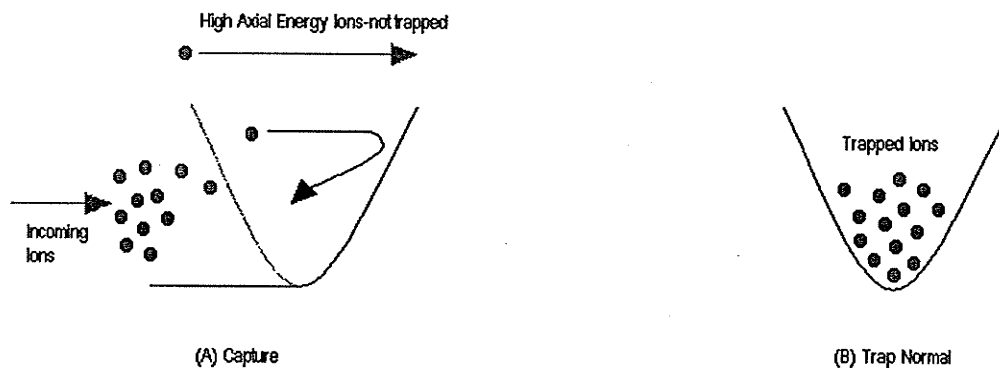
Fig. 4.8. Potential profiles for Penning Trap capture process

The ions arriving at the Penning Trap are "cool" bunches from prior processes in the RFQ Trap (*see Chap. 3 and Chap. 6*). The capture process requires no energy loss of the incoming ion bunch. This is in contrast to the RFQ Trap capture process where the inclusion of a buffer gas aids capture through energy moderating collisions between incoming ions and buffer gas atoms. For capture without energy loss, the incident ions must have axial energies less

than the potential well depth. Excessive axial energies will cause the ions to just skip over the trap. Thus the trap can only be open for a time span not exceeding the period of one ω_z oscillation (axial). In the instance of Au ions with a ω_z frequency of around 40kHz, the capture period is approximately 25μs. The capture principle basically involves "opening" the trap and "closing" it before the ions have an opportunity to be reflected out. Specific negative low voltage pulses are coupled to the entrance endcap and bottom correction electrode to allow ions into the trap. These voltages are removed after the capture period and the trapping potential returns to normal. The captured ion bunch is subsequently "cleaned" by removing those ions orbiting near the top of the trapping potential due to above average axial energies. This was originally achieved by pulsing the top correction tube so as to provide an exit path for the high-energy ions. The limited success of this method prompted the implementation of the "potential shallowing" technique, discussed in detail in chapter 6.7.

Ion ejection from the Penning Trap is achieved by "opening" the trap on the exit side. This allows the ions to slowly drift out. No large impulses are applied to the ions as only a slow drift across the inhomogeneous magnetic field can ensure complete conversion of the cyclotron energy to axial energy. Once again low voltage negative pulses are coupled to the exit endcap and top correction electrode. The ejection time period is not critical as long as the potentials are returned to normal after all the ions have exited the trap vicinity. Any premature "closing" of the trap might give trailing ions an extra impulse that will distort TOF information.
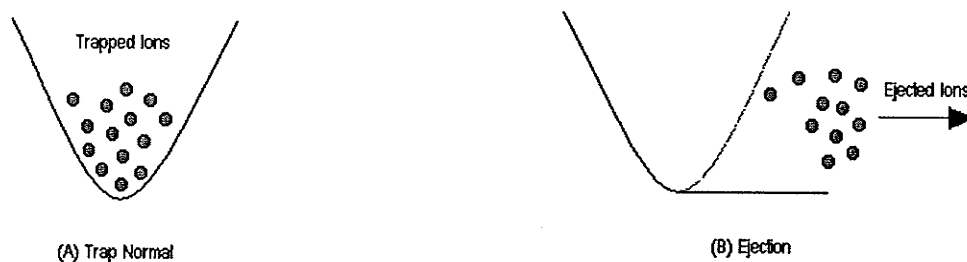
Fig. 4.9. Potential profile during the Penning Trap ejection process

Chapter 4. References

- Barillari, D. K. (1999). *PhD Thesis, The University of Manitoba*, Winnipeg, Canada.
- Bloch, F. (1953). Physica, **19**, 821.
- Bollen, G., Moore, R. B., Savard, G. and Stolzenberg, H. (1990). *Journal of Applied Physics*, **68**, (9), pg. 4355.
- Brown, L. S. and Gabrielese, G. (1986). *Review of Modern Physics*, **58**, 233.
- Cornell, E. A., Weisskoff, R. M., Boyce, K. R., Flanagan, R. W., Jr., Lafyatis, G. P. and Pritchard, D.E. (1989). *Physics Review Letters*, **63**, 1674.

- Fukutani, H. (2000). *MSc Thesis, University of Manitoba*, Winnipeg, Canada.
- Gräff, G., Kalinowsky, H. and Traut, J. *Z. Phys.* **A 297**, 35.

5 The CPT Mass Spectrometer

The CPT Mass Spectrometer is a system comprising various ion collection/transport devices. The "novel" elements are the ion collection devices and the precision mass measurement Penning Trap. A 5.9T superconducting magnet is used to provide a highly homogeneous field. A simplified overview of the CPT MS is shown below. The operation can be clearly categorized into "laser desorption" and "gas cooler" operation. The intrinsic difference between these two modes is the nature of the ion source. A laser is used to ionize stable atoms from a target. "Gas cooler" involves the transfer of exotic ions created during online accelerator operation or stable ions created from gaseous ionization within the gas cooler. A full description will be first made of the "laser ionization" set-up and a brief overview given for the gas cooler system.
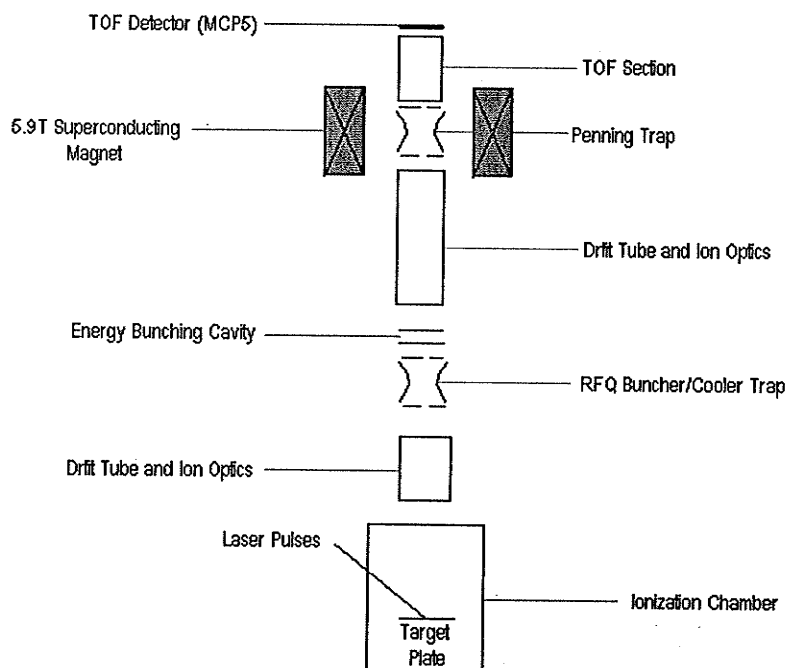
Fig. 5.1. Main Elements of the CPT MS System

5.1 *General Set-Up*

The laser ionization system consists of a YAG laser, operated in pulsed mode, and a configuration of mirrors and prisms that directs the beam onto the target plate. This plate holds three sample discs and an aperture, which allows for ion transfer from the cooler during online operation. A polarizer is included in the beam path to allow for intensity control. The entire beam path is shielded to avoid unwanted exposure to the human eye. Pulsed ionization is required as the RFQ buncher trap has periods of "closed" cycle (pulsed injection mode). Continuous laser operation will not be efficient with regards to RFQ trap collection efficiency.

TOF MCP#5

V-10

TOF LINE

MAGNET

PENNING TRAP

DECEL ELECTRODES

DRIFT TUBE

DRIFT TUBE

APERTURE #3

MCP#4

MAGNET MATCHING LENSES

QUAD 4

V-6

QUAD 3

DRIFT TUBE

MCP#3

APERTURE #2

QUAD 2

EINZEL LENS #2

APERTURE #1

RAMPED GAP & ACC. LENS

RFQ TRAP

MCP#2

IONIZATION CHAMBER

MCP#1

EINZEL LENS #1

YAG LASER

QUAD 1

DRIFT TUBE

DEFLECTOR #3

TO
TRANSFER
LINE
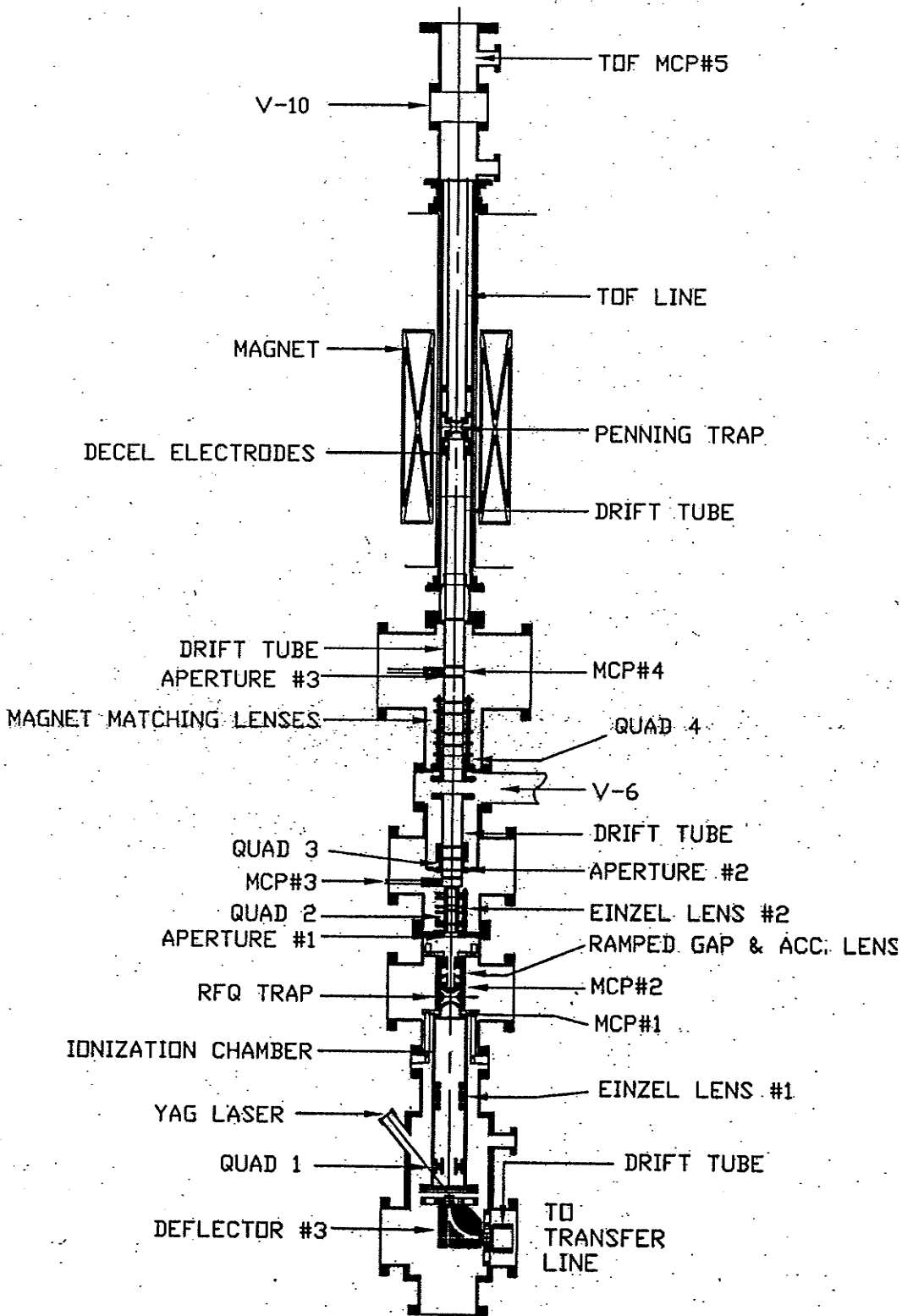
Fig. 5.2. The Complete CPTMS

48

Three extraction or "acceleration" plates set at a negative voltage ensure that the ions desorbed from the target material leave the vicinity of the target holder. A system of lenses and steering plates allows for deflection and focusing control of the resulting ion beam. The ion beam is directed towards the entrance aperture of the RFQ trap, which is used as an ion buncher/cooler. A deceleration electrode is employed just before the RFQ trap entrance aperture to allow for effective capture.

The RFQ trap has been elaborated in previous sections. Its primary use is to collect and cool the ions prior to injection into the precision Penning trap. Effective capture and subsequent ejection processes are crucial to ensure transfer efficiency. This is of great significance during online accelerator operation with low yield exotic species. The electrode structure is as shown in figure 3.4, with critical trap dimensions r_o=1.16cm and z_o=1.0cm. The entrance and exit apertures are 0.6cm each. A gas inlet is provided for filling the trap with buffer gas. Normal operation involves He gas at a pressure of approximately 1×10^{-5} torr within the trap enclosure. The RFQ trap is operated in pulsed mode, allowing for the capture of a predetermined number of "laser shots" as specified by the user. "Pulsing" the RFQ refers to the limited time in which the trap can accept externally injected ions. Medium voltage pulses applied to the endcap electrodes (Chapter 3) effect capture and ejection. The ion confinement field is derived from a HV square oscillating potential coupled to the ring electrode (Chapter 6.1). Figure 5.2 shows the current RFQ electronic setup.

The cooled/bunched ions ejected from the RFQ trap are directed through an "energy bunching" cavity. A high voltage time varying waveform is applied to the cavity to ensure energy bunching. Effective energy bunching is highly desired in order to produce an ion bunch that occupies a small z extent in the Penning trap. This would be of great consequence in the author's case as the magnetic field provided by the superconducting magnet is far from being ideal. The "energy bunched" ions are transferred enroute to the Penning Trap. A small aperture just before the Penning trap entrance endcap, pre-selects only those ions that possess limited off-axis trajectory. A final set of steerers and lenses is used to center the ion beam along the magnetic field axis before injection into the Penning Trap.

The Penning trap has an electrode structure similar to the RFQ trap, consisting of a ring electrode and two endcap electrodes with the dimensions r_o =1.16cm and z_0 =1cm. The endcaps have holes of radius 0.25cm to provide the ion entrance and exit apertures. The ring electrode is physically split into four quadrants to allow for multipole RF excitation (dipole/quadrupole). In order to maintain a pure quadrupole field within the precision trap enclosure, correction electrodes are incorporated in the design. The correction rings and correction tubes correct for the effects of the split ring and the endcap holes respectively. Biasing these electrodes at the appropriate potential ensures that the field within the trap remains fairly quadrupole in nature. The Penning trap is positioned in a region of ultra high vacuum (10^{-10} torr) and extremely strong magnetic field. This prompts the trap design to possess rather stringent requirements. The material used in the trap construction needs to possess a low magnetic susceptibility. This ensures that the trap itself will not distort the homogeneous magnetic field. OFHC (Oxygen Free High Conductivity) copper is chosen and precision-machined to tight tolerances so as to avoid possible field perturbations near the trap center (Fukutani 2000). The trap is plated with a thin layer of gold to avoid "patch effects" that arise from the eventual oxidation of exposed copper. The copper oxide patches would

cause any electric potential applied to the electrode to suffer from homogeneity. The Penning trap is housed within the molybdenum bore of the superconducting magnet (Appendix A1).

5.2 RFQ Trap Buncher/Cooler

The Radio Frequency Quadrupole Ion Trap is used as a "temporary ion store" before the ions are transferred to the precision Penning Trap for mass measurement. The addition of a buffer gas serves to "cool" the ions by energy moderating ion-gas atom collisions. Routine operation consists of driving the trap with an oscillating high-voltage (HV) electric field and supplying pulses to allow for ion capture and ejection.
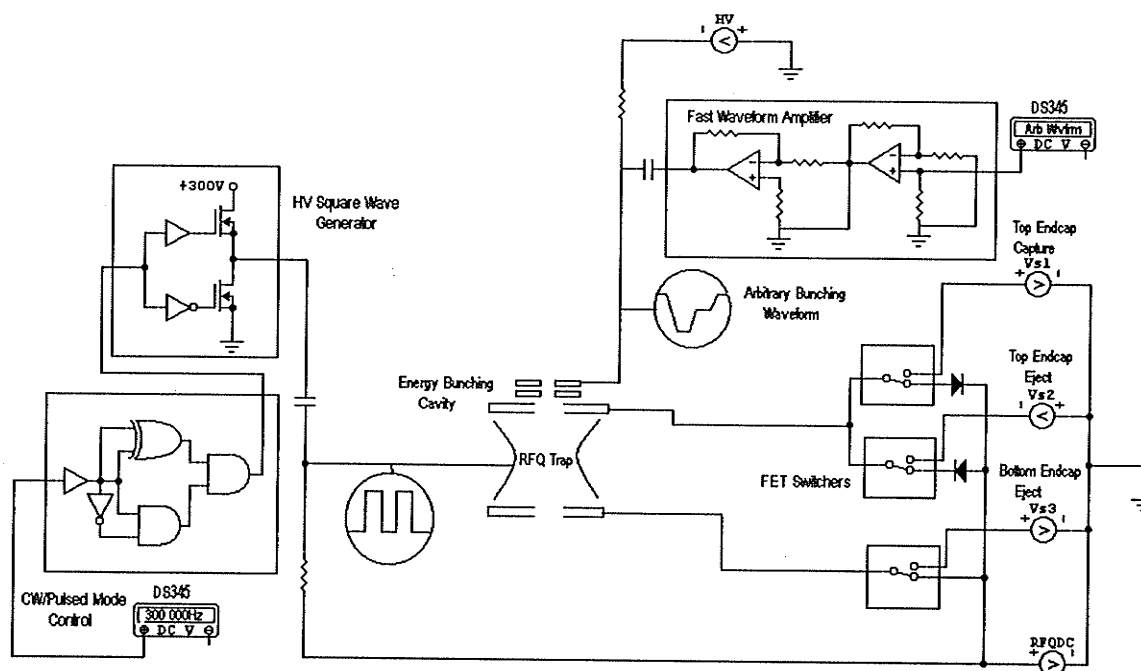
Fig. 5.3. Schematic of the RFQ Trap setup

The HV drive is a square waveform derived from fast switching MOSFETs. The square wave generator is designed for $450V_{pp}$ operation at a maximum frequency of 1MHz. The HV generation is based on the amplification of a low voltage TTL signal (see Chapter 6.1). This signal is derived from a Stanford Research Systems (SRS) DS 345-signal generator. Control of the HV RFQ drive signal is a feature added to the system recently (CW/Pulsed Mode control). This system provides the user with the option of "freezing" the square HV signal if the need arises (see 6.2). A simple AC coupling afforded by a capacitor and a resistor allows for the HV square waveform to be DC biased. The HV signal is applied to only the ring electrode while the endcaps sit at a predetermined DC level. The entire RFQ trap can therefore be "moved" to different potentials along the ion flight line. The capture/eject pulses are critically timed signals applied to both the endcaps. The pulses are normally of a few tens of microsecond duration and can range from 50V to 100V in amplitude. HV pulsers enable the endcaps to "switch" between the DC bias and the

required voltage for the capture and eject processes. Protective diodes are installed on the pulsers connected to the top endcap as shown to ensure that only one voltage is applied at an instant. An "energy correction" cavity serves to bunch ion energy prior to Penning trap injection (see sections 6.4 and 6.5).

5.3 *The Penning Trap*

The precision mass measurement takes place with specific multipole RF excitations within this trap. The trap design is more elaborate when compared to the relatively simple RFQ Trap. Besides the endcap and ring electrodes, correction electrodes are included to preserve the integrity of the quadrupole potential during operation (Chapter 4). Ion capture and ejection processes are no longer only restricted to applying fast pulses on the endcaps alone. The inclusion of correction electrodes around the vicinity of the entrance and exit apertures requires a slightly more detailed consideration of the capture/ejection process. However to present a comprehensive picture of the setup, it would suffice to state that low voltage pulses (18V max.) are required on the endcaps and correction tubes.

In order to obtain an accurate quadrupole potential within the trap, certain DC potentials must be applied to the ring, endcap and correction electrodes. The potentials are supplied by a precision 20-channel DC supply. Pulses (capture, ejection....) are derived as arbitrary low voltage waveforms from SRS DS345 waveform generators and amplified. The coupling of all signals (DC, pulses and RF small signal) to the respective electrodes is performed in an AC coupling box. The RF excitation sequence involves both dipole and quadrupole modes and a variety of distinct frequencies (plus a scanning frequency for ω_c excitation). DS345's provide the RF signal, which is transferred to a 5-channel solid-state-relay based "frequency selector". The sequentially timed triggers select only one frequency, which is passed to a "phase inverter".

The output supplies the in-phase (ϕ) and anti-phase ($\bar{\phi}$) signals required for the multipole excitations. The coupling of the alternating signal phases to the respective ring quadrants is performed by the relay-based "phase selector". A number of 30V summing amplifiers provide the capability to couple two or more signals to one electrode. This is the case for the top endcap and correction tube, where both "evaporation" and "ejection" pulses are applied to these electrodes (at different times).

Improvements in this work involve the introduction of fast JFET solid state switches to replace formerly "mechanical relay" switching systems (see Chapter 6.6). A novel method of pre selecting "cold" ions prior to mass measurement has also been commissioned in this work (see Chapter 6.7). Figure 5.3 shows a complete electronic set up of the Penning trap.
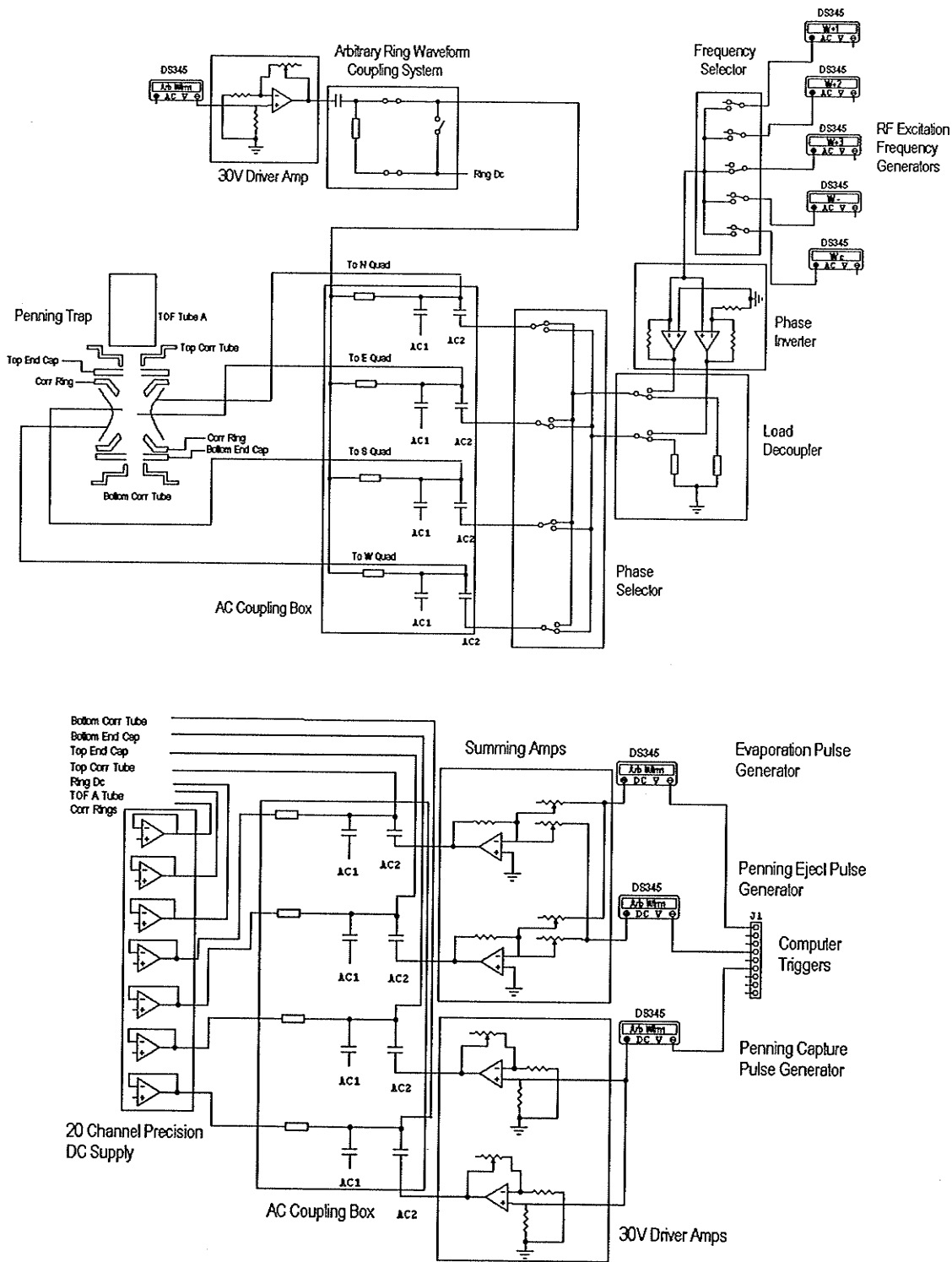
Fig. 5.4. Schematic of the Penning Trap setup.

5.4 *Ion Detection*

Ion detectors are situated at critical points throughout the spectrometer to monitor the transmission of the ions through the apparatus. Micro-channel plates (MCP) were chosen as the "ion counters". The signal produced by these detectors is proportional to the number of ions incident of the detector face. This enables the user to alter the lens/steerers potentials until the signal is maximized, indicating optimized transmission. The relative positions of the detectors are shown in the figure 5.4.
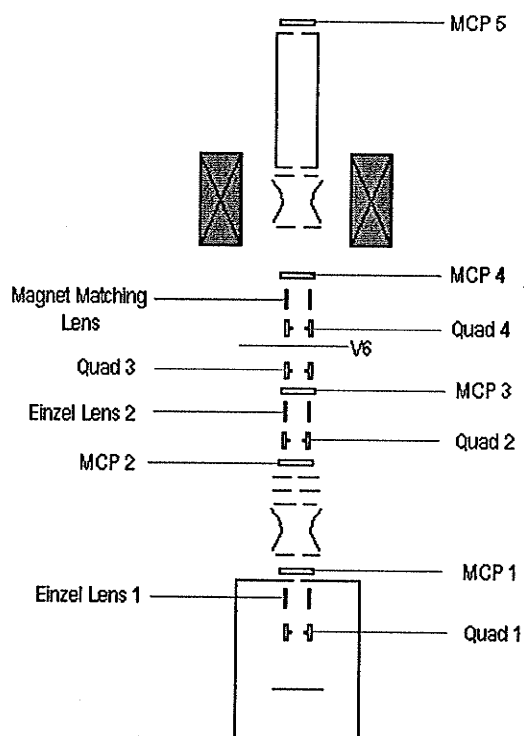
Fig. 5.5. Relative positions of ion optic elements and ion detectors in the CPT MS

The positions of the focusing elements are also indicated in figure 5.5. The MCP detectors are mounted on retractable plungers that are moved into position to attain ion signal readings and then removed from the ion flight line. A small section of drift tube, mounted on the same plunger provides for continuous ion transmission otherwise. MCP 5 is the final TOF detector. This detector provides the TOF data of the ions ejected from the Penning trap after RF excitation, and therefore, is mounted as a rigid fixture. The steerers, Quad 3 and 4 are critical in ensuring that the ions adopt a parallel trajectory along the magnetic field lines, prior to entering the Penning trap.

5.5 Gas Catcher/Cooler Exotic Harvest System

Provisions have been made for the transfer of ions from another remote "ion source". This enables "exotic" or radioactive ions, created during online accelerator operation to be transferred to the CPT MS for mass measurement. A brief description of the setup will be presented here. Gaseous atoms (e.g. Xenon stable isotopes) can also be ionized within the chambers before transfer to the spectrometer. The figures below show the critical elements in the gas cell/ion guide design.
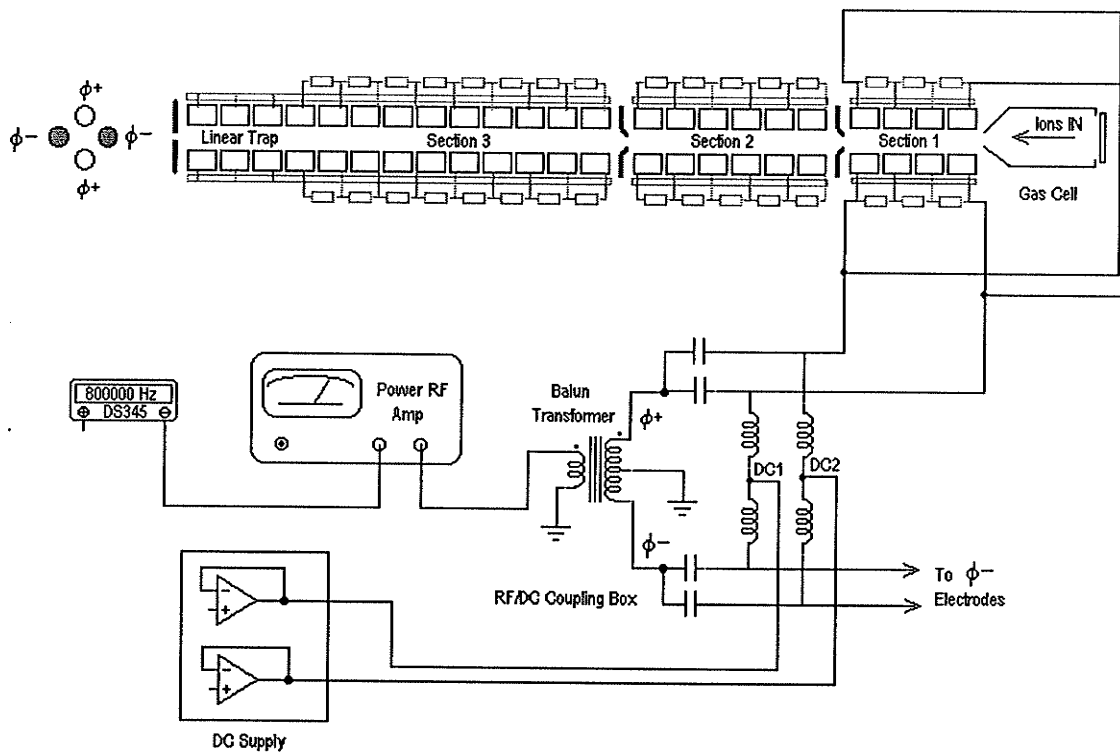
Fig. 5.6. Typical electronic configuration for an ion guide/mass filter section.

The Gas Cell, filled with Helium buffer gas, stops incident radioactive ions. These ions are then extracted via an "assisting" DC gradient together with gas flow. The next stage consists of a configuration of 3 ion guide sections separated by apertures. All sections possess similar characteristics in that they all are operated with HV RF electric fields in conjunction with a "draw-out" DC gradient. The ions are then collected in a "linear trap" before being ejected as an ion bunch. The figure above shows a typical electronic setup for an ion guide section. Proper operation requires both RF and DC fields to be applied to the electrodes. Coupling capacitors provide a low impedance path for the RF drive signal to the rod segments while resistors establish the required DC gradient. High voltage RF is achieved through amplification of a very low voltage signal provided by the SRS DS340/345 signal generator. The power RF

54

amplifier, ENI 240L provides about 50dB gain with a flat band response from 20kHz to 10Mhz, well suited for the operation regime. The coupling box includes a transformer, which conveniently achieves a balanced signal from unbalanced (single end) input from the power amplifier which is then DC biased employing inductors (Fig. 5.5). DC1 and DC2 set up the "draw-out" gradient. The opposing electrode pair is connected similarly to phase ϕ_-. The linear trap however requires no DC gradient. Routine operation can involve section 2 configured as a mass filter. A DC offset is placed on the electrodes to effect mass selection (Boudreau 2001).
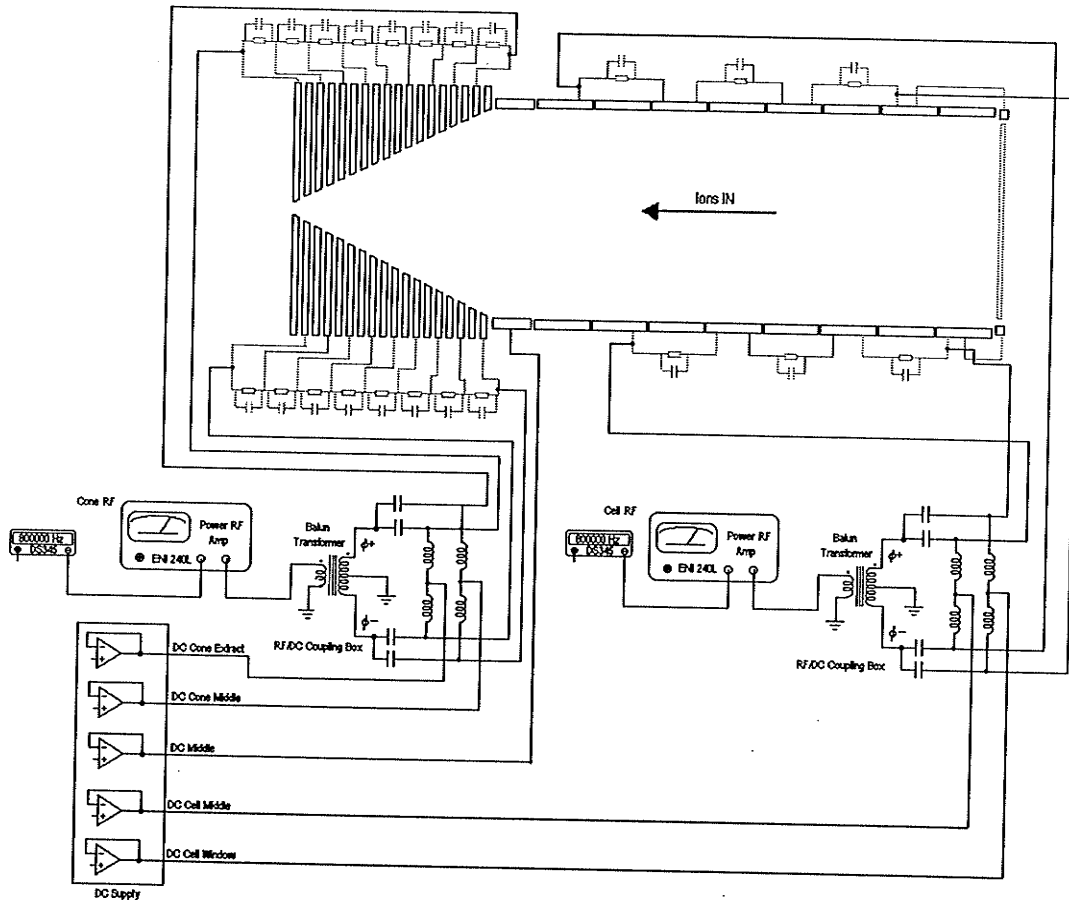
Fig. 5.7. Schematic of the Fast Gas Filled Catcher

The Gas Cell is composed of stacked cylindrical sections to allow for alternating phase HV RF as well as a DC gradient. The coupling is similar to that described for the ion guide. The exit cone or nozzle is also a system of precision-machined stacked plates. The plates are arranged in an order of decreasing internal diameter as shown in fig. 5.6. The resulting form is an exit nozzle with RF/DC gradient capability. It can be seen from the diagram (fig. 5.6) that alternating plates have RF offset in phase by π radians. DC voltages are derived from a dedicated 20 channel "Ion Cooler" DC Power Supply.

The transport tube contains a set of three spherical deflectors that steer the ion beam through 90° each, allowing for transmission through the aperture in the target plate located within the CPT MS ionization chamber. These ions then follow a similar path as the ions, laser desorbed from the target plate. A series of lenses and steerers once again provide control over transmission. A system of four orthogonal plates, located just before the final spherical deflector, is operated as a "pulsed deflector". Ions are mass selected through TOF by applying a critically timed HV pulse (see Chapter 6.3).
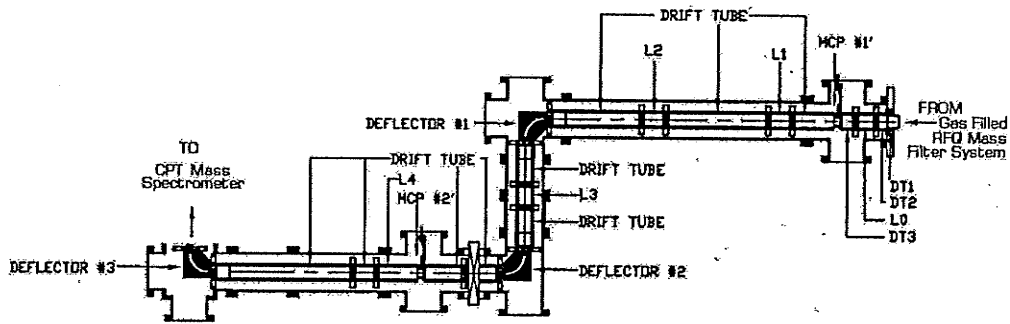
Fig. 5.8. The transport section coupling the Exotic Harvest System to the CPT MS

Chapter 5 References

- Boudreau. C. (2001). *M.Sc. Thesis, McGill University*. Montreal, Canada.
- Fukutani, H. (2000). *M. Sc. Thesis, University of Manitoba*. Winnipeg, Canada.

6. Electronics Improvement/Modifications

The CPT MS is a relatively new instrument assembled at ANL in 1997. The first precision mass measurements made on this machine in 1998/1999 (Fukutani 2000) provided a test of the system behavior. This was crucial as improvements made in this work came as a direct result of these early mass measurements. The commencement of online operation initiated the CPTMS as a complete functioning spectrometer. Experience with the actual operation invariably dictates the need for modifications beyond the "original design". This chapter will highlight the electronic improvements and their motivations.

The author has adopted a simple strategy for all the designs mentioned below. The "plug and play" approach allows for future upgrades with minimal operation inconvenience. The "breakaway" character provides the user with the flexibility to perform system tests with and without the device in question with relative ease. MOSFET design technology is discussed in considerable detail as MOS devices are currently being used in high voltage equipment built in house. A comprehensive record is deemed prudent when dealing with a 1500V-isolated device capable of pulsing 350V in 40ns.

6.1. *High Voltage, High Frequency (HVHF) Direct Drive System*

The introduction of power MOSFETs (Metal Oxide Semiconductor, Field Effect Transistor) signaled a departure from the traditional bipolar junction transistors (BJT), the workhorse of the electronics industry. The performance of MOSFETs is generally superior to bipolar transistors when considering characteristics like speed, breakdown voltage and thermal effects. The drive circuitry has also become simplified in the form of single chip integrated circuits that possess built in "level shifting" of up to 600V .The ability to drive both "high" and "low" side devices with a single driver has been realized. These drivers outperform totem pole configurations commonly used in conjunction with bipolar transistor circuitry (Simpson 1987).

The interest in power MOSFETs in the field of ion traps and guides stems from its high frequency switching characteristic, which could be used as the basis in the design of a high voltage, high frequency (HVHF) rectangular waveform generator. This generator would eventually be the direct rectangular drive element for various rod sections in ion guides and trap electrodes in RFQ traps. The apparent draw towards a direct drive system arises fundamentally from the elimination of the presently available cumbersome transformer coupled sinusoidal drive circuitry. The transformer coupling introduces some form of intrinsic resonant behavior that prevents operation over a wide frequency range. Any change in operational frequency is normally accomplished by altering circuit element values (capacitance/inductance) in a tuned (tank) circuit (Jones *et. al.* 1997). Thus RFQ device operation has never been based on the principle of frequency scanning. The introduction of rectangular waveform direct drive systems will usher in the era of frequency agile RFQ devices.

The other disadvantage of transformer coupled RF drive systems is the difficulty to operate in a pulsed mode. The field cannot be interrupted without the adverse effect of feedback or oscillation. Several groups have devised ingenious methods to pulse sinusoidal high voltages (Mosburg *et. al.* 1987,Rocher *et. al.* 1998, Fulford *et. al.* 1979).

Pulsing direct drive systems would definitely come at a lower cost in development time and energy. It has shown that it is possible to achieve effective operation of an ion guide with a rectangular waveform as the confining radio frequency field (Richards *et. al.* 1973). The duty cycle of the waveform employed has also been shown to possess some mass filtering ability. Any mass filtering capability in radio frequency quadrupole ion guides (specifically termed as quadrupole mass filters) is presently achieved with a separate dc supply coupled to the sinusoidal RF field. The elimination of a separate dc supply, while still retaining a fair degree of mass selectivity, is very desirable. Currently, the RFQ trap which is being used as an ion accumulator / cooler in the CPT system at Argonne National Laboratory is driven by a square waveform direct drive system using fast switching MOSFETs, designed and built by Dr. Sidney Gulick at McGill University, Montreal, Canada.

  The square waveform direct drive system is built on the principle that fast power MOSFETs may be used as ideal switches. Here two power MOSFETs are configured to switch alternately, i.e. each is on or off half the time (for square waves) but never on at the same time. This technique is commonly incorporated in RF power efficient amplifying devices classified as Class-D RF Amplifiers. The sinusoidal RF output is attained through the implementation of an output harmonic filter, which removes all the higher order harmonics from the square signal, leaving only the fundamental frequency (Gottlieb 1993). The ideal power efficiency arises from negligible transition or switching time. The ideal fully on MOSFET state is construed to possess zero resistance between the source /drain channel and similarly, for the off state, this resistance is infinite. No power is consumed in both these states. Thus power loss can only occur during switching time, which therefore must be minimized (Andreycak 1998). The circuit schematic is as shown in Fig 6.1.
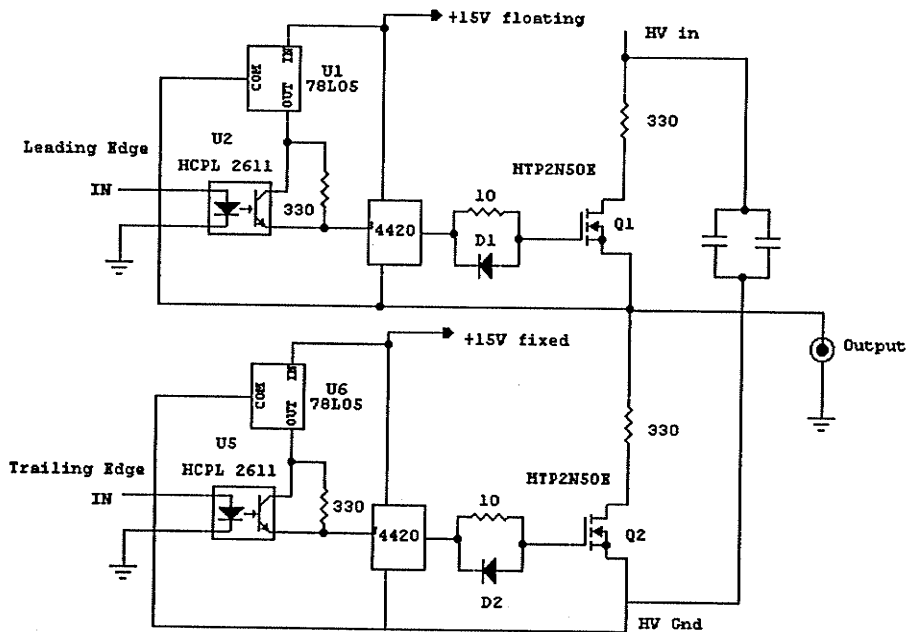
Fig. 6.1. High Voltage, High Frequency Direct Drive System

The switching MOSFETs are Motorola MTP2N50E with a maximum voltage rating of 450V. The switched output is taken from the common source Q_1 and drain Q_2 junction. It can be noted that the large, almost infinite off resistance of the MOSFET holds the switched state without adverse leakage currents. For example when Q_1 conducts, the source is at HV less a small potential drop due to a finite on resistance. This indicates that the drain of Q_2 is also at HV while the source is at ground potential. This clearly indicates the need to adhere to the maximum drain to source breakdown voltage $V_{DS-Max} = 450V$. This then sets maximum permissible output of this particular drive system as $450V_{pp}$. This design could be extended to higher output voltages by using power MOSFETs with a higher maximum rating for V_{DS} (e.g., Intersil RFP4N100 $V_{DS} = 1000V$).

The configuration of MOSFETs in a HVHF switching circuit is somewhat determined by operational parameters. The simplest scheme would be to use a complementary pair, i.e, one n channel and one p channel. The design consists of identical configuration of circuit elements on two sides, a high side floating at HV and a low side referenced to ground potential. Each side is isolated and self contained with dedicated power supplies. The n-channel is used as a low side switch and the p-channel is subsequently used in the high side. The only complication with this method is the requirement of a floating power supply for the high side .The drains of both MOSFETs are connected, from which the output is derived (Fig. 6.2).
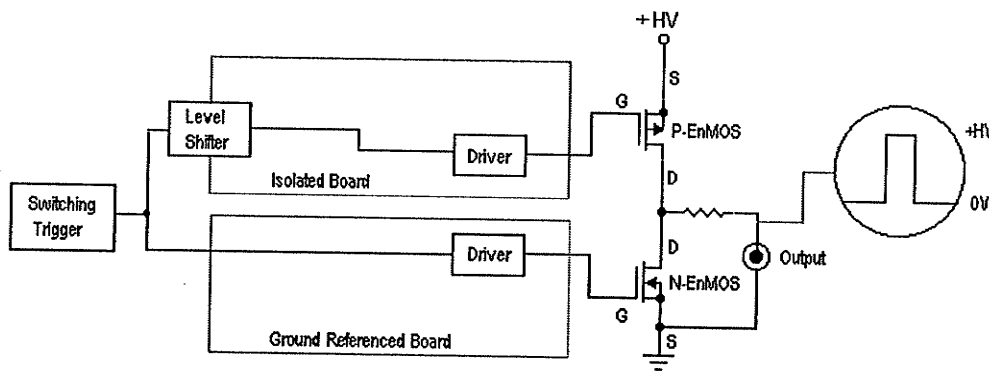
Fig. 6.2. Schematic of complementary pair MOSFET switcher circuit.

The drawback in a complementary pair design is that the p-channel power MOSFET suffers from a large gate to source internal capacitance and maintain a greater on resistance. These are due to device construction and the fact that the p carrier mobility is less than that of the n type. These characteristics are manifested itself in slower switching times and greater power dissipation within the transistor. As a result, p-channel MOSFETs are rarely used in HVHF applications (Int. Rectifier App Notes). The p-channel is not available at a V_{DS} rating of 1000V, therefore any switching design in this range warrants a two n-channel switching system. The two n-channel-switching configuration is possible with some additional circuitry. Proper operation can only result from coupling the source of the high side device to the drain of the low side device. This junction becomes the output. The low side operation is similar to that described for the complementary pair method. The high side however is not truly a *high side*. The high side device has its source connected to the output. The maximum gate to source potential, V_{GS}, is rated at 30V. This indicates that for V_{GS} to remain within the mandated range, the *high side* must be referenced to the output. The

high side therefore floats alternately between HV and ground. The *switching* of the high side reference requires that the floating power supply transformer have isolation rating of at least HV. The parasitic capacitance between the primary and secondary coils must be low to ensure that during switching, the potential at the source and the gate always stays within the rated V_{GS}. Currently n-channel MOSFETs are readily available at a maximum rating of V_{DS}=1200V.

The square waveform generation is a relatively simple process of turning on one transistor at a time. The output is at HV when the high side MOSFET is conducting and the output is ground during the low side conduction phase. Thus the output is a square waveform with an amplitude of V_{pp}= HV. The switching of the respective MOSFETs are triggered by TTL signals. These triggers are complementary, as it is required that only one MOSFET is made conducting at a particular instant. The basic TTL trigger is afforded by a frequency generator that controls the switching frequency, which ultimately sets the frequency of the HV square waveform. The complementary signal can be obtained by simple inverter logic (leading edge/trailing edge triggers). These triggers are passed to the respective isolated boards. Since the TTL triggers are ground referenced signals, the trigger for the high side has to be *level shifted*. Level shifting is achieved through the use of an optoisolator, Hewlett Packard HPCL 2611, with isolation rating of 600V. This is used as a trigger receiver on both boards to improve noise immunity and eliminate ground loops.

A direct digital delay is added to one of the trigger lines. This is to prevent simultaneous conduction in both MOSFETs. Since the thresholds for turning on and turning off are different, there might be an instant where one transistor crosses the conduction threshold before the other transistor has fallen below the turn off point. This would result in an instantaneous path to ground through both conducting transistors and large currents would be drawn from the HV supply. The built in delay prevents this undesirable event from occurring. The received trigger signals, now referenced to the respective board "reference" potential, are conveniently transferred to the MOSFET Gate Drivers (MGD). The gate driver used is the Telcom 4420 with a maximum rated drive current of 6A. To ensure adequate thermal management, the TO-220 package is used which provides the option for heat sinking.

Special consideration must be given to power management at the design stage to ensure the constituent devices do not exceed operational limits. Power losses in MOSFETs can be subdivided into switching losses and conduction losses. Switching losses arise from the simultaneous presence of the drain current, I_D and drain source potential drop, V_{DS} during transition, while conduction loss is brought about by a small "on" resistance. Controlling these losses can be done by careful attention to device parameters. Switching losses can be reduced by making state transition times as brief as possible with a high current gate driver. This would minimize the overlap between drain current and V_{DS} (Andreycak 1998). Conducting losses can be curbed by selecting a MOSFET with a low "on" resistance and by ensuring "full enhancement". The capacitive load (rod sections or trap electrodes) must be included before a complete computation of MOSFET power handling requirements can be performed. The charging of the load capacitance at HVHF is an extremely power consuming process. A simple calculation ($\frac{1}{2}CV^2$ x 2f) puts the MOSFET power-handling requirement at 250W for a 1000V waveform switching at 1MHz through a load capacitance of 500pF. This is an enormous strain for any power transistor. The load capacitance includes the MOSFET parasitic drain to source capacitance, which is a characteristic of metal oxide device construction. It is

therefore crucial to effectively heat sink MOSFETs for HVHF switching operation. A ducted fan ventilation system would provide forced air cooling to alleviate excessive thermal stress that might otherwise lead to critical device failure. Currently power MOSFETs in the semiconductor market have a maximum power rating of around 300W. This may prove to be a limiting factor in the design of higher frequency drive systems.

6.2. Pulsed Mode Operation for HVHF Direct Drive System.

Operating the HVHF Direct Drive System in a pulsed mode is made feasible by the control of the driver TTL signals. The TTL signal with the two logical states can be made to remain *state* locked for a period of time as required by the user. The locked signal is then transferred to the HVHF system for *amplification*. The design of the HVHF system dictates that the two states of the output waveform (Fig. 6.4) is either ground (LOW) or HV (HIGH). The logic nature of the trigger signal prevents locking the output at any other intermediate voltage level. The output waveform is AC coupled to the RFQ electrodes. The electrodes can thus be locked HIGH (+½HV) or LOW (-½HV) to allow processes to occur without the effect of rapidly changing field configuration within the electrode region. The state lock (pulsed mode) is triggered and maintained by a TTL pulse originating externally. Delay elements like the monostables (74LS123) provide a small variable delay between the trigger signal and the execution of state lock .The rest of the design is straightforward logic through the use of common integrated circuit elements. The primary "RF" input is derived from a high frequency waveform generator (Stanford Research DS340) set to deliver a TTL signal at a prescribed frequency. A selector switch S1 provides the option for operating in pulsed or CW mode. All input and output signals are buffered using standard 74LS244 buffers/drivers. The output selector switch S2 sets the state lock to either HIGH or LOW (Fig. 6.3). The logic level output is then passed on to the HVHF Direct Drive System for high voltage waveform generation. The HVHF Pulser was originally designed for the ion ejection process but could be easily modified to control both injection and ejection. The Fig. 6.5 shows a proposed circuit that could be used to lock the drive signal for both the injection and ejection processes. A third channel is shown to allow for expansion.
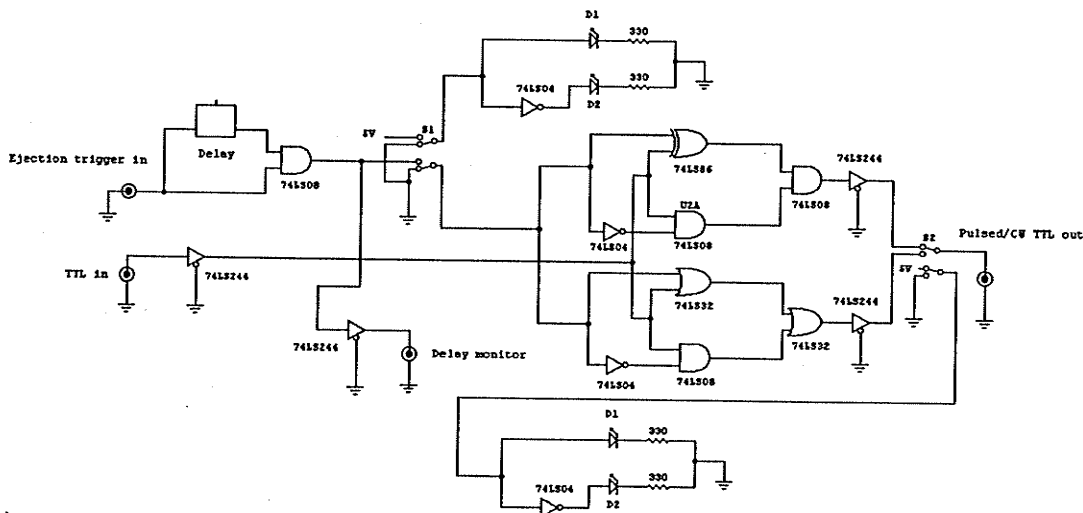
Fig. 6.3. Direct Drive Pulser
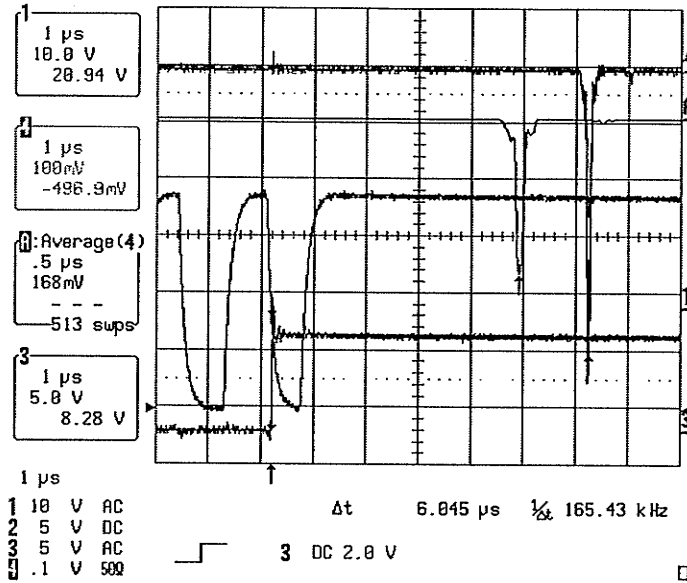
Fig. 6.4a. Oscilloscope traces showing *square RF* of 350V$_{pp}$ at a frequency of 600kHz applied to the ring electrode. The HIGH state lock is initiated a short time after the ejection pulses are engaged. The ejection trigger is shown as trace 3 with the ejected ion signal as trace 4 .The capacitive loading clearly distorts the square waveform at high voltage, high frequency operation.
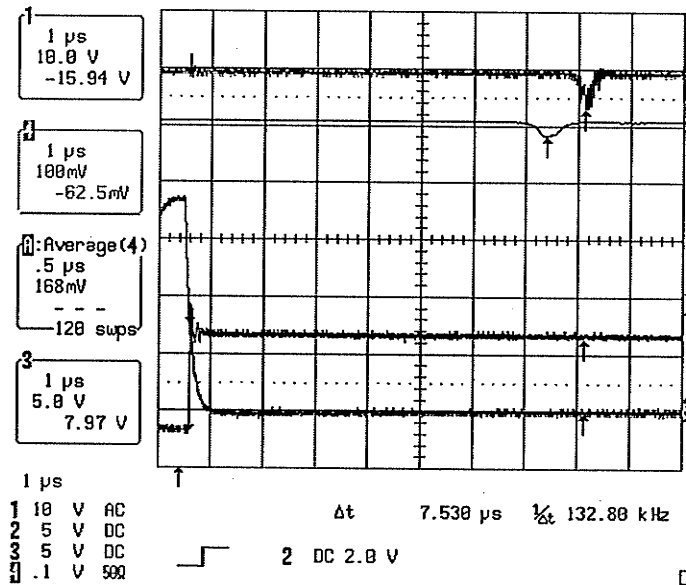
Fig. 6.4b Similar conditions as in (a) but with the LOW state lock initiated .It can be noted that the ion signal is much weaker indicating an unfavorable ejection condition. The sustained defocusing effect of a ring held at negative potential during the ejection process causes the positive ions to be drawn <u>away</u> from the exit aperture.
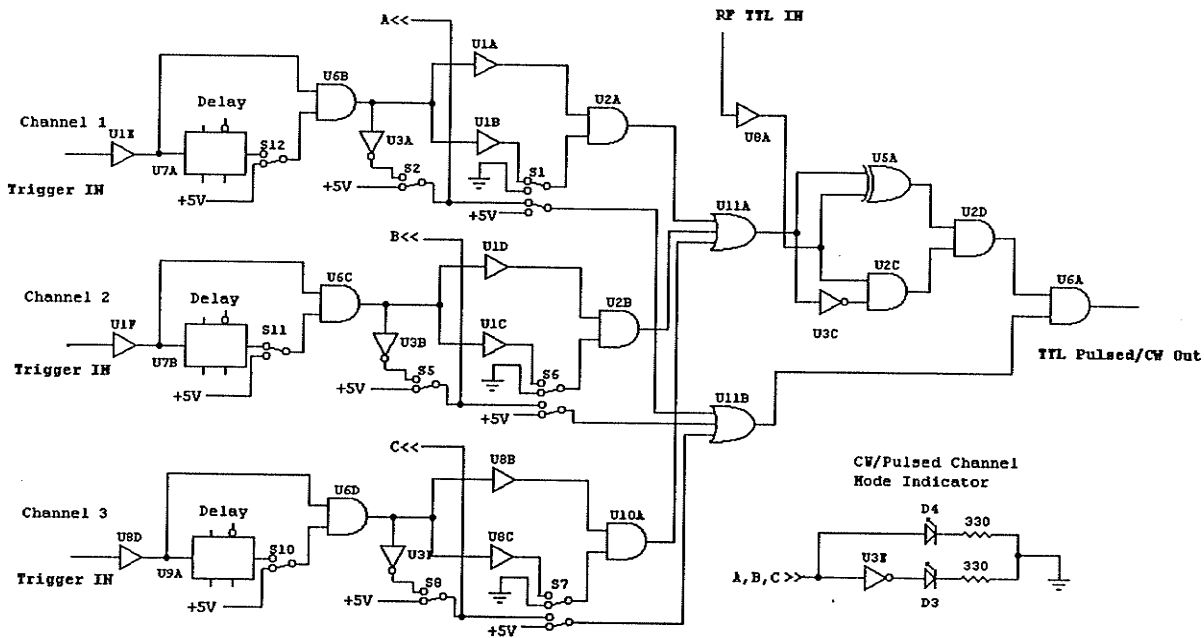
Fig. 6.5. Proposed Multi-Channel Pulsed/CW Mode Control Circuit

6.3. *High Voltage Fast Pulser.*

Manipulation of ion beams often requires very fast pulses in the sub-microsecond regime. These pulses can range from a few tens of volts to kilovolts. The voltage required depends on the task at hand and the nature of the ion beam. The transit time of a particular ion beam through a cavity in question determines the applied voltage required to produce a particular change in the beam character. Pulse width becomes crucial in cases where the ion beam consists of more than one species and the effect needs to be species specific. The requirement for fast pulses biased at HV in the region of kilovolts is common in ion beam experimental/industrial equipment. The uses range from pulsed ionization with electron guns to pulsed extraction to generate temporally bunched beams. The pulses can have a simple rectangular waveform or more elaborate time varying structures. In any case, the reason for pulsing is to deliver a time dependent voltage that affects the ion beam in a desired manner.

High voltage pulses can be generated using certain amplifiers. The amplification process is relatively straightforward and construction is a well-documented process. The cost of high voltage fast amplifiers however, can run in the hundreds of dollars per integrated circuit. A simpler and more cost-effective solution can be achieved by using high voltage MOSFETs. The circuit configuration consisting of a complementary pair of MOSFETs has been previously highlighted (section 6.2). The MOSFETs are once again employed as a "switch". The switching is performed between two isolated voltage levels. The isolation is achieved with isolation transformers rated to 2500V. The switching FETs are rated with a maximum drain to source voltage (V_{DS}) of 450V. It is therefore possible to switch between two voltage levels biased at approximately 2000V, and separated

63

by 450V. The design was originally conceived and built by Mr. Leo Ninniken at McGill University. These "switchers" currently provide pulses for ejection/capture processes for the various ion-trapping devices in the CPT system. The new design (Fig. 6.7) embraces a similar concept except for the FET drive circuitry. Recent developments in solid state technology have made "small footprint" high current MOSFET gate drivers a reality. The performance of these devices is far superior to bipolar junction transistors (BJT). These drivers have been designed to replace BJTs thereby reducing parts counts as well as minimizing "valuable" circuit board area. The entire circuit including the isolation transformers is made to fit on a 7" by 4" board (Fig. 6.8) This circuit will be a prototype for printed circuit boards in the near future.

Online accelerator operation for the production of exotic nuclei currently produces a large number of ions from organic contaminants. A fair degree of "decontamination" is necessary in order to ensure the purity of the injected ions into the Penning Trap. Mass selection with respect to time of flight (TOF) is attained through the use of a pulsed deflector. The deflector electrodes are four steel plates that are held at drift tube potential during the very short transit time of the mass under experiment (Fig 6.6). All other masses are deflected away from the transmission axis by one plate (shaded) held at about 350V lower than the drift tube potential. A resolution of 1-2 amu can be observed with a pulse of about 350V with a time-width of 800ns (Fig.6.9). The pulse rise time is modestly rated at 60ns. This translates into a slew rate exceeding 4000V/usec. Very few power linear amplifiers can boast such operational parameters.
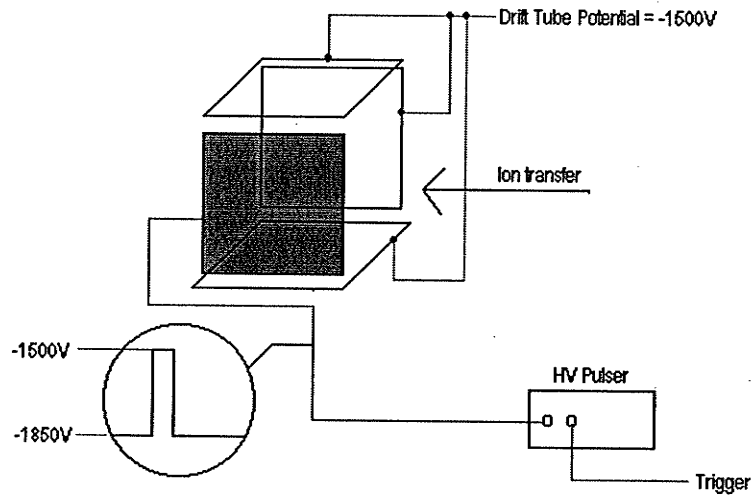
Fig. 6.6. TOF based Pulsed HV Mass Selector
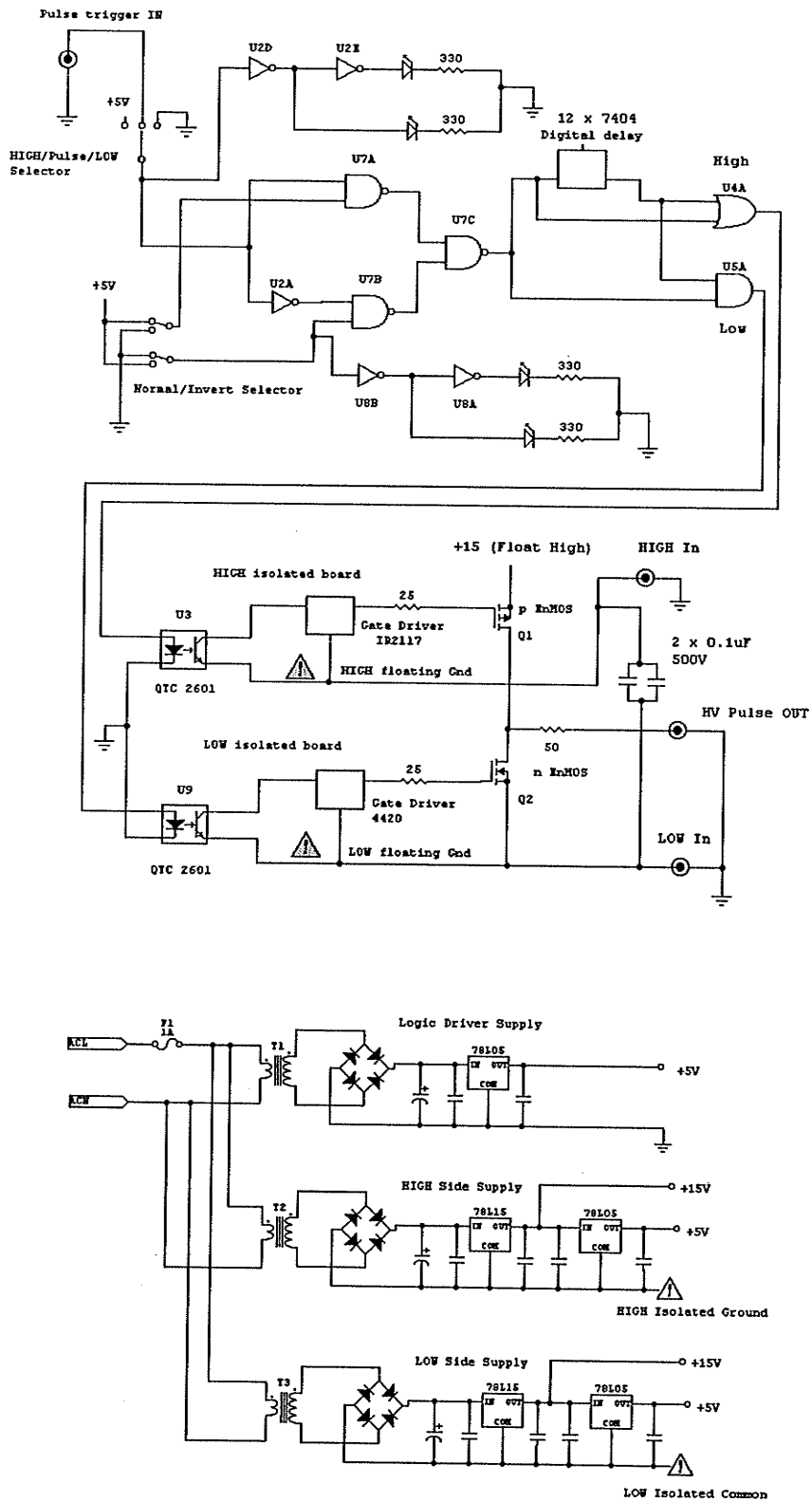
Fig. 6.7. CPT Pulser Schematic
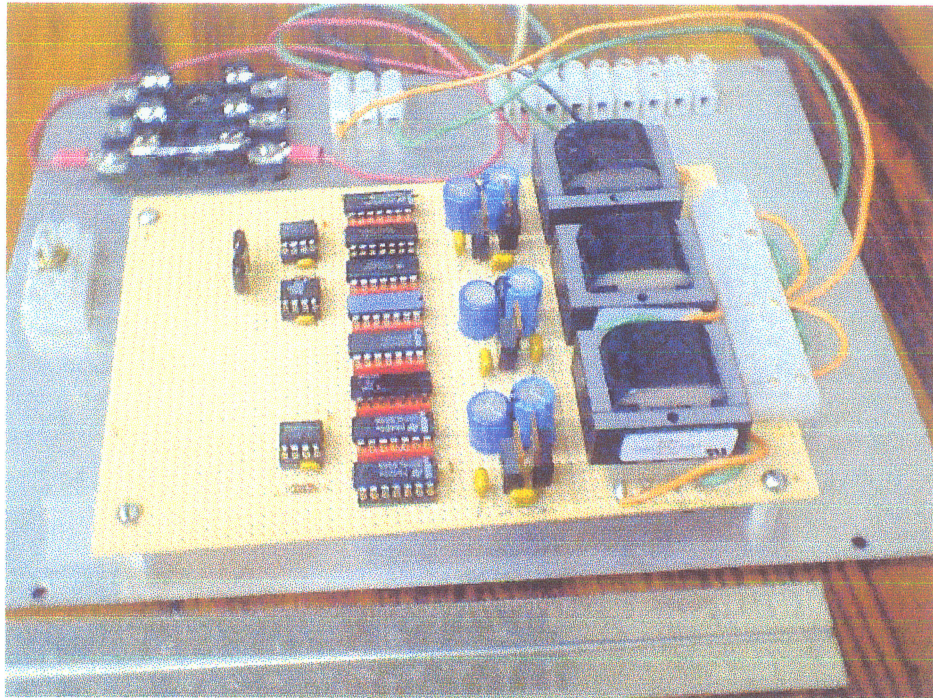
Fig. 6.8a. Circuit board on test bed. The 2500V isolation transformers are visible on far right
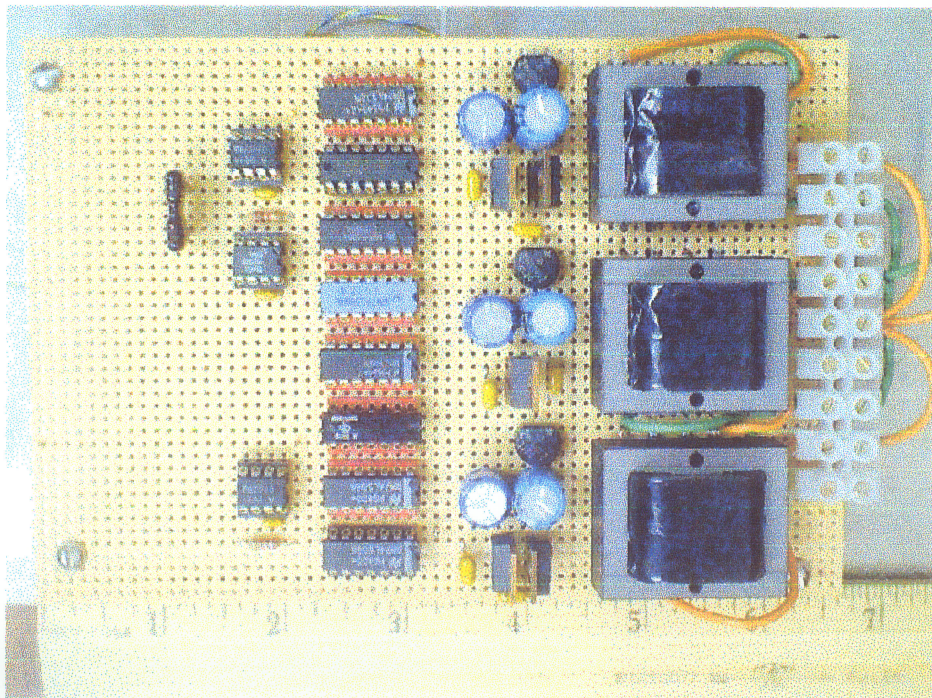
Fig. 6.8b. Entire circuit board area is a compact 7" x 4". Switching MOSFETs are not yet inserted.
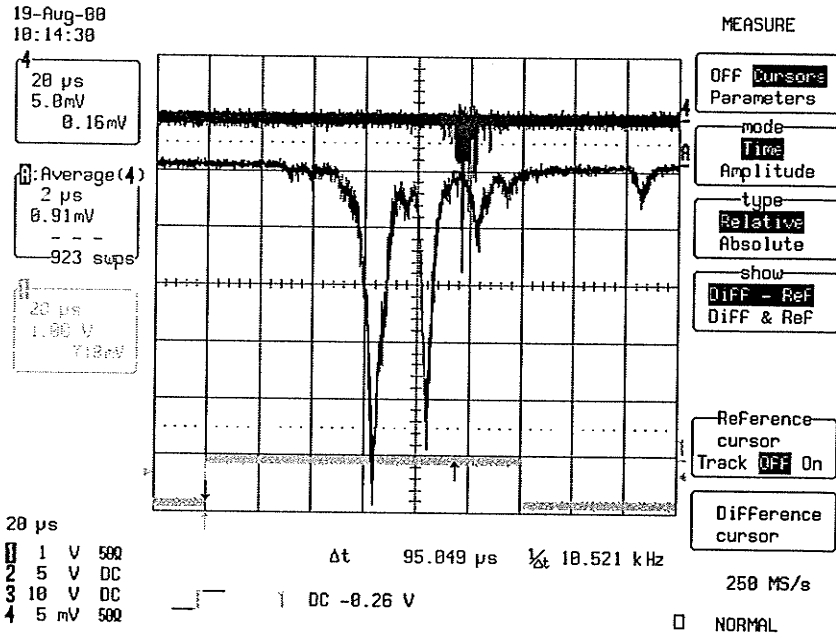
Fig. 6.9a   Spectrum at MCP1 shows organic contaminants over a wide mass range due to ionizing primary beam entry into gas cell.
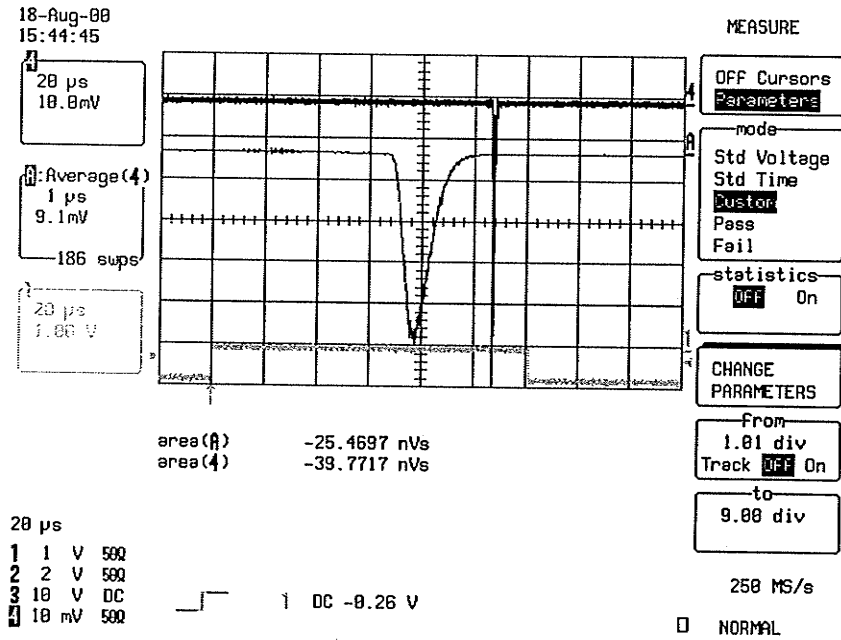
Fig. 6.9b.   Operation of Pulsed Mass Selector- A resolution of 1amu is a compromise between contaminant rejection and exotic transfer efficiency

6.4. *In-flight Ion Energy Bunching.*

Energy bunching of the ion bunch prior to Penning trap injection is a "mission critical" process. An ion bunch with a large energy spread can fill the entire trapping volume. This results in a portion of the trapped ion cloud occupying regions of the magnetic field where the inhomogeneity is suspect. This would have adverse effects as the magnetic field itself defines the mass measurement. The figure below (Fig. 6.10) shows the different possible filling instances of the Penning trap. A poorly energy-bunched ion beam consists of ions with a wide range of axial incident energies. The capture process involves no energy loss. The trapping process is therefore successful for all ions that possess axial energies up to the trap depth. Ions with above average energies execute orbits near the top of the trapping potential. The orbit radial extent is large therefore these ions probe a greater region of the magnetic field.
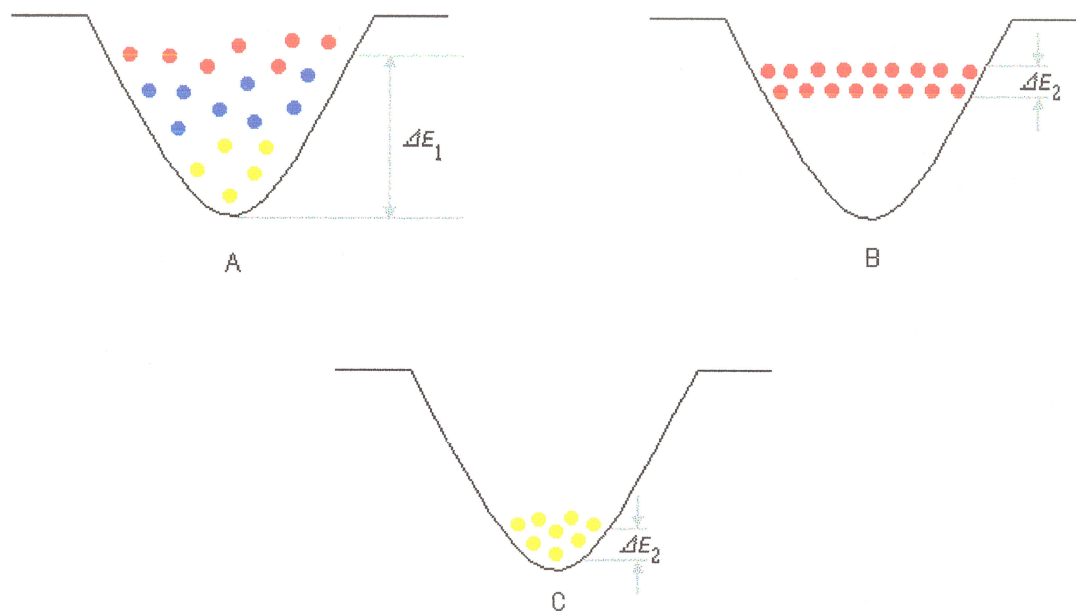
Fig. 6.10. (A) An ion cloud with a large energy spread being trapped. A large extent of the trapping volume is filled. (B) An energetic ion cloud with a small energy spread being trapped. (C) The cloud in (B) can be made to enter just slightly above the trap center by merely altering the potential of the ion source (RFQ trap in the case of the CPTMS instrument).

On the other hand, low energy ions move very close to the trap center in tight orbits. These ions experience fields of the highest homogeneity. The magnetic field as well as the electric quadrupole potential has inhomogeneity that increases with distance from the trap center. It is therefore wise to ensure the ions trapped in the Penning trap have energies only slightly above the trapping potential minimum. A tightly energy bunched beam is a prerequisite to this goal as now the trap user can merely alter the potential of the "ion source" to bring an energetic but energy-bunched ion beam to be trapped just slightly above the trap center. The author has devised a means to circumvent the energy-bunching requirement by pre-selecting a certain part of the ion cloud (see Chapter 6.7). This relaxes

the need for tight energy- bunching but the tradeoff is transfer efficiency. This limits spectrometer performance during online mass measurements where production rates are very low.

An ion bunch is normally characterized by its dynamic properties (x, p). It is crucial in all ion beam experiments to achieve some sort of control of these coordinates. One obvious method is focusing, where transverse spatial coordinates are compressed to facilitate transmission through beam elements. Energy "focusing" or bunching is another criterion whereby the energy spread ΔE of the ion beam is decreased in-flight. Phase-space dynamics once again can be used to understand the mechanism. The Liouville theorem prescribes the conservation of phase-space, which relates ΔE and Δt or conversely, Δx and Δp. For motion along the z-axis, the following holds true:

$$\Delta E_z \Delta t = \Delta p \Delta z.$$

This indicates that any bunching in energy is accompanied by an increase in time spread and vice versa. In ion beam experiments time or energy bunching is considered paramount. An example of "time" bunching is in heavy ion linear accelerators, where the ion beam is accelerated through the use of pulsed RF accelerating gaps. In order for effective acceleration, all the ions must arrive at the acceleration cavity at the same time (Humphries 1986). A pre-buncher is precisely employed for the purpose of "time" bunching.
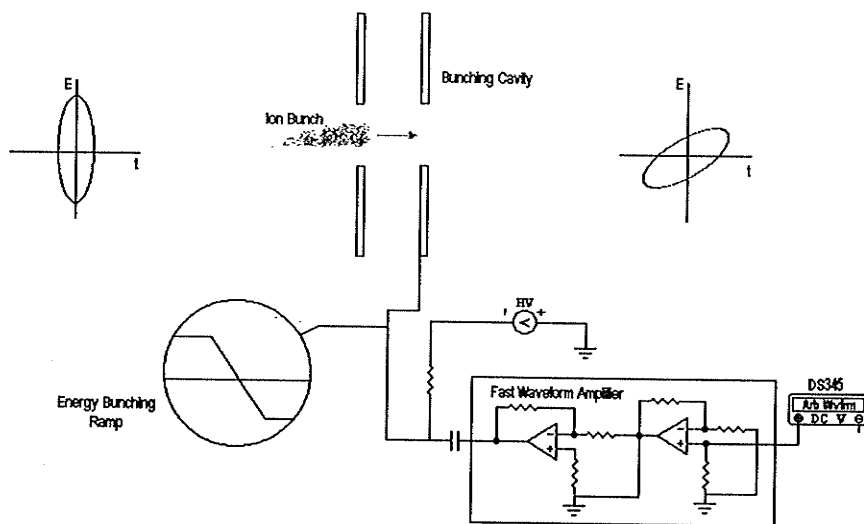
Fig. 6.11.   Set-up of the In-flight Energy Bunching System. Phase space before and after the bunching cavity shows an ion cloud bunched in energy at the expense of an increased temporal spread.

The CPTMS requires an ion beam tightly bunched in energy. A time spread of a couple of microseconds can be accommodated during the Penning Trap injection process. The simple principle of energy bunching is to accelerate slower ions while retarding the faster ones. Briefly, an ion bunch with a large energy spread traverses through the bunching cavity and on exit, their energy spread is decreased. An ion bunch traversing through a region of static electric fields would maintain their inherent energy spread as each ion gains or loses the same amount of energy. To correct energy spread; a dynamic field is required. The ramp is the simplest example of a dynamic field. The ramp is set to slew more negative with time, thus more energetic ions arriving earlier would experience less

acceleration than slower ions arriving later (Fig. 6.11) .The result would be ions bunched together in energy. The need for different ramp slew rates is prompted by the varying transit times of different masses through the ramp cavity under similar ejection conditions. Lighter ions would be traveling faster in general and over a short distance would be closely bunched in time. To achieve the same "degree of bunching" the ramp should fall faster. The Fast Ramp Amplifier design allows for a maximum slew rate of 220V/μs.

The ramp requirements for the RFQ ejection parameters were attained primarily from SIMION (Dahl 1995) simulations. An ensemble of about twenty ions trapped in the RFQ Trap was ejected with pre determined ejection phase and amplitude. The individual ion energy and TOF is extracted from the simulation data. A particular "bunching" ramp is then inserted into the computation and the simulation is run again. The effect of the ramp can be observed from the energy spread of the ions on exit. A technique using the Penning Trap electrodes as a retarding lens is then used to confirm the results experimentally. The following figures, 6.15 and 6.16, illustrate simulation and experimental results for cases of ion energy spread, with and without the energy-bunching ramp. The author credits Dr. Guy Savard and Mr. Jason Clark for setting up the simulations as well as performing the energy spread tests.

6.5. *Fast Ramp Amplifier.*

The Fast Ramp Amplifier is a replacement for the Penning Trap "Energy Bunching" Power Amp in operation till June 2000. The change was necessary to improve on the slew rate as well as eliminate parasitic oscillations that were so rampant in the latter amplifier. The Fast Ramp Amp is configured to operate on a single negative supply so as to maximize the voltage range of the output. The amplifier used is the PA85 from Apex Microtechnology. It is a high power bandwidth, high voltage MOSFET operational amplifier designed to operate on from ±225V supplies. The state-of-art MOSFET technology enables very fast switching with a maximum slew rated at 1000V/μs. An important consideration for single supply operation is that waveforms with an output voltage of greater than 200V might be required depending on the mass species being transported. Operating with twin symmetric ±225V will definitely put a severe limitation on the voltage swing, as amplifier saturation is imminent for any output approaching the supply voltages. Most power op amps are suitable for single supply operation but the common mode voltage range (CMVR) does impose some limitations (Apex 1999). One of these is that the input voltage does not reach within 12V of either supply rail i.e. $(V_- - 12) < V_i < (V_+ - 12)$. The true "single" supply operation with ground, as the positive rail would not be possible here as the input waveform is a ground-referenced signal. A simple alternative to this is to have a second low voltage supply +15V to adhere to the CMVR. Violation of this requirement would invariably lead to a loss of linearity. This alternative could be realized by the use of an encapsulated DC supply external to the amplifier housing. Symmetric supply amplifiers operating from ±V will have an output baseline at 0V. Current operation is with supply rails at +15V and –300V. The inputs must therefore be biased so as to provide the output with as much room to swing as far negative as possible. Resistor chains with a 1.5kOhm, 5kOhm resistors provide an output DC baseline of approximately –

80V, leaving enough swing to achieve an output of –200V comfortably. This choice of resistor combination was due to the limited resources available at short notice. The resistors are high power resistors, as they have to dissipate a combined power of 15W. The resistor chain biasing itself needs to draw 48mA of current. The power supply chosen for the negative rail thus has to provide at least 150mA with ease to the complete circuit. The Sorenson DCS600-1.7E with its maximum ratings for voltage and current of 600V and 1.7A respectively was chosen and easily configured as a negative supply.

The amplifier is set with a total fixed gain of 25 in two x 5 non-inverting configurations (Fig. 6.12) .The input signal is provided by a waveform generator operating as a low Z (impedance) driver. Since the amplifier inputs are high Z, there is a further gain of 2 at the inputs. This gives an overall gain of 50. The choice to use two stages with a low gain each instead of the more economical single high gain stage was prompted by the need for wide bandwidth, low distortion techniques in employing MOSFET power amplifiers. The power response for the PA85 indicates that at high gain, the bandwidth decreases. Therefore to maintain the high frequency components as far as possible, it was decided to employ two stages each with a low gain. Wide bandwidth was a major concern in this design as the signal undergoing amplification is an arbitrary ramp. The ramp, on Fourier decomposition will ultimately consist of very high frequency components. It would be wise if the design could allow for a bandwidth of approximately 5MHz. Any severe loss of high frequency components would invariably lead to more rounded transition edges and therefore a decrease in slew rate .The other concern was amplifier stability. Since the waveform is composed of many frequency components – it was crucial that no oscillation occurred at any of the constituent frequencies. Great care was taken to decouple the amplifier power supplies with capacitors so as to prevent noise and oscillation due to cross coupling between the different stages. The components were mounted right on the amplifier leads in an attempt to minimize lead inductance ("inverted bug" construction-Fig 6.14b) .The system fared extremely well on bench tests with an oscilloscope load. However when connected *in situ* to the trap, oscillations began to occur .The capacitive nature of the load coupled with a source of inductance forms an oscillatory LC, high Q, tank circuit. This circuit exhibits a resonance at a particular frequency f_o , where $f_o = 1/\sqrt{(LC_{load})}$ and if f_o is one of the constituent frequencies in the waveform, oscillations occur. Great effort was taken to minimize stray inductance in the circuit. The capacitance of the load, C_{load}, is intrinsic to the design and set up of the RFQ Trap and the adjoining Ramp Correction Cavity. A very simple way to arrest the oscillation is to remove the "offending " frequency. This can be performed easily with the use of slew -limiting filters. These are RC low pass filters, which limit high frequencies. The breakpoint is set at 3MHz .The tradeoff for stability is slightly rounded edges and diminished slew rate. The PA85 is rated for 1000V/µs but the operational requirement for the amplifier slew rate is at the extreme, 300V/ µs. Thus slew rate limiting is not expected to compromise experimental specification.

The design lends itself easily to future modifications. Changing the values of the biasing resistors could alter the output dc baseline. Positive high voltage ramps are possible with current circuit configuration. The power supplies however need to have reverse polarity. The negative supply becomes –15V while the Sorenson DCS600 could be set up to deliver positive high voltage. Any sort of "seriously" bipolar signals (voltage swings in both directions) need dual supplies. A method to circumvent this requirement while still maintaining the ease of single

supply operation is to use AC coupling to set the bias point externally. This method requires an external high voltage channel, which can be provided by a High Voltage Supply Mainframe for example, the LeCroy 5440.
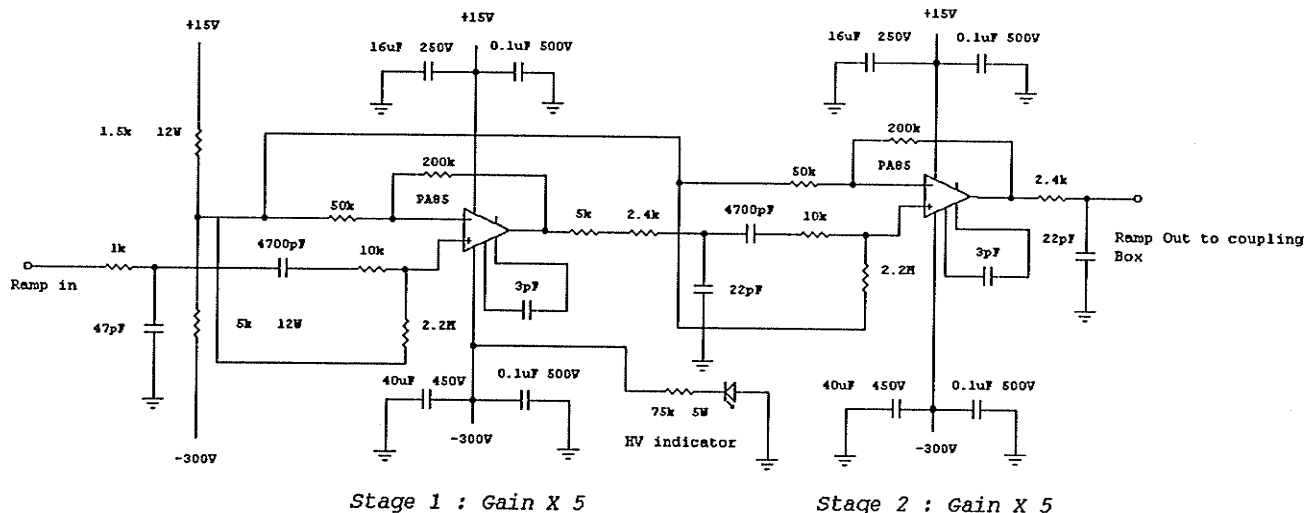
Fig. 6.12.   Fast Ramp Amplifier
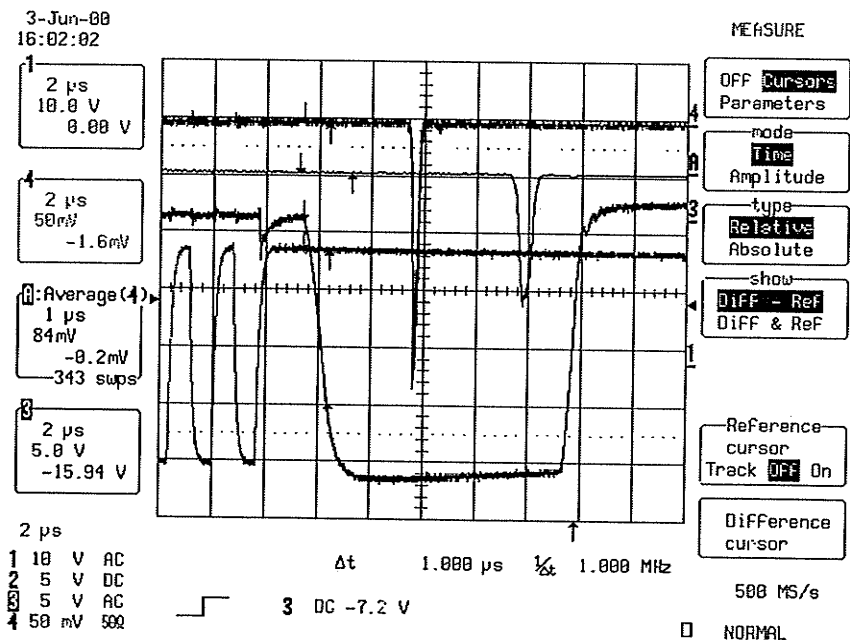
Fig. 6.13.   Oscilloscope trace (x10 attenuation) showing a ramp waveform of 160V/usec coupled to the cavity. The other traces are the RFQ drive waveform and the ion signal

72
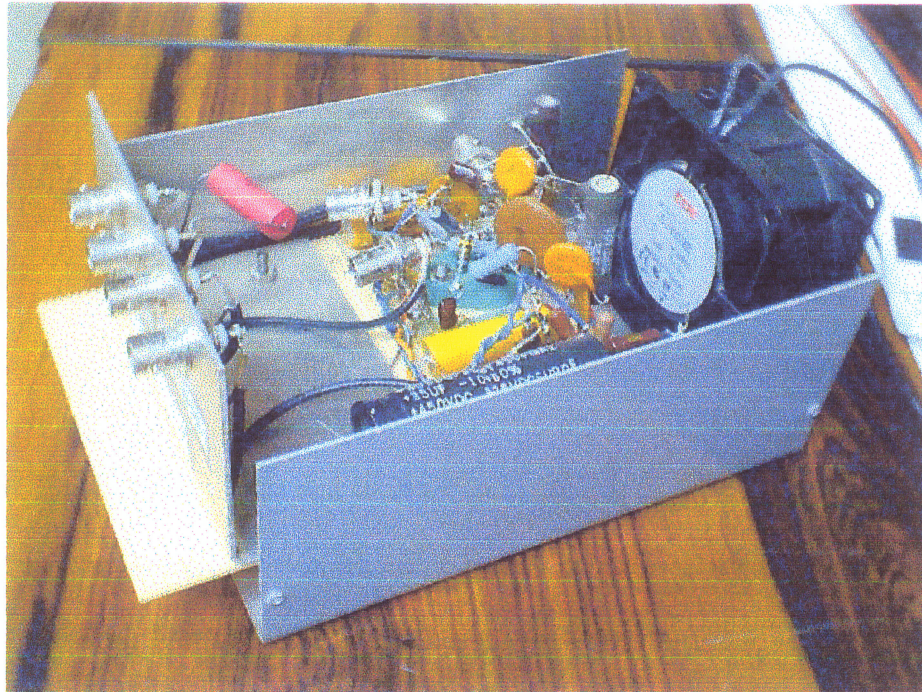
(A)
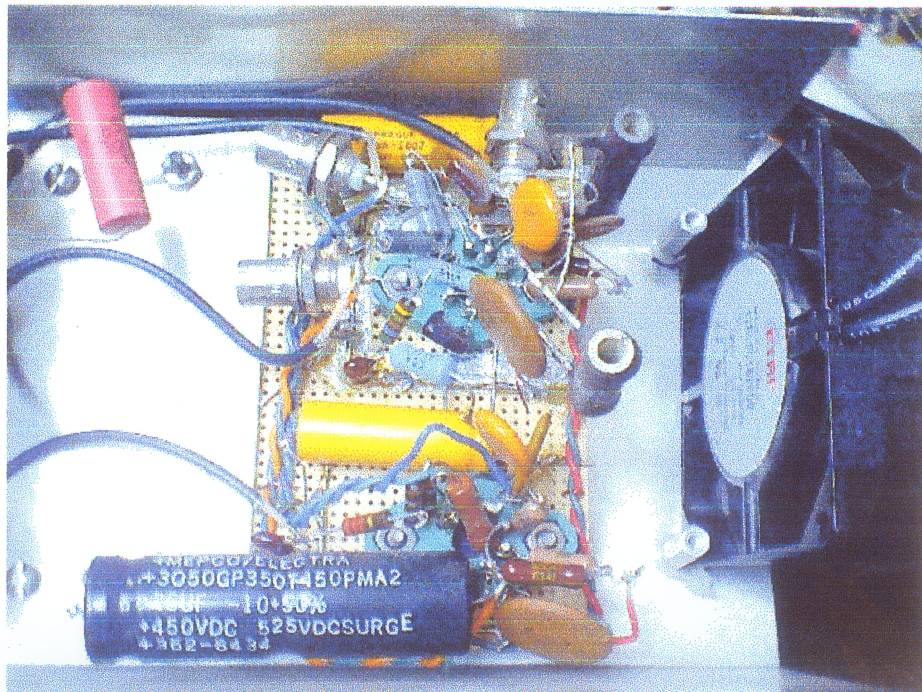
(B)

Fig. 6.14. Two views of the Fast Ramp Amplifier. (A) shows the complete system in its housing. (B) shows a close-up of the "inverted bug" construction.

SIMION Simulation for RFQ ejection with 20 ions

(A) No Energy Bunching Ramp applied, ΔE=14eV

(B) Energy Bunching Ramp applied, ΔE=7eV
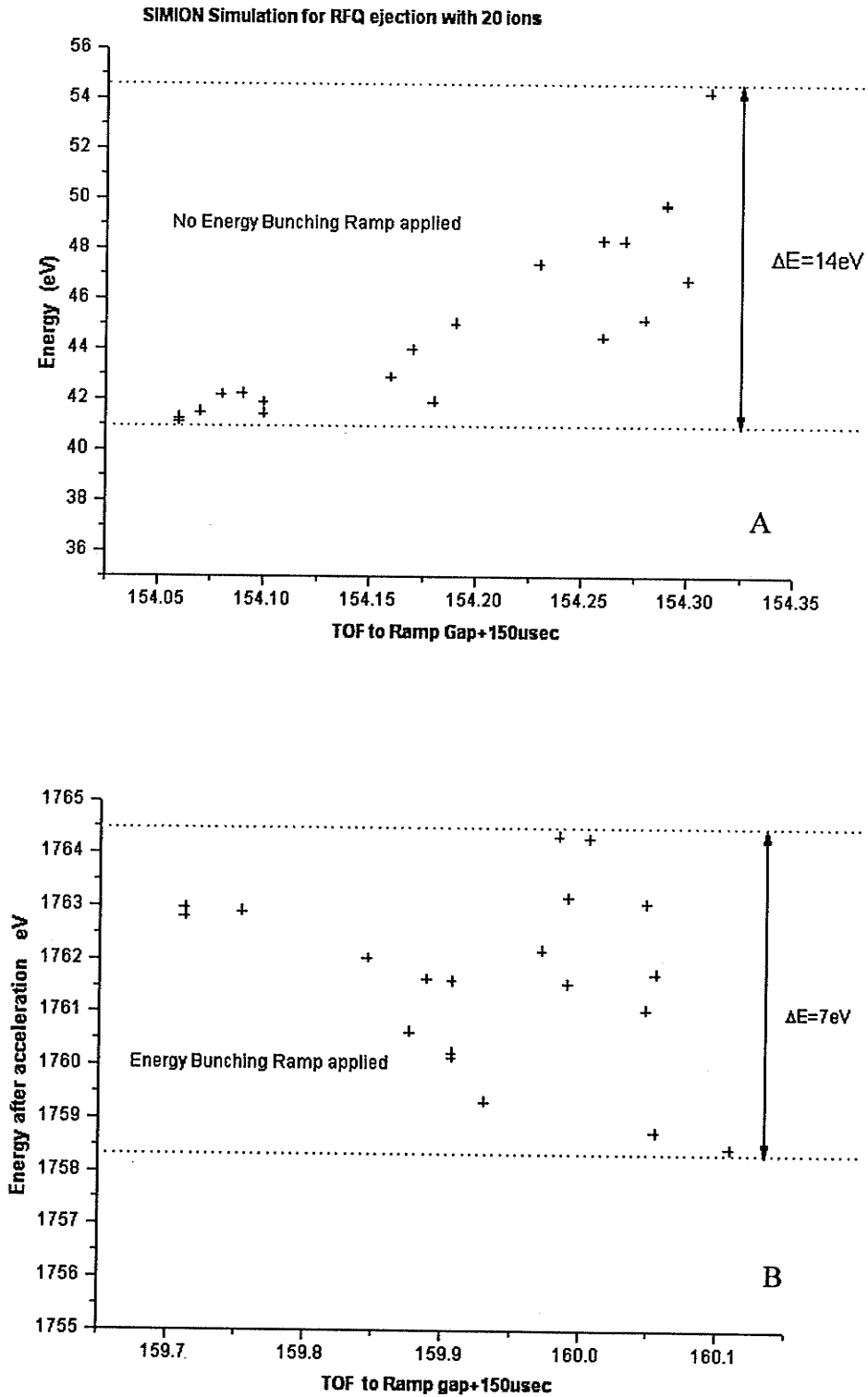
Fig. 6.15. Simulation results for ejection parameters: ϕ_{eject} = 0°, eject pulses = -100V, +70V . The intrinsic energy spread (A) and the energy bunching effect (B) is shown

Intrinsic Energy Spread -- No Ramp

ΔE=14eV

No of ions detected

Retarding Potential   Volts

A

Energy Spread with Ramp engaged

ΔE=8eV

No of ions detected

Retarding Potential   Volts
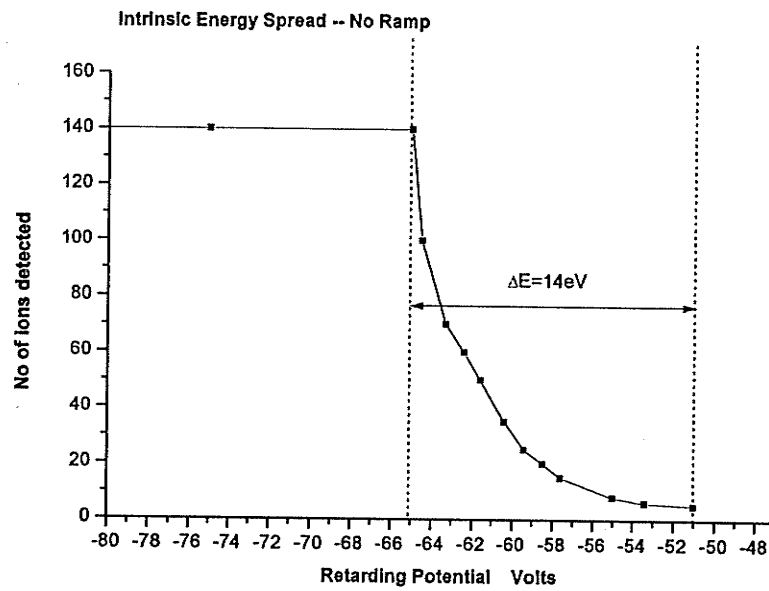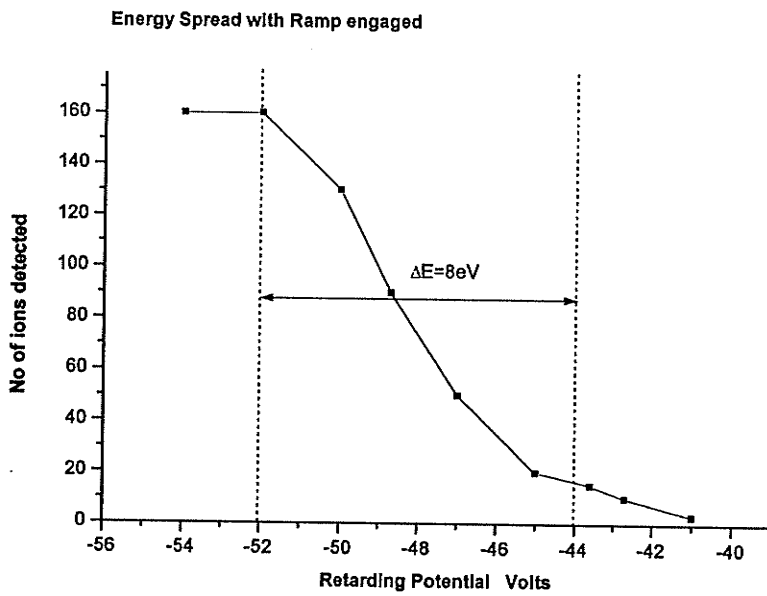
B

Fig. 6.16.   Measurement of the energy spread using the retarding potential technique for (A) no bunching ramp, (B) with the bunching ramp active

6.6. *Solid State Switching Systems.*

The design standard of the CPTMS is set to deliver mass measurements of exotic nuclei with half-lives greater than 50ms. The very short half-lives place stringent time constraints on the various experimental procedures that constitute the precision mass measurement process. Currently, mechanical relays dominate the low voltage switching systems that boast switching times in the order of a couple of milliseconds (3-4ms for a good relay). Clearly the excessive switching times for both "on" and "off" transitions, coupled with the number of switch operations per measurement cycle, would severely limit the overall capability of the spectrometer.

Solid state switching technology had reached maturity in the early 1990's. The availability of solid state analog switches as integrated circuits (IC) attest to the current widespread applications. The decision to implement solid state analog switches is rooted in the reliability of these switches coupled with the fast switching time. Mechanical relays are notorious for critical failure after a specified number of switch operations. "Misfiring" is also a cause for concern for aging relays. The switching event is also prone to "multiple bounce" before a stable state can be established. Solid state analog switches are far superior with switching transitions in the sub microsecond region, absence of transition "bounce" and virtually guaranteed lifetime performance. The only criterion where mechanical relays outperform solid state devices is in "off isolation". This is infinite for the classical switch compared to around 60dB for a solid state switch in the mid price range. A complete conversion to analog solid state switches for all low voltage switching devices is anticipated in the very near future.

The frequency selector was redesigned (Fig. 6.17), employing analog solid-state switches. Solid state switches from Precision Monolithics (now a subsidiary of Analog Devices) were selected to perform the switching. The choice was based on previous use in the Manitoba II High-Resolution Mass Spectrometer where these switches were used to deliver highly reproducible voltages in the microvolt level. The "off" isolation at -50dB (500kHz) of the SW06GP (Analog Devices SW06 Datasheet) was deemed suitable for the present use. Performance has been satisfactory with respect to high frequency waveform response. No distortion is present for RF at frequencies up to 3MHz. The intrinsic "switch" capacitance does not influence system capability at the frequencies of interest. Along with the systems test, a decision was made to use the SW06 in future solid state switcher designs. The requirement of a dual supply to facilitate control of bipolar signals is the only design complexity. This frequency selector is now 5 channel instead of the previously used 4 channel. This increase in available switching channels was prompted by the need to deliver a variety of signals to remove contaminants during online accelerator operation. The 5th channel will now enable a very small-amplitude contaminant removal excitation to be performed within 200Hz to the ω_+ of the isotope of interest.

The new improved Solid State Ring Waveform Delivery system (Fig 6.23) will also be based on SW06GP analog switches. The "off" isolation of almost -80dB at DC is adequate for this purpose. The SW06GP with 2 normally open and 2 normally closed switches provide for great design flexibility without the need for trigger inversion elements (section 6.8). The Solid State Waveform Delivery System is to be a prototype for a bank of switchers to be built at the ANL electronics shop. This system would provide for sub microsecond switching of precise analog voltages (differential 36V max.). A simple modification of the above-described circuit

can provide for triggered fast switching between two analog low voltage levels. A +/- 30V-driver amplifier presently provides low-voltage square pulses. These pulses have rise/fall times rated in microseconds, which makes the conversion to solid state analog switches possible. The only major concerns involve pulse amplitude and the ability to drive a capacitive load. Single supply operation is possible with the negative supply input tied to ground. This would allow control of signals with maximum amplitude +V-4V, which translates to 32V with a positive supply voltage of 36V. A more practical approach would be to allow for +/- 18V supplies so as to accommodate bipolar signals. Regulation of the readily available +/- 24V in the NIM crate to power this switching system would be a more economical alternative when compared to the currently used +/-30V drivers, which require dedicated AC line rectification/regulation with costly transformers.
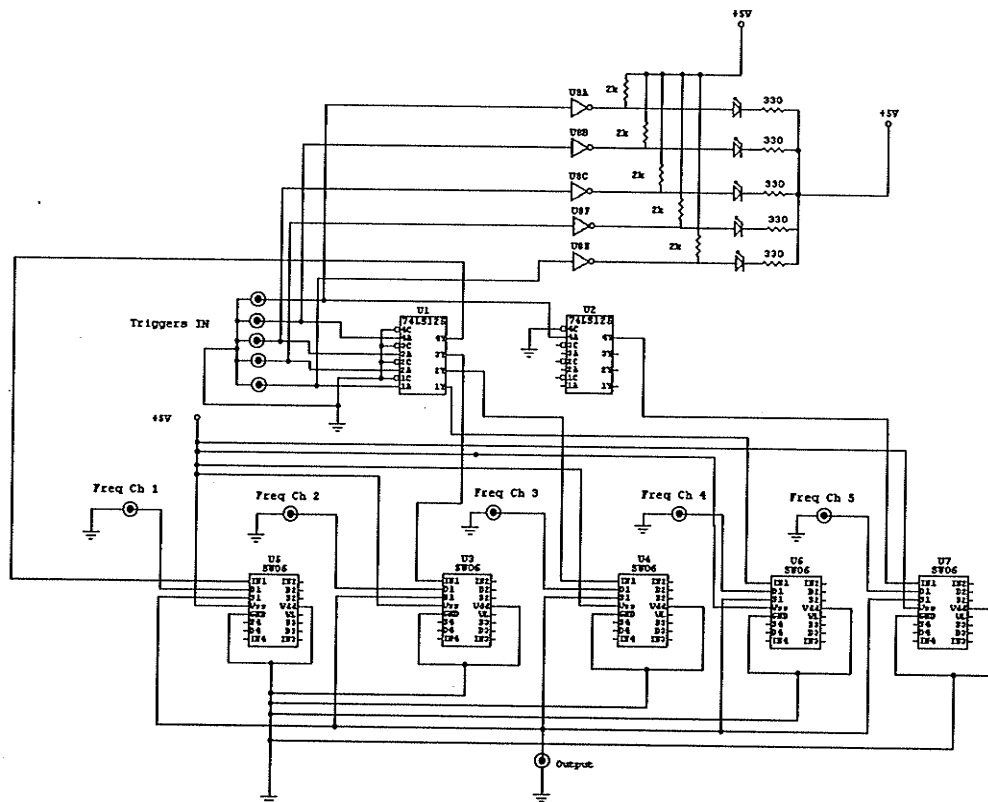
Fig. 6.17. CPT Solid State Frequency Selector

6.7. *Trapping Potential "Shallowing"*.

The potentials of the Penning trap ring and endcap electrodes fundamentally define the quadrupole trapping potential well. A variation of one or the other will alter the "well" depth and as such will affect the trapping efficiency. Incoming ions will only be trapped if their axial energy is less or at least equal to the well depth. This facet was discussed in a previous section (section 6.4). It is clear that trapping conditions will ultimately effect the possible precision of the mass measurement. High precision mass measurements (a few ppb) need to be conducted in a region of extreme magnetic field homogeneity. The entire ion cloud should execute orbital motions in this region. High homogeneity, high field magnets are difficult to construct. The high homogeneity is only rated over a small volume, hence the need to restrict the size of the ion cloud. Controlling the size of the ion cloud without any form of cooling is a desirable addition for the CPT system. The original system is configured to perform only limited "cloud contraction" by pulsing a correction tube electrode in an attempt to remove high energy ions. A better system was required.
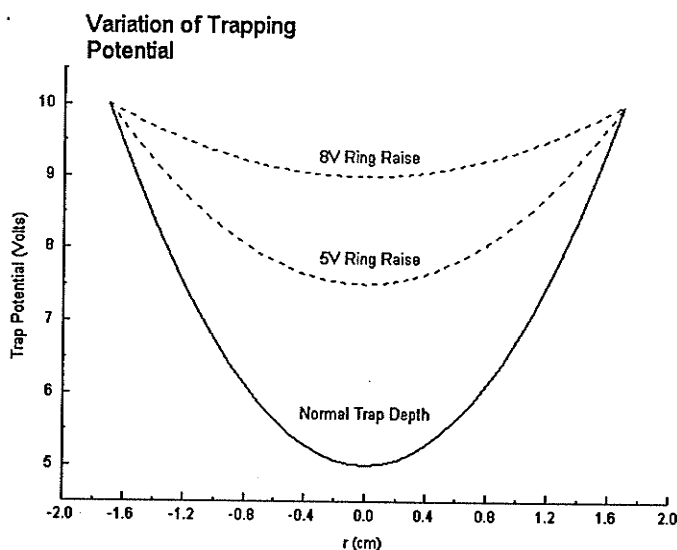
Fig.6.18. Potential Well "shallowing" during the ring raising process

The current operating state of the superconducting magnet has prompted considerable efforts in the development of a system that pre-selects only the ions situated in a very small region of acceptable magnetic field homogeneity. These ions are of very low axial energy (cold) and therefore reside near the bottom of the trapping potential. The harmonic potential implies that low energy ions oscillate over a region of smaller z dimension and are therefore under the influence of a much more homogenous magnetic field. The principle involved is to increase the ring electrode potential "adiabatically" so that the trapping potential is made shallow allowing high

energy ions to leave the trap confines. The trap potential is then returned to its normal depth (Fig. 6.18 and 6.21). The rate of increase must be very slow compared to the ion z-oscillation frequency.
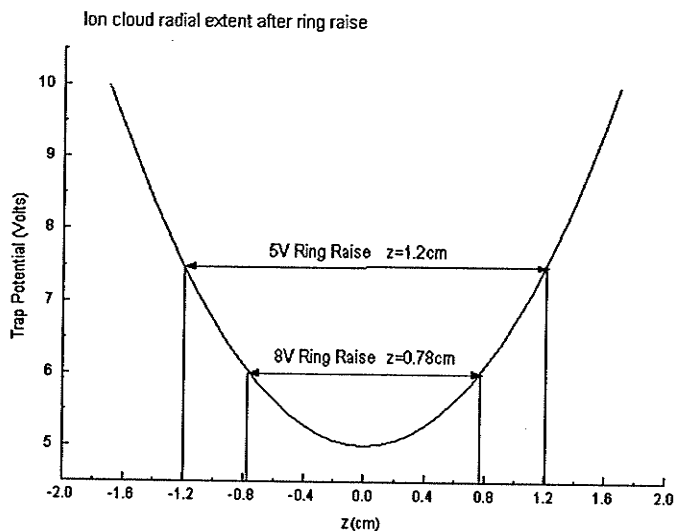
Fig. 6.19. Radial extent of the trapped ion cloud after ring raising.

A total rise time of 0.5ms is deemed sufficient for heavy ions (180-200amu). The top correction tube electrode is lowered simultaneously to allow for a well-defined escape path. The RF excitation, which constitutes the mass measurement process, is then applied to the remaining "cold" ions. A good indication to the working nature of this system is the resonance spectrum itself! The average TOF of the ions during off resonance scans is observed to increase. The trapped "cold" ions with low axial energy take a longer time to reach the detector. A comparison between resonance spectra with and without "potential shallowing" is shown in figure 6.20. The baseline shifts upward by 10% while the TOF depth increases by about 12%.

This "deep cleaning" process is bound to find application in most upcoming Penning trap systems in other research laboratories. The obvious pitfall relates to the effective trapped ion efficiency. An ion beam exhibiting poor energy bunching can still be "cleaned" but this will involve removing a large percentage of the incoming ions (90% or more). Widespread use of the procedure is not recommended for online exotic mass measurement where the production rates are very low. A moderately energy-bunched ion beam together with the deep cleaning process is predicted to be the avenue to attain 10ppb precision for both stable and exotic nuclei on the CPTMS with the current damaged magnet system. The circuit development together with relevant schematics is given in the following sections.
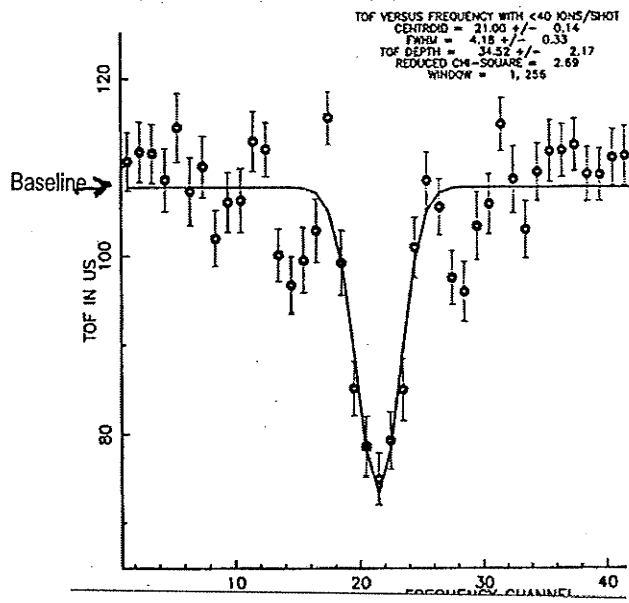
(A)
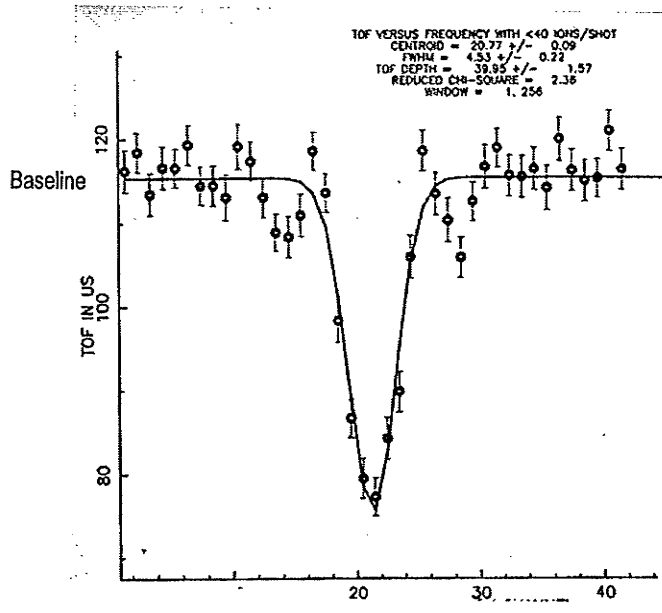
(B)

Fig. 6.20. Test spectra showing the effects of "ring raising". The TOF baseline of a resonance spectrum
attained with ring raising (B) compared to a normal spectrum (A). The higher baseline on the
former indicates a "cooler" ion cloud.
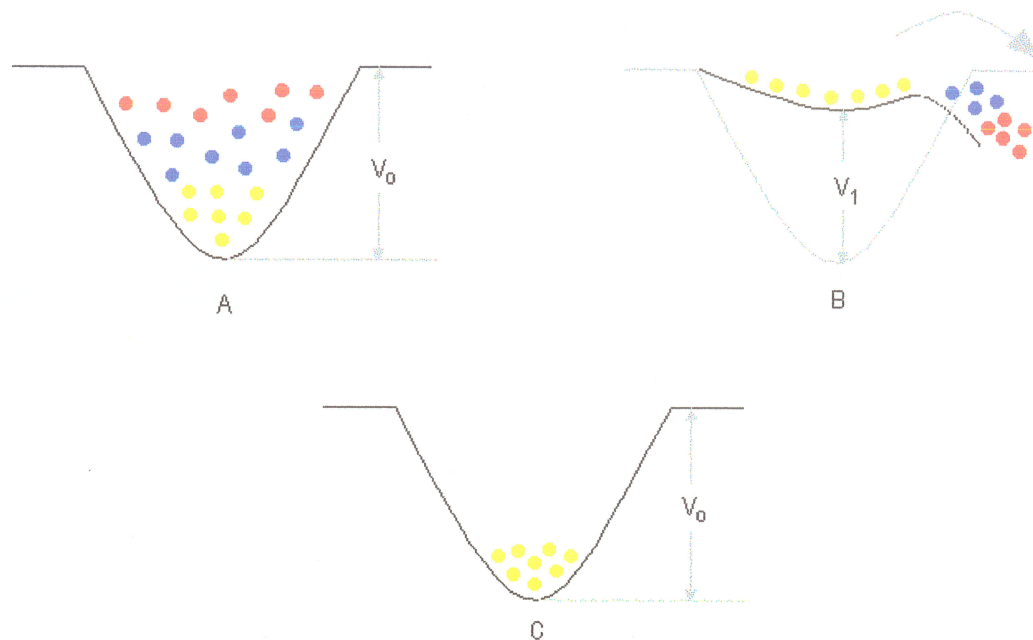
Fig. 6.21. A method to pre-select only low energy ions for mass measurement. Fig A shows ions with a wide energy spread being trapped. Fig B shows the trap depth being made shallow so as to "evaporate" the high-energy ions. The trap depth is then returned to its normal value (Fig C). The ions remaining are relatively cold and thus are confined near the trap center where the magnetic field is highly homogeneous. This relaxes the requirement for a well-tailored ion bunch, but at the expense of collection efficiency.

6.8. *Solid State Waveform Coupling System.*

The Penning Trap signal coupling system is a simple capacitive scheme. Arbitrary waveforms referenced to predetermined DC levels are placed on certain electrodes to enable specific processes to be executed. These can range from superimposing RF voltages on the ring electrode biased at a prescribed DC level to pulsing of the endcap electrodes during ion capture and ejection. The "shallowing" of the trapping potential could in fact be effected by a simple means of altering the ring electrode potential. The motivation behind the process has been elaborated elsewhere while this section highlights design and construction detail.

The original design conceived in January 2001 was a simple mechanical relay based system (Fig. 6.22). The relays were adopted in order to decouple the waveform feed from the ring electrode when the process was completed. This is to prevent any adverse loading effects that might occur during the application of very low level RF signals to the ring electrode. The schematic shows the arbitrary waveform independently coupled to each of the four ring quadrants. This system was tested and effectively incorporated into the CPT apparatus. A decision to

move away from mechanical relay based devices was made and as such the design was re-evaluated. The current design consists entirely of solid state analog switches, the Analog Devices SW06. The arbitrary waveform in this design is applied to all four ring quadrants through the primary Ring DC level feed. This eliminates the possibility of any variation in applied signal to the four quadrants. The switching system in the complete configuration consists of two sections, the Waveform Coupler and the Load Decoupler (Fig. 6.23). The Waveform Coupler is a simple system of three switches (Fig. 6.24). During the triggered application period, the arbitrary waveform is biased to the primary Ring DC level. This signal is then transferred to all quadrants via the DC feed line. The end of the trigger sequence completely decouples the arbitrary signal drive and sets the condition DC in = DC out, through the switch S1. This is the configuration adopted during all the RF excitation processes. It should be instructive to note that the circuit once again maintains a non-intrusive presence during the actual precision mass measurement process.

Initial tests indicated a severe loading effect due to the RF coupling capacitors constituting a load terminated by the RF driver system. A simple solution was to disengage the load, as there was no apparent need for RF signals during the deep cleaning period. The Load Decoupler is basically a four-channel analog switch, which disconnects the RF drivers when a trigger is received. The complete switching configuration is shown in Fig. 6.24, both with the pre-existing system in black and the new additions in red. The switch positions on the Waveform Coupler and the Load Decoupler are shown as during a HIGH trigger (arbitrary waveform application).
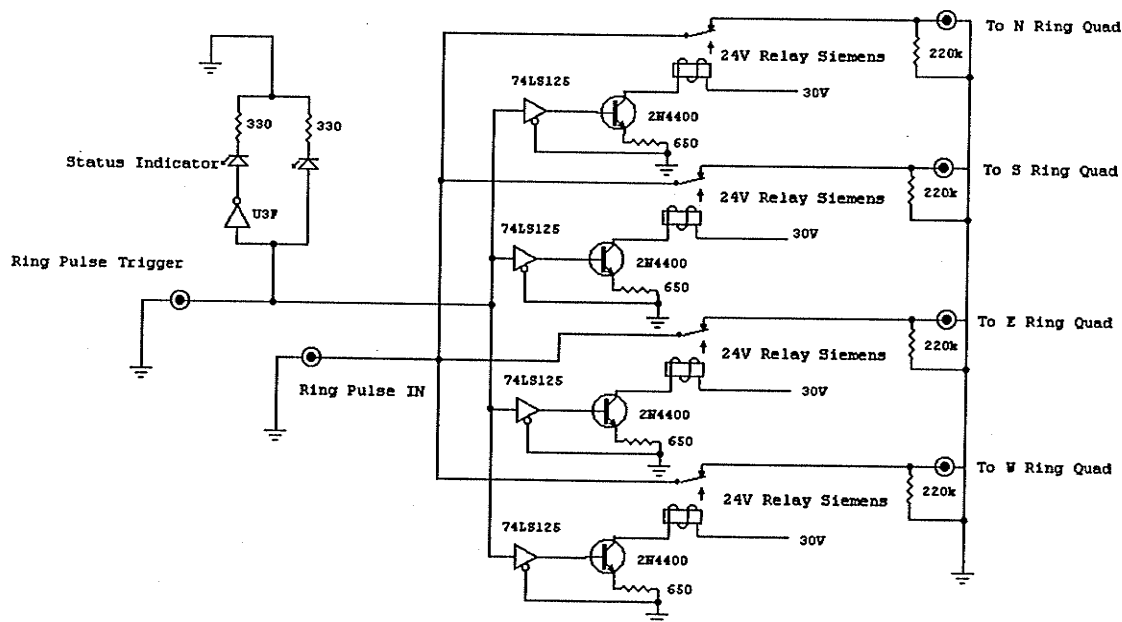
Fig. 6.22. CPT Ring Waveform Relay System
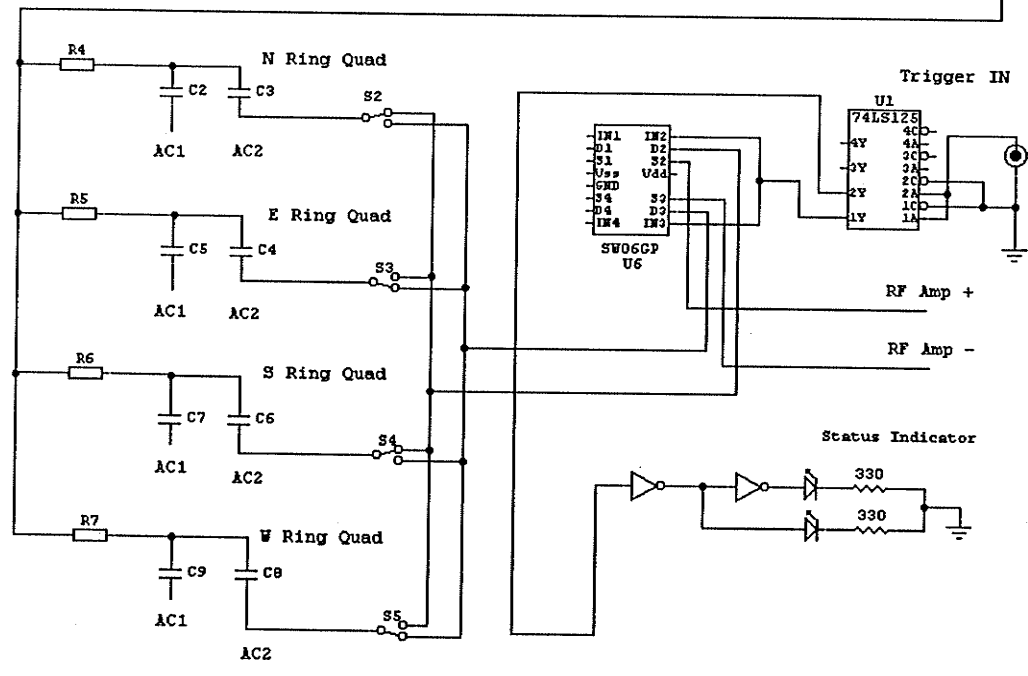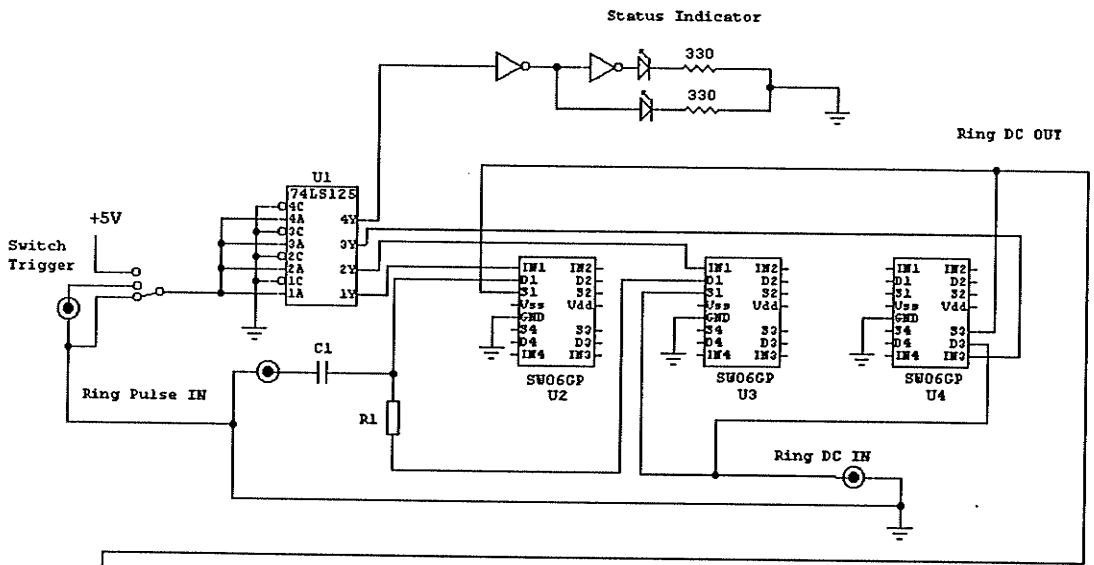
Fig. 6.23. CPT Arbitrary Ring Waveform Coupling System
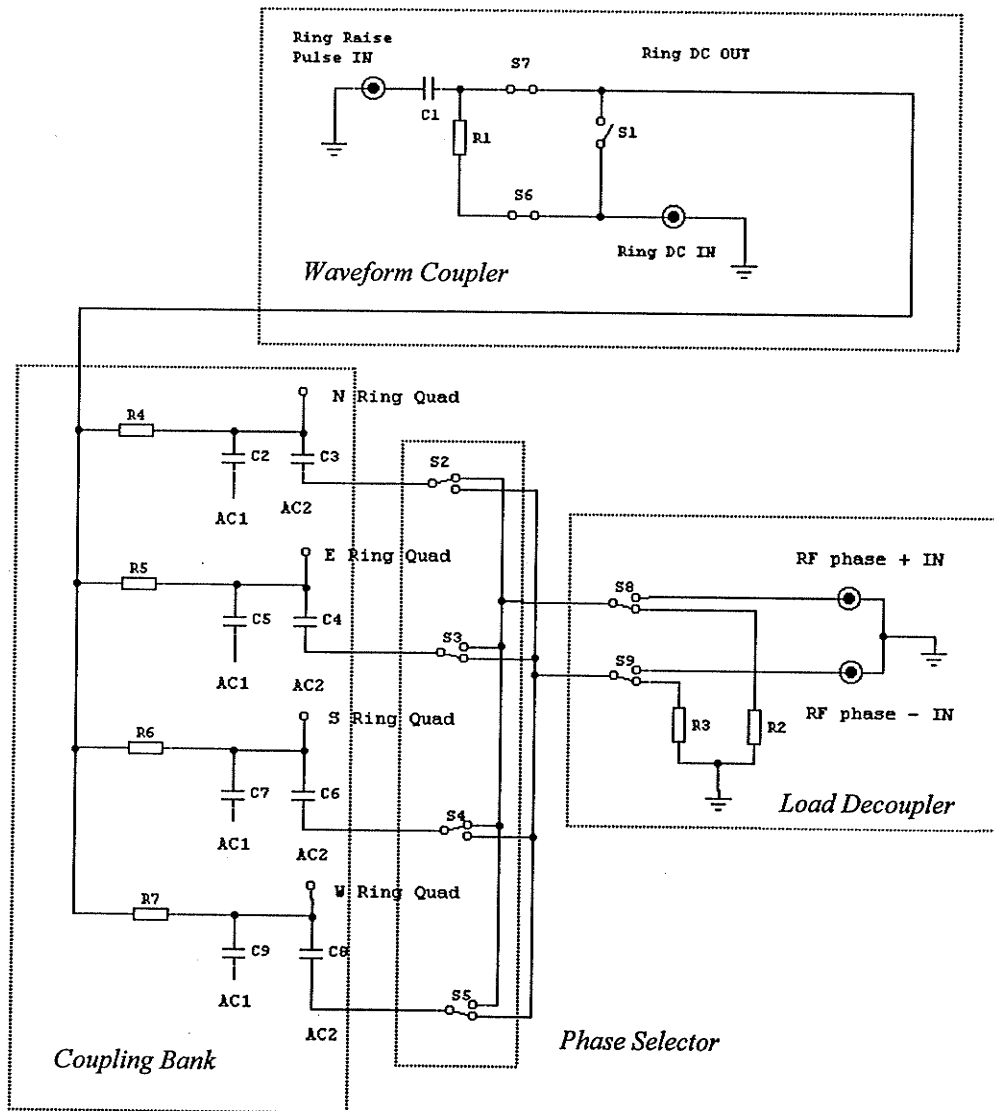
Fig. 6.24. Arbitrary Waveform Application Switch Configuration
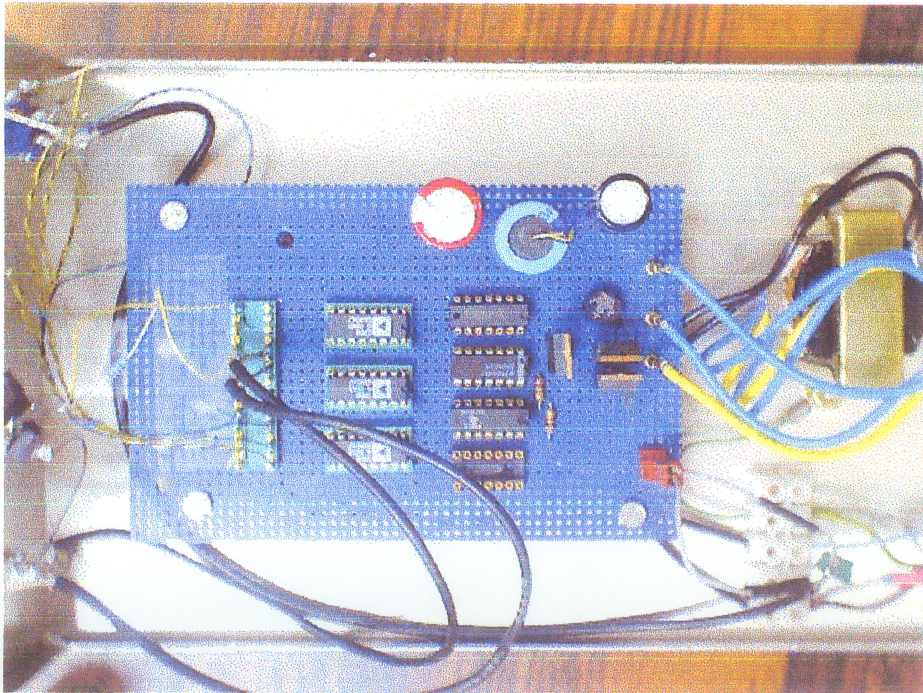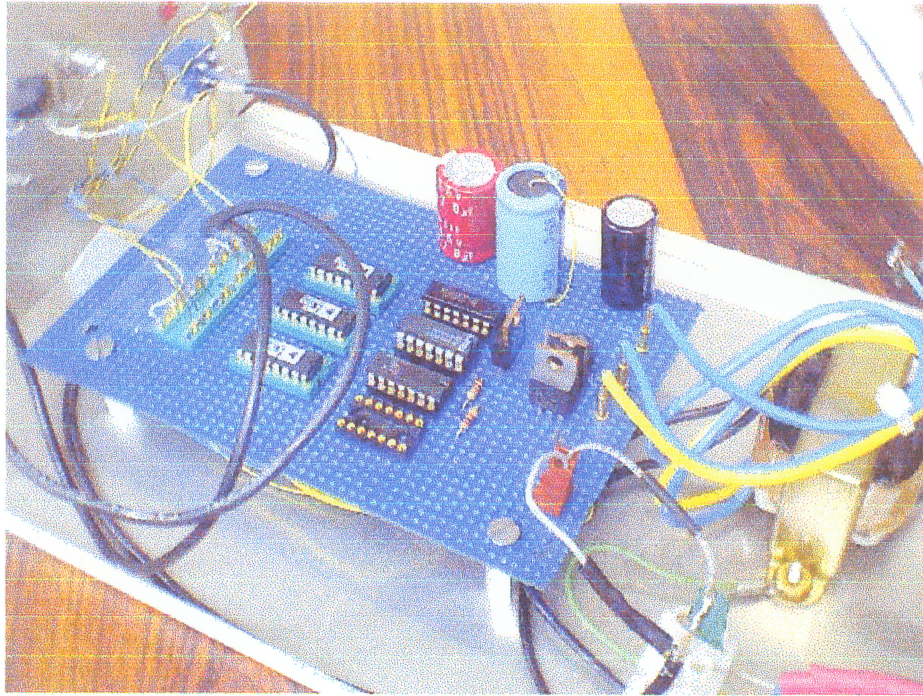
Fig. 6.25.   Two views of the Arbitrary Ring Waveform System. Load Decoupler is in a separate chassis, not shown.

Chapter 6 References

- Analog Devices. *SW06 Quad JFET Switch Datasheet*.

- Andreycak, B. *Unitrode Application Note U137 "Practical Considerations in High Performance MOSFET, IGBT and MCT Gate Drive Circuits"*.

- Apex Microtechnology. (1999). *Apex Power Intergrated Circuits-Application Note 8*.

- Dahl, D. A. (1995). *SIMION 3D User's Manual, Idaho National Engineering Laboratory*, Idaho Falls.

- Fulford, J. E. and March, R. E. (1979). *International Journal of Mass Spectrometry and Ion Physics*, **30**, 373-378.

- Gottlieb, I. M. (1993). *Practical RF Power Design Techniques*, Chap 3, pg. 90. TAB Books.

- Humphries, Jr. S. (1986). *Principle of Charged Particle Acceleration*, pg. 426-430. John Wiley and Sons.

- International Rectifier Technical Information, IR Application Note AN-940.

- Jones, R. M., Gerlich, D. and Anderson, S. L. (1997). *Review of Scientific Instruments*, **68**, 3357-62.

- Mosburg Jr., E. R., Vedel, M., Zerega, Y., Vedel, F. and Andre', J. (1987). *International Journal of Mass Spectrometry and Ion Physics*, **77**, 1-12.

- Richards, J. A., Huey, R. M. and Miller, J. (1973). *International Journal of Mass Spectrometry and Ion Physics*, **12**, 317-339.

- Rocher, J., Vedel, M. and Vedel, F. (1998). *International Journal of Mass Spectrometry and Ion Physics*, **181**, 173-180.

- Simpson, R. E. (1987). *Introductory Electronics for Scientists and Engineers* (2nd Edition), pg. 280-284. Prentice-Hall.

7. Mass Measurement

The operation of the CPT Mass Spectrometer can be subdivided into two sections. The first section concerns transfer of ions from "ion source" to RFQ buncher trap. The second section involves ion transfer from RFQ trap to Penning Trap and the mass measurement process itself. As presented earlier, the ion source in question can be the laser/target plate or the remote Gas Cell/Cooler system. The experimental setup is such that the Penning Trap is impervious to ion source "nature" once the ions are sufficiently cooled in the RFQ trap. The mass measurement process only involves the precision Penning Trap. All other prior processes merely involve ion transfer and beam characteristic tailoring (e.g. energy bunching). The energy bunched ion pulse captured in the Penning trap is described in Chapter 4. The mass measurement process consists of a series of operations as indicated in the figure below. These distinct operations are critical in "preparing" the trapped ion cloud for the precision mass measurement process.
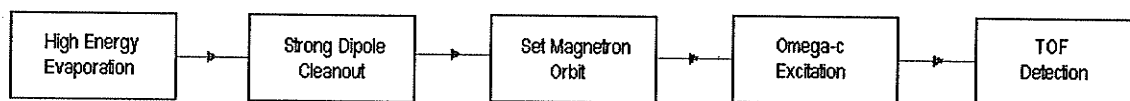
Fig. 7.1. Block diagram of the mass measurement process

7.1. *Process*

Tuning the Penning Trap

Prior to any Penning Trap process, it is crucial to establish a potential distribution within the trap confines that closely resembles a quadrupole potential. The presence of correction electrodes biased at specific DC values is used to account for the "distortion" produced by the practical trap design (see Chapter 4). The ring and endcap electrode potential determine the trapping well depth. The SIMION program is then used to compute the DC values for the various correction electrodes to attain the required quadrupole potential. These values are used as the "starting" values for a pure quadrupole potential. Slight adjustments to these DC values are normally performed through observing the ω_+ TOF spectra for symmetry and maximum TOF depth. This is due to the fact that the dipole motion is more sensitive to changes in the electric field. The tuning needs to be done only once as long as the trap is not dismantled. A millivolt stable DC supply is usually adequate to ensure long-term stability of the various electrode DC bias.

High Energy Evaporation

Ions captured with above average axial energies will exhibit orbital motion far above the trap center. They are therefore under the influence of a more inhomogeneous magnetic field extent. In order to prevent this undesirable situation, a method is devised to remove or clean the trapped ion cloud of highly energetic ions. The original evaporation system merely consisted of pulsing the top correction tube down to allow the

high-energy ions to leave the trap. This method is further improved by simultaneously shallowing the trapping potential. This constitutes a "deep clean" process whereby the user is provided with the option of totally emptying the trap except for the "cold" ions orbiting very close to the trap center. The result is a contracted ion cloud orbiting in a region of superior magnetic field homogeneity (see Chapter 6.6).

Strong Dipole Isotope Cleanout

The capture process is not mass selective to the required resolution. It is common for an ion bunch captured in the Penning Trap to contain 3-5 different species of ions. The energy spread of the incoming ions, the short drift tube section and the capture time period prevent the capture of just the isotope under experiment. This is further complicated by the presence of contaminant isobars during online operation. The removal of all species except that under experiment is crucial to attain good resonance spectra. "Surgically" exciting the modified cyclotron motions (ω_+) is a means to remove unwanted ions. Mass selection using this method is good to a resolution of about 1×10^{-6}. The process is relatively straightforward. The orbital motions of the unwanted ions are excited resonantly. Enough RF power is pumped into the motion such that the orbits increase and the unwanted ions inevitably collide with the electrodes.
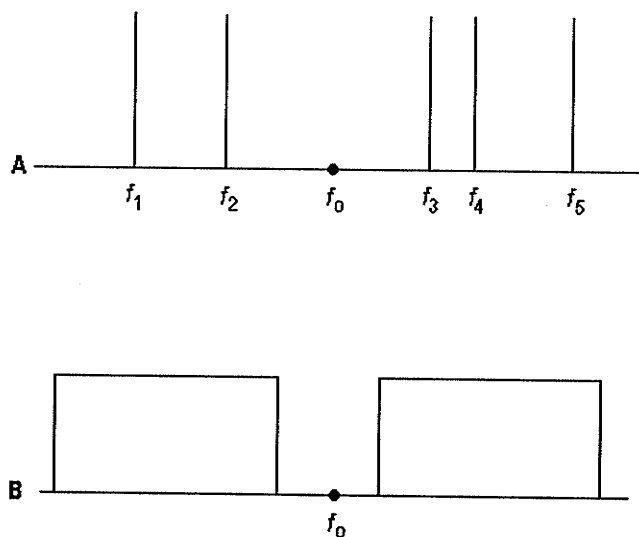
Fig. 7.2. Two modes of strong dipole excitation employed

Two methods are currently being used to resonantly excite dipole motion. Discrete excitation is where certain frequencies are excited sequentially. A frequency sweep can also be performed whereby a frequency range is scanned except for a "notch" or "window" strategically placed over the ω_+ frequency of the species under experiment.

Magnetron Orbit

The magnetron orbit is set by resonantly exciting the ω_- motion to a well-defined orbit. This is done carefully by adjusting the RF amplitude so that none of the ions are excited to an orbit large enough that they collide with the trap electrodes. Currently only a very small RF amplitude is used so as to ensure a small magnetron orbit. The ions in this case orbit a region where electric and magnetic field imperfections are minimized.

Resonance Excitation

The final phase in the RF excitation sequence is the quadrupole ω_c excitation. The excitation amplitude is carefully chosen so that the complete "conversion" from magnetron motion to cyclotron motion can be achieved during the time in question. This can be achieved by observing the TOF spectrum for the characteristic "double hump" (Fig. 4.5) that signals the applied RF field as being <u>twice</u> that required for complete conversion. The amplitude is subsequently adjusted for complete conversion. This process is normally done for 200ms excitation and is then scaled for longer excitation times (see eqn. 4.47a). The excitation times can range from 50ms to 2 seconds depending on the required experimental precision. The ions are subsequently ejected from the Penning trap.

TOF Detection

The ions are ejected towards a MCP detector and the arrival times are measured. The ion arrival times are "binned" by the MCS (Multi-Channel Scaler). The 256 channels are set to advance at a 4µs interval, per channel. The average arrival time for the ion bunch is then computed and stored as a data point. The entire process above is repeated for a new ion bunch with the only difference being the quadrupole excitation frequency. About forty different frequency scans are performed resulting in 40 data points giving the TOF versus RF excitation frequency information. The cyclotron resonance frequency is thus seen as the frequency that gives the greatest TOF dip (ions arriving at the detector the fastest). This method is very well suited for ions with low production rates. System tests with stable Pt ions have proven the possibility of making single measurements to < 10keV precision in about 2 hours, with ion production rates as low as 4 ions/second (Chapter 8)!

7.2. Systematic Effects

As in any experimental setup, it is common to expect certain systematic effects due to the less than ideal experimental conditions. These effects are constant, in that, the influence on the experiment can be predicted if the cause is known and understood. Appropriate corrective methods can then be incorporated into the experimental process to minimize or "calibrate away" these effects. In this section an overview of the systematic effects together with the corrective procedures will be examined.

Electrical Field Imperfections

The quadrupole trapping potential $V(z)$ can be written as a sum of Legendre polynomials (m=0 only) from azimuthal symmetry considerations,

$$V(z) = \frac{V_o}{2}\left(C_o + \frac{C_2}{z_o^2}z^2 + \frac{C_4}{z_o^4}z^4 + ..\frac{C_{2n}}{z_o^{2n}}z^{2n}\right). \tag{7.1}$$

C_{2n} represents the contribution of the various multipole orders to the potential such that,

$$\sum_{n>0}^{\infty} C_{2n} = 1. \tag{7.2}$$

The reader is advised to note that the above sum does not contain the C_o term. This is due to the nature of the "zeroth order multipole" which is in fact z independent. In simple terms, it is just a DC offset and therefore does not distort the quadrupole potential in any way. For a true quadrupole potential it then follows that $C_2 = 1$ and $C_{2n\neq2,n>0} = 0$. In reality, small components of higher order multipoles are present due to electrode machining or deliberate modification to the ideal trap geometry (e.g. exit holes and slits in ring electrode). The first two higher order multipoles and their effect on the all important sum frequency is given as,

$$\Delta(\omega_+ + \omega_-)_{c_4} = \frac{3}{4}\frac{C_4}{z_o^2}\frac{\omega_z^2}{(\omega_+ + \omega_-)}\left(\rho_+^2 - \rho_-^2\right),$$

$$\Delta(\omega_+ + \omega_-)_{c_6} = \frac{15}{8}\frac{C_6}{z_o^4}\frac{\omega_z^2}{(\omega_+ + \omega_-)}\left[3z^2\left(\rho_-^2 - \rho_+^2\right) + \left(\rho_+^4 - \rho_-^4\right)\right]. \tag{7.3}$$

The octupole (C_4) and dodecapole (C_6) components introduce frequency shifts dependent on the ion orbit radii. The dodecapole component is also proportional to the extent of z-motion. Besides the installation of correction electrodes in an attempt to null the presence of C_4 and C_6 components, certain precautions need to be incorporated to ensure minimum frequency shifts in the case of "less than perfect" corrective techniques. These precautionary measures are quite clear, firstly, keep ion orbit radii small and secondly, ensure that ions are trapped near the bottom of the trapping potential where z oscillation is at a minimum. Setting up a small magnetron orbit in addition to the highly efficient "deep-cleaning" method described in this work (see Chapter 6.7), prevents any gross frequency shifts from occurring.

Misalignment of trap to magnetic field axis

The trap axis is ideally aligned to the magnetic field axis. Generally the alignment is performed on the bore with an electron beam/detector set up. The trap is then inserted into the bore as a snug fit. Frequent removal of the Penning trap from its housing might cause the bore to shift slightly from alignment. The

misalignment produces a linear dependence of the cyclotron frequency on the ion mass. This prompts the use of a calibration or reference mass with about 3amu mass difference from the experimental mass. The other method is to fully characterize the mass dependence over a large mass range by using organic or carbon cluster ions. The correction can then be applied to the mass under experiment. This characterization must be done whenever the trap is removed from the bore and reinserted so as to track any possible shift in the alignment.

Trapped Ion Number

It has been observed that varying the number of ions stored in the trap causes shifts in the cyclotron resonance frequency. This might be due to the fact that large ion clouds will occupy a larger extent of the trapping volume thereby being subject to electric/magnetic field imperfections. The Coulomb interaction of similar ion species is not expected to give rise to any frequency shift but a shift is expected if the stored ions are of different masses. It is therefore imperative to clean the trap of all but one ion species. Operation with low number of ions is best to avoid the pitfalls of an expanded ion cloud. Comparison of the reference and experimental masses must then be performed under similar ion number conditions. A single trapped ion in each case offers the ultimate unprejudiced measurement!

8. Experimental Results

This work involves precision stable mass measurements in the A~200 region. This region has long-standing conflicts; case of this is the "Hg problem" (Wapstra 1985). Absolute Mercury (Hg) mass measurements performed by the University of Manitoba's AMD Group have consistently been deemed 20keV "more stable". These measurements were conducted with the Manitoba II High Resolution Mass Spectrometer twice, 20 years apart, yielding very similar results. The Atomic Mass Evaluation (AME) uses a complex system of determining masses through a massive data compilation. A multitude of data involving mass measurements and reaction Q values are assembled and from this self-consistent mass values are attained. It is possible to find that errors in Q value measurements "accumulate", and are propagated to the final mass tabulation. It is therefore imperative to obtain anchor points along the stability line in the form of absolute mass measurements. The Platinum (Pt) measurements performed on the CPT MS are expected to provide some "relief" in this beleaguered region of precision mass measurements.

The role of the CPT MS will largely involve precision mass measurements of nuclei far from stability. The precision required of these measurements could range anywhere between 1-100 keV, depending on the experimental aims. Developments in this work will help characterize the spectrometer system as well as introduce and test novel techniques that will prove valuable during the push towards the high end of "online" precision. It can be noted that the CPT MS design does not differentiate between "ion sources". System performance is expected to be similar whether ions are laser desorbed from a solid target or exotic species created online. The following considerations were deemed paramount in the pursuit of high precision mass measurements employing Penning traps and the author restates this in the list below.

Clean beam

Requires that ions of only one species remain in the trap during the mass measurement process. All other ions present due to the injection process must be removed. These can range from isotopes to organic contaminants.

Energy bunching

Ions injected into the Penning trap must have a narrow energy spread. This prevents the trapped ion cloud from occupying a large extent of the field region.

User defined high energy evaporation

Removing ions with high axial energies that would otherwise probe a larger, more imperfect magnetic/electric field region. User is now given the option to remove almost 99% of the trapped ions!

Low number of ions

Mass measurements with a very small ion number ensure that the ion cloud can be confined in a small region of superior field (electric/magnetic) homogeneity. Operation close to the "single ion"

limit also provides a test platform to predict system performance during the event of very low ion production rates, a trait of exotic nuclei with small production cross sections.

The data presented here is a result of extensive modification to system electronics and processes. Direct cyclotron resonance frequency measurements were performed for the four most abundant isotopes of Platinum. The abundances (WebElements 2002) are as listed in Table 8.1 below

Table 8.1. Platinum Abundance

Platinum Isotopes	Abundance (%)
190	0.01
192	0.79
194	32.9
195	33.8
196	25.3
198	7.2

The reference mass selected was Au (A=197) for convenience. Switching between reference and experimental masses now just becomes a simple task of moving the respective target plate into place. The number of trapped ions in each case was kept to a maximum of 39 ions. Any wild fluctuations were accounted for by the analysis program, which counts ions and "bins" accordingly. All measurements were performed with the "deep cleaning" method thereby using only "cold" ions.

8.1. Data Analysis

Raw data is primarily the ion arrival time. The MCS is set to store these times in discrete bins of 4μs time-width (256 x 4 = 1024μs). The average TOF for the arriving ion bunch is then computed from number of ions in each bin and the bin "time". This constitutes the data point for a particular excitation frequency. This cycle is repeated about 40 times at 40 different frequencies to yield data points for a scan. The user then selects the number of scans required to achieve sufficient statistics. The individual scan data is stored in a "cumulative" manner as "new" scan data is just added on then "re-averaged". In real time, the resonance spectra slowly starts to take shape as individual data points become more defined. A typical spectrum is shown in Chapter 4.

The fitting function used initially was a simple inverted Gaussian line shape. The main peak was the only region of concern. This simple function was then replaced by a more accurate description of the experimental spectrum, mathematically equivalent to the energy gain equation (4.48). Fig 8.1a and 8.1b shows a typical dataset being fitted with both the simple Gaussian function and the more complex "Sinc Squared" function. The "Sinc" function besides being an accurate description of the experimental line shape also provides the user with instantaneous feedback of the quality of the electric

fields within the trap. Excessive side band amplitude will signal cyclotron-magnetron over conversion and the RF amplitude must be adjusted while asymmetry indicates a far from ideal static quadrupole electric field which can be corrected by varying the correction electrodes DC potentials.
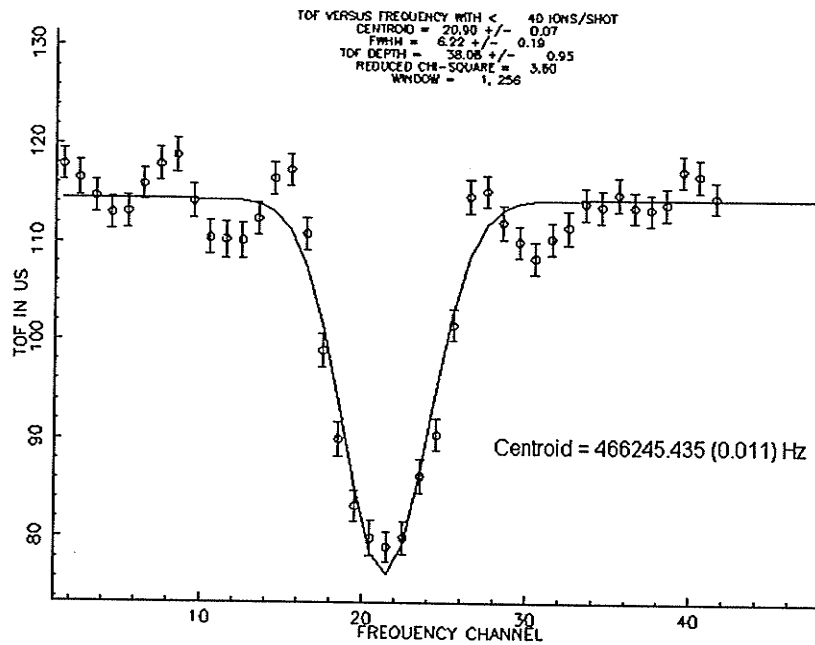
Fig. 8.1a A simple inverted Gaussian fit for the cyclotron resonance spectrum of [194]Pt
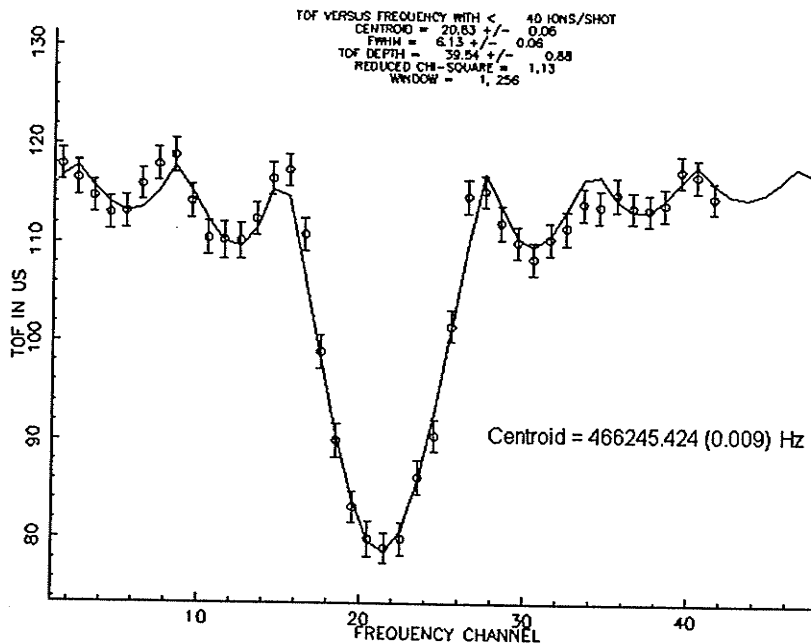
Fig. 8.1b The "Sinc" fit to the above dataset.

The fitting function provides the centroid position and accompanying error for the TOF peak,

$$Centroid = f_c \pm \delta_{f_c} . \qquad (8.1)$$

The frequency information is then converted to atomic masses with the frequency ratio R, (4.53) with the frequency errors (expt. and ref.) added in quadrature,

$$\frac{\sigma_m}{M} = \frac{\sqrt{\dfrac{\delta^2_{f_c\,expt}}{f_c^2} + \dfrac{\delta^2_{f_c ref}}{f_{ref}^2}}}{R} . \qquad (8.2)$$

The measured atomic mass is hence given,

$$M \pm \sigma_m . \qquad (8.3)$$

This result constitutes a measurement run. This is then repeated according to the number of runs (N) made for a particular mass species. The final mass value is attained by a straight average of all the runs for a particular isotope and the accompanying error δ_{mean}.

$$\overline{M} = \frac{\sum\limits_{i=1}^{N} M_i}{N} .$$

$$\delta^2_{mean} = \frac{\sigma^2}{\sqrt{N(N-1)}} . \qquad (8.4a)$$

The weighted mean can also be computed for a particular dataset in the case of measurements performed with varying precision. This is most likely useful when measurements of a particular isotope are made with different excitation times resulting in different precision. The weighted mean (M_w) is stated as:

$$\overline{M}_w = \frac{\sum\limits_{i=1}^{N} \left(\dfrac{M_i}{\sigma_i^2} \right)}{\sum\limits_{j=1}^{N} \left(\dfrac{1}{\sigma_j^2} \right)} . \qquad (8.4b)$$

The associated errors are computed as, standard deviation σ_{ext}, which is a measure of "scatter" of all data points,

$$\sigma_{ext} = \sqrt{\frac{\sum\limits_{j=1}^{N}\dfrac{\left(M_j - \overline{M}_W\right)}{\sigma_j^2}}{(N-1)\sum\limits_{i=1}^{N}\dfrac{1}{\sigma_i^2}}}\;, \qquad\qquad (8.5)$$

and σ_{int}, an implicit indicator of "reproducibility".

$$\sigma_{int} = \frac{1}{\sqrt{\sum\limits_{i}^{N}\dfrac{1}{\sigma_j^2}}}\;. \qquad\qquad (8.6)$$

A measure of data quality is the Birge ratio, $R_B = \sigma_{ext}/\sigma_{int}$. A value much greater than one would indicate the presence of inconsistent data points. The external/internal errors will only be quoted in the final result. All other errors quoted are standard errors as defined by eqn. 8.4a.

8.2. Data Consistency

The results mentioned here were acquired over a two-week period with machine operation close to 16 hrs a day. Excitation time is either 1 or 1.5 seconds. Forty frequency steps are taken to constitute a measurement "scan" and ten measurement scans make a measurement group. It is common to acquire 15 groups for sufficient statistics, especially in the case of really low ion numbers. The effective "measurement" time per isotope, say for 1-second excitation is,

$$40\times1\times10\times15 = 6000s\left(\approx 1.5hr\right).$$

This does not include the time taken for other processes (*e.g.* high energy evaporation and isotope cleaning). The total time can come close to 2 hrs per isotope. During most run days, two reference measurement sets are taken, interspersed between that of the Pt isotopes. This serves to track any changes in the magnetic field. Graphs for 2 Pt isotopes and ^{197}Au calibration have been included to check possible night/day fluctuations due to changes in ambient room temperature (fig. 8.2). The temperature changes can affect the magnetic field in a cyclical manner. Figure 8.3 shows the measured cyclotron resonance frequency over a period of two weeks. In order to illustrate all four isotopes on the same axis, the deviation from the mean is computed for each of the isotopes, which is then illustrated.
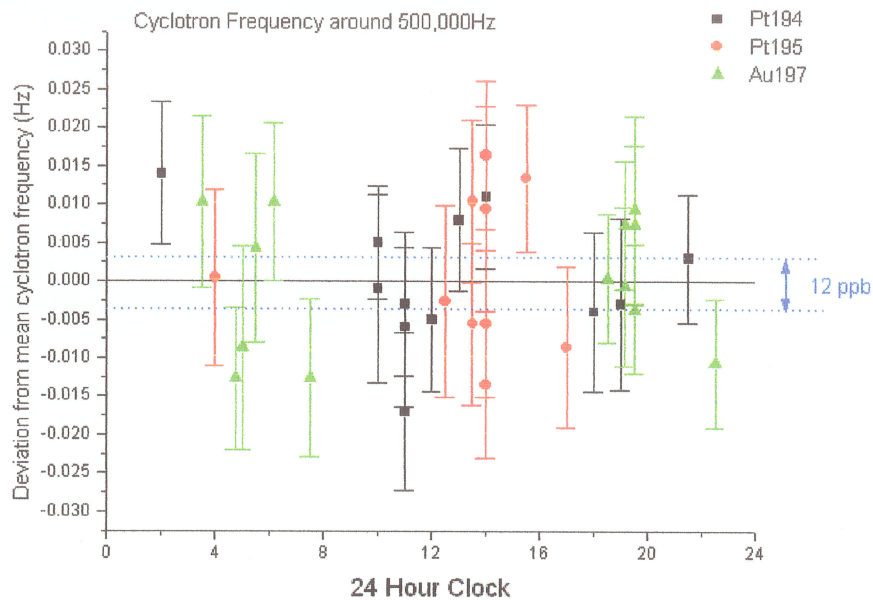
Fig. 8.2. Measured cyclotron frequencies. The time of measurement is indicated (24hr clock).
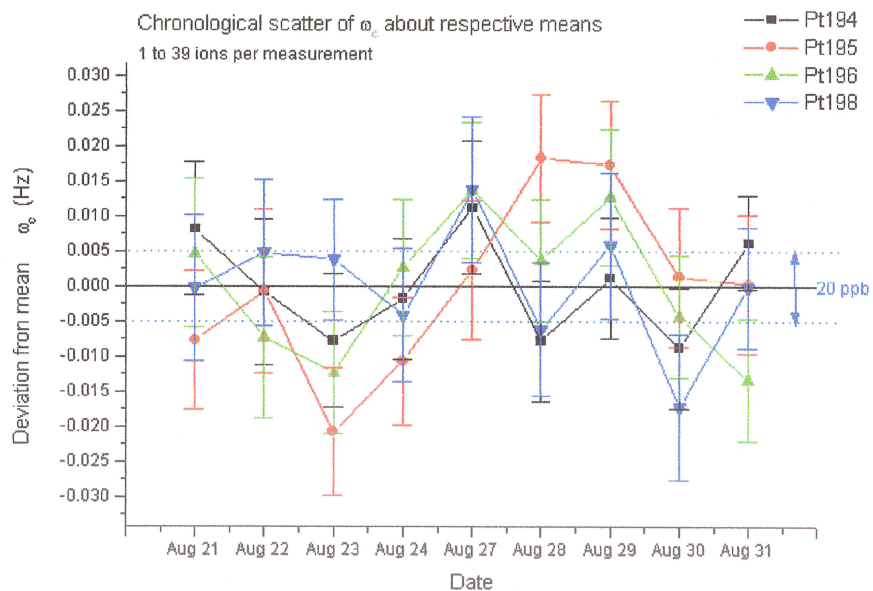
Fig. 8.3. Scatter of measured ω_c for the four Pt isotopes over a 2-week period

A scatter of 20 ppb over a period of 2 weeks indicates the apparent stability of the system as now the selected cold ions are executing orbital motions near the trap center, where field imperfections or inhomogeneities are minimal. The night/day temperature dependent magnetic field fluctuations are not discernable at the 20 ppb regime.

8.3. *Data Process*

The frequency ratio *R* is attained from each data set from which the atomic mass can be computed according to equation 4.53. In order not to be reliant on the quoted value for the reference mass (Au), the frequency ratios are tabulated. This will prove useful when a "new" value for the reference Au mass is computed using recent mass measurements from Manitoba II and complementary data from other laboratories. The data is binned according to ion number to provide an accurate comparison platform. The bin numbers are 1-39 ions, 1-24 ions, 1-19 ions, 1-15 ions and 15-39 ions. This binning is also conducted for the reference mass, to ensure consistency. A sample table for the frequency ratios (Table 8.2) is shown for the bin 1-39 ions. The mean frequency ratios for each bin size are presented in Table 8.3.

Table 8.2   Frequency Ratio *R* for the bin size 1-39 ions

| Date	^{194}Pt	^{195}Pt	^{196}Pt	^{198}Pt
Aug 21	1.015 487 009(31)	1.010 267 392(31)	1.005 111 185(33)	0.994 941 937(32)
Aug 22	1.015 487 036(28)	1.010 267 453(30)	1.005 111 205(30)	0.994 941 993(28)
Aug 23	1.015 487 058(37)	1.010 267 447(35)	1.005 111 179(25)	0.994 941 976(25)
Aug 24	1.015 487 038(27)	1.010 267 436(26)	1.005 111 211(26)	0.994 941 958(26)
Aug 27	1.015 487 066(30)	1.010 267 464(30)	1.005 111 255(29)	0.994 942 017(31)
Aug 28	1.015 486 988(32)	1.010 267 462(32)	1.005 111 207(28)	0.994 941 947(29)
Aug 29	1.015 486 994(28)	1.010 267 446(28)	1.005 111 209(28)	0.994 941 956(29)
Aug 30	1.015 487 014(34)	1.010 267 453(35)	1.005 111 168(32)	0.994 941 902(34)
Aug 31	1.015 487 011(22)	1.010 267 416(26)	1.005 111 152(25)	0.994 941 943(35)

Table 8.3   Mean frequency ratio *R* for the various bin sizes

Ion Bin	^{194}Pt	^{195}Pt	^{196}Pt	^{198}Pt
1-39 ions	1.015 487 024(9.7)	1.010 267 441(8.3)	1.005 111 197(10.6)	0.994 941 959(11.8)
1-24 ions	1.015 487 010(10.7)	1.010 267 428(10.7)	1.005 111 195(11.6)	0.994 941 951(10.3)
1-19 ions	1.015 487 006(12.2)	1.010 267 430(9.9)	1.005 111 195(10.0)	0.994 941 947(9.5)
1-14 ions	1.015 486 993(9.0)	1.010 267 426(8.2)	1.005 111 193(6.1)	0.994 941 945(6.0)

A few test runs were also made with very low ion numbers. These are illustrated in figures 8.4a and 8.4b showing a very well defined and symmetric line shape for an excitation time of 1.5 seconds. The extremely small ion cloud in both the cases shown (less than 5 and 10 ions respectively), orbiting in a very small region about the trap center, makes the problems associated with severe field imperfections and space charge distortion a non-issue. The possibility of making precision mass measurements with the TOF technique near the "single ion" limit has been illustrated (one of the design requirements of the CPT MS).
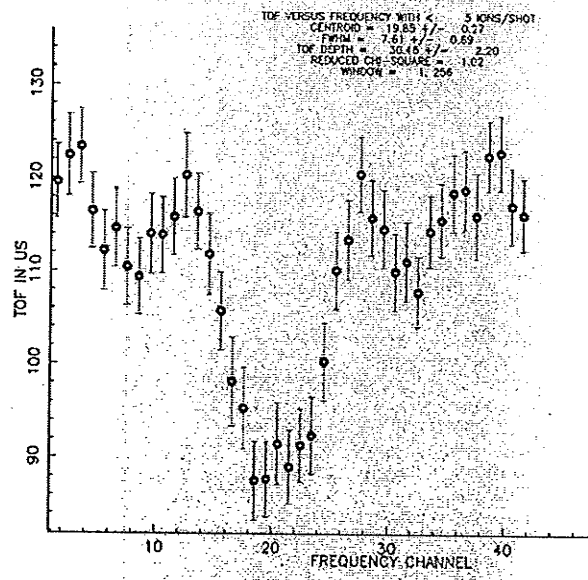
Fig. 8.4a. 1.5 second excitation spectrum for ^{195}Pt with less than 5 ions per measurement. The individual frequency channels are 0.075Hz apart
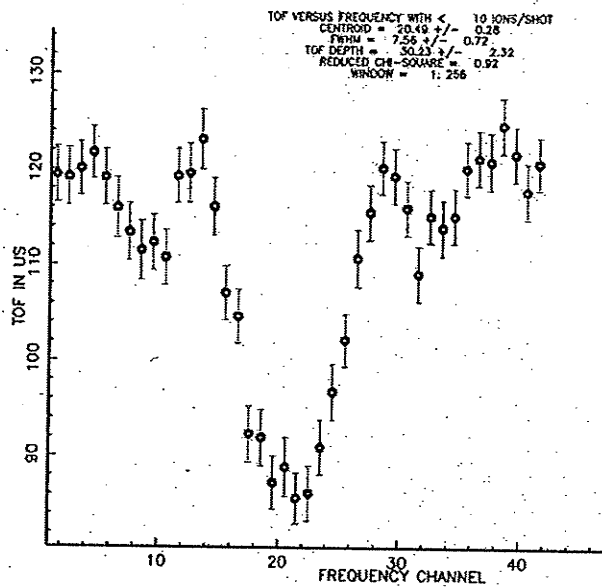

Fig. 8.4b. 1.5 second excitation spectrum for ^{194}Pt with less than 10 ions per measurement. The individual frequency channels are 0.075Hz apart

8.4. *Self Consistent Mass Value for* ^{197}*Au with Least Squares Adjustment*[1]

The reference mass, ^{197}Au, enables the atomic mass of the various Pt isotopes to be computed with ease. An accurate reference mass is thus a pre-requisite for accurate experimental mass results for the CPTMS. The reference mass can readily be obtained from most recent Atomic Mass Evaluation (AME) tables. The other option is perform some method of self-consistent determination for the reference mass using reliable "local" mass measurements and reaction Q values. The author would like to state that in any case, in mass regions where no discrepancy is suspect, the AME tabulation and the "local" mass measurement/Q value computation would have little or no discernable difference. For this work, it was decided that the mass region A=180-200 is plagued with far too many inconsistencies. A limited (over 20 mass units) least squares adjustment (LSA) is therefore performed in the region A=180-200 from which a self-consistent value for the mass of ^{197}Au is obtained.

The "local" mass measurement data used for this LSA is a set of Mercury (Hg) measurements performed on the "upgraded" Manitoba II spectrometer between 1996-1999. This study was part of a series of experiments designed to confirm a prior result set of Hg measurements done by the University of Manitoba's AMD group in 1980. This "local" data is then combined with the input values given in AME 95 for the relevant mass region from which the output values are obtained in a self-consistent manner (see Audi 1986, Sharma 1977 and references therein for the Least Squares technique).

The 3 "absolute mass" doublets "added" to the existing body of AME data is marked "A", "B" and "C" (Barillari 1999). It would be instructive to note that doublet "A" is actually a re-measurement, originally done in 1980 (Kozier 1980). Table 8.4. below shows the values for both these measurements.

Table 8.4. Two independent measurements on doublet "A"

Doublet "A"	Barillari 1999	Kozier 1980
^{199}Hg-^{12}C$_2$^{35}Cl$_5$	124017.19 (1.48)	124 023.43 (0.53)

These "new" input measurements are shown in figure 8.5. The doublet "D" refers to an absolute mass measurement for ^{201}Hg done in 1980. The reaction data (Q values), "*a*" and "*b*" (Table 8.5.) are other complementary data that will be used as a "reaction bridge". These would enable the mass of ^{197}Au to be calculated from the mass of ^{198}Hg via the chain a, b.

Table 8.5. Complementary Q value data

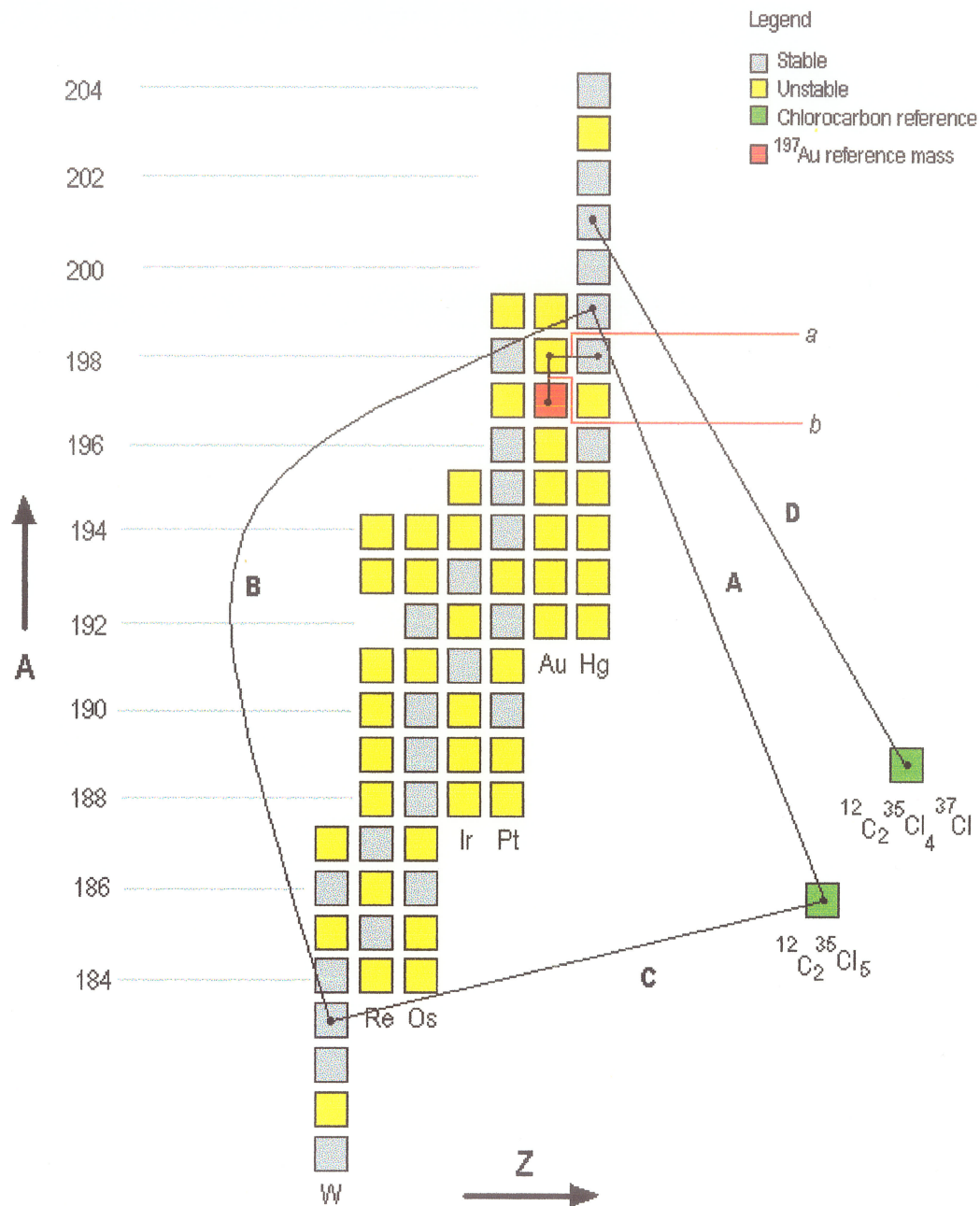| Code	Reaction	Decay Mode	Q value (keV)	References (as in AME 93)
a	^{198}Au-^{198}Hg	β^-	1 372.40 (0.60)	65Ke04, 65Pa08
b	^{198}Au-^{197}Au	(n, γ)	6 512.20 (0.22)	79Br26

Fig 8.5. "Local" data for Least Squares Adjustment (A=180-204)[1]

A selection of the LSA output values is shown in Table 8.6. Comparison values are shown where applicable (the default comparison value is of course, from AME 95 (in *italics*). A reliable mass value for ^{197}Au is the prime objective of this LSA exercise. An accurate mass value for ^{198}Hg (verified independently

by two or more experiments) would prove invaluable in this instance. The very short reaction chain itself leaves little room for error. The result for the calculated ^{197}Au mass will therefore be highly reliable.

The author would like to state that the LSA output values is just a set of best values given the number of constraints imposed by mass measurements and reaction Q values. Reliability is ultimately ensured by correspondence to other data, <u>not</u> included in the LSA. An excellent illustration of this is for masses ^{198}Hg and ^{204}Hg (see table). Bergstrom, from the SMILETRAP collaboration, had presented results at ENAM 2001 that agrees very well with the LSA output values for these two masses. The ^{204}Hg mass, as presented by Bergstrom, even agrees with the Manitoba II result from 1980 (Barber 2002-priv comm.)!

Table 8.6. LSA output values and comparison for certain masses

	LSA Output (µu)	Comparison (µu)	Reference
^{183}W	182, 950, 223. 39 (0.61)	182,950,224. 20 (3.00)	AME 95
^{184}W	183, 950, 931. 51 (0.67)	183, 950, 9 32.30 (3.00)	AME 95
^{186}W	185, 954, 363. 84 (1.23)	185, 954, 362. 00 (3.00)	AME 95
^{187}Re	186, 955, 752.11 (1.15)	186, 955, 750. 50 (3.00)	AME 95
^{194}Pt	193, 962, 678. 56 (0.97)	193,962,663. 58 (3.00)	AME 95
^{195}Pt	194, 964, 789. 42 (0.97)	194,964,774. 45 (3.00)	AME 95
^{196}Pt	195, 964, 949. 92 (0.96)	195,964,934. 88 (3.00)	AME 95
^{198}Pt	197, 967, 891. 33 (3.35)	197,967,876. 01 (4.00)	AME 95
^{197}Au	196, 966, 567. 87 (0.70)	196, 966, 551. 61 (3.00)	AME 95
^{198}Hg	197, 966, 768. 55 (0.43)	197, 966, 777. 49 (0.78) 197, 966, 774. 10 (0.76) 197, 966, 771. 27 (0.68) 197, 966, 767. 88 (0.66) 197, 966, 768. 40 (0.60)	(i) (Kozier 1980) Manitoba II AMD^2 (ii) (Kozier 1980) Manitoba II AMD^2 (iii) (Barillari 1999) Manitoba II AMD^2 (iv) (Barillari 1999/Kozier 1980) AMD^2 (v) (Bergstrom 2001) SMILETRAP
^{199}Hg	198, 968, 281. 36 (0.42)	198, 968, 287. 08 (0.55)	(Kozier 1980) Manitoba II AMD^2
^{201}Hg	200, 970, 304. 26 (0.50)	200, 970, 308. 97 (0.63)	(Kozier 1980) Manitoba II AMD
^{204}Hg	203, 973, 494. 04 (0.41)	203, 973, 494. 22 (1.26) 203, 973, 494. 20 (0.60)	(Kozier 1980) Manitoba II AMD (Bergstrom 2001) SMILETRAP

^{2} The various data checks are shown as Q value/mass measurement schemes in fig. 8.6
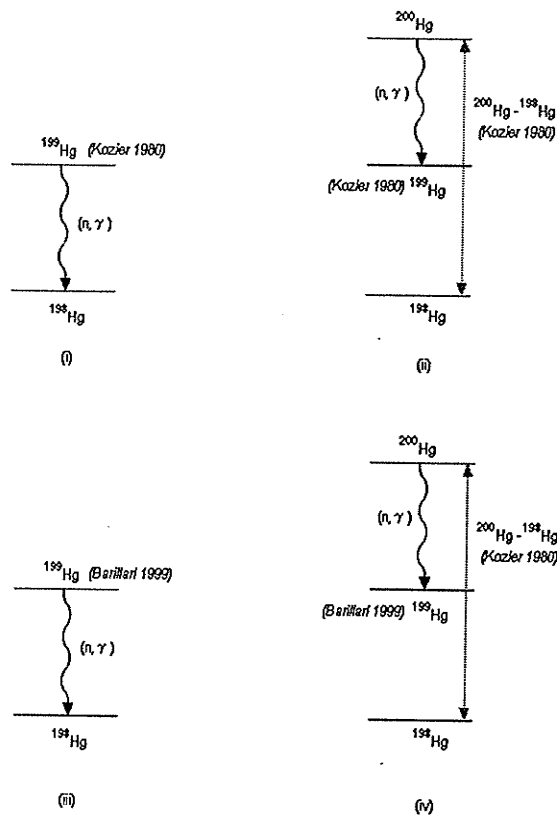
Fig. 8.6. Checks on ^{198}Hg mass with Manitoba II data
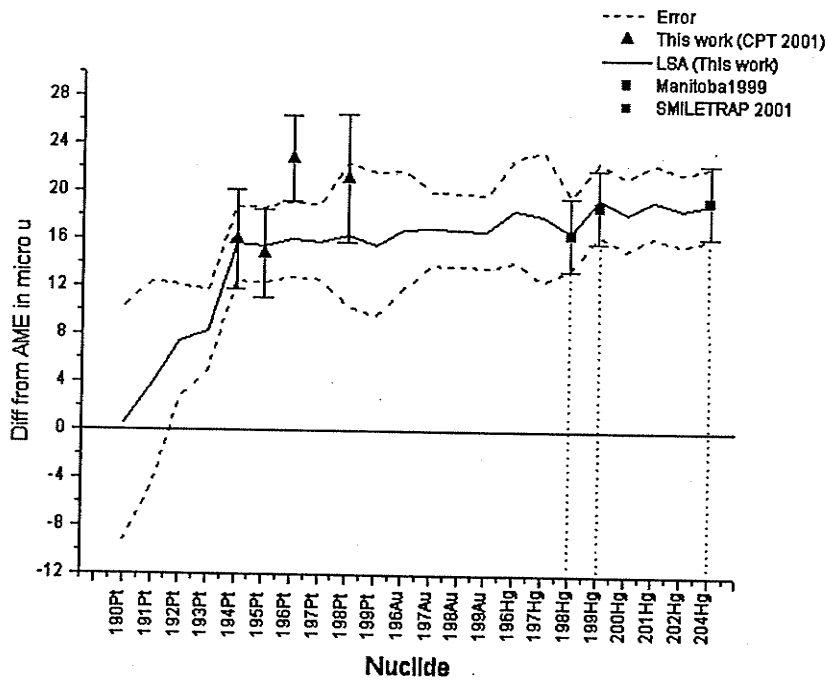
Fig. 8.6b. LSA output values shown as deviation from AME.

Fig. 8.6b shows the LSA output values as deviation from the AME. The independent Hg measurements of SMILETRAP are also inserted. The 16 keV shift around A=200 first noted by the Manitoba AMD group is evident from this plot.

This value for ^{197}Au (from LSA) and that quoted in AME 93 are given for reference in Table 8.7.

Table 8.7. Atomic Mass of ^{197}Au

	Atomic Mass ^{197}Au (µu)
Atomic Mass Evaluations (AME) 93[a]	196,966,551.61(3.00)
Least Squares Adjustment (LSA)	196,966,567.87(0.70)

8.5 *Atomic Masses for Platinum*
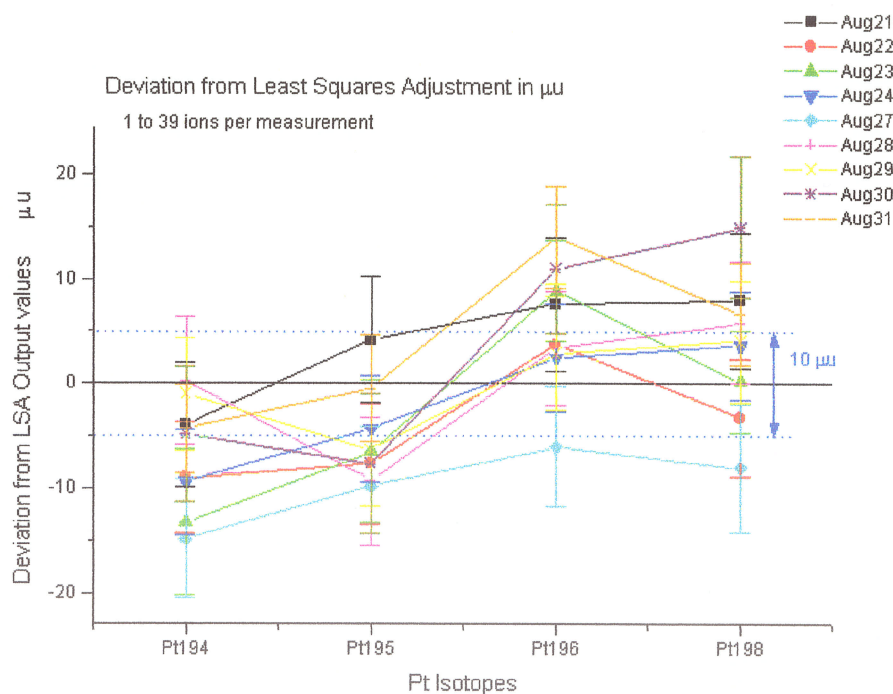
Fig. 8.7. Scatter of measured masses for bin 0-39 ions, shown as deviation from LSA output values
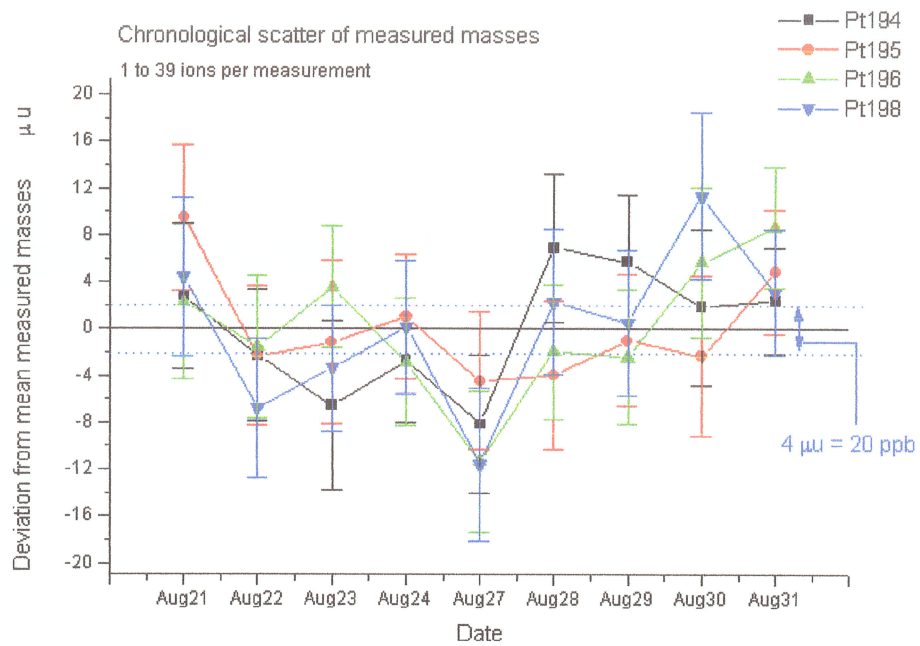
Fig 8.8. Data "reproducibility" as indicated by the day-to-day variations.
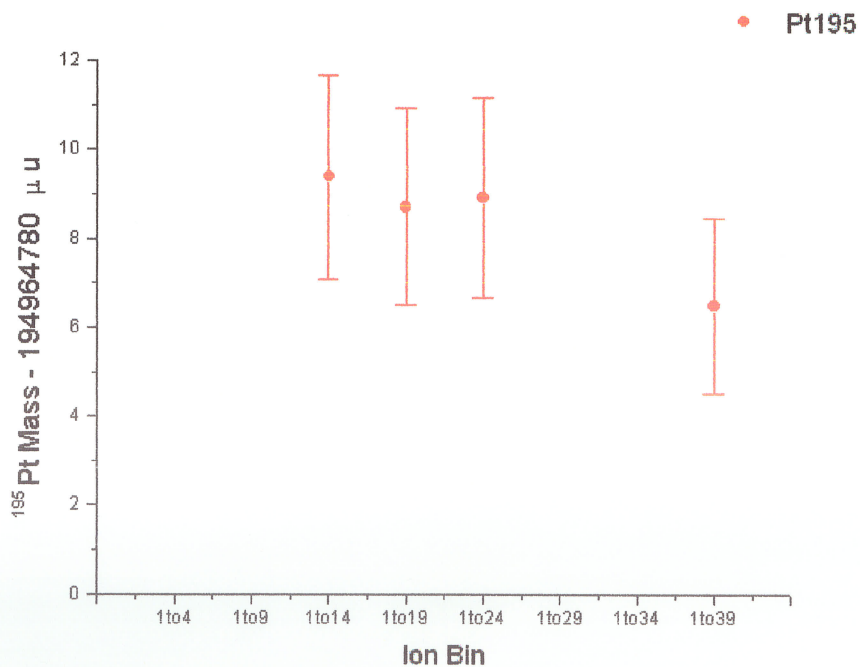
Fig. 8.9. Measured masses (no "wide" calibration) for ^{194}Pt according to ion number

The day-to-day run results are shown in the figures on the previous page. Figure 8.7 illustrates the scatter of the measured masses from the LSA output values for the four isotopes. The relative increased scatter in the results for ^{198}Pt points to a condition where "cleaning" majority of the stored ions starts to disturb the resonance (^{198}Pt abundance ~8% therefore 92% of the stored ions are removed). Driving out most of the stored ions through strong dipole excitation might cause the excited ions to agitate or indirectly excite the small number of the ions of interest through collisions.

The measured masses over two weeks are self-consistent with a variation not greater than 4µu. This translates into 20ppb (2×10^{-8}) stability for any independent measurement. The result for one isotope, ^{195}Pt, is shown in fig. 8.9. The variation of the measured masses between bin sizes with small ion number increment is negligible (Fig. 8.9). The ion bin 1-19 ions is chosen as the "final result" representative bin as this is a small ion cloud with sufficient statistics. The error bars indicate the error in the mean δ_{mean},

$$\delta^2_{mean} = \frac{\sigma^2}{\sqrt{N(N-1)}}.$$ (8.7)

Measured masses for the four platinum isotopes are listed according to ion number in Table 8.8. The error in the mean is quoted in brackets.

Table 8.8 Raw Results (no "wide" calibration)

Isotopes	^{194}Pt	^{195}Pt	^{196}Pt	^{198}Pt
0-39 ions	193,962,671.85(1.80)	194,964,785.09(1.56)	195,964,955.22(2.01)	197,967,894.87(2.29)
0-24 ions	193,962,674.51(1.99)	194,964,786.52(1.89)	195,964,955.52(2.20)	197,967,896.46(1.99)
0-19 ions	193,962,675.27(2.27)	194,964,786.30(1.86)	195,964,955.52(1.89)	197,967,897.31(1.84)
0-14 ions	193,962,677.67(1.68)	194,964,786.98(1.54)	195,964,955.92(1.15)	197,967,897.69(1.15)
LSA	193,962,678.56(0.97)	194,964,789.42(0.97)	195,964,949.92(0.96)	197,967,891.33(3.35)
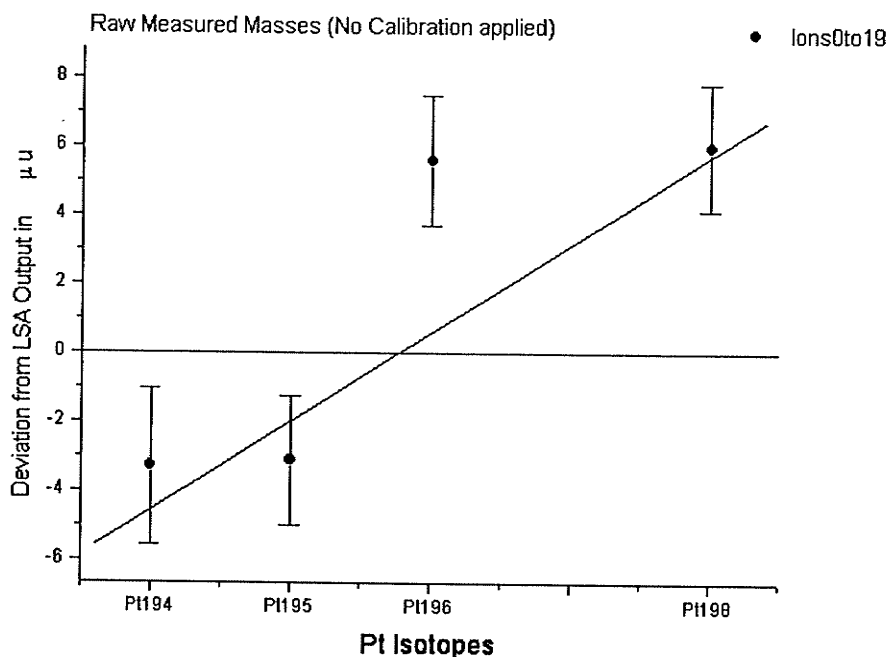
Fig. 8.10. Measured mass values for the 1-19 ion bin (uncalibrated), shown as deviations from LSA.

A distinct pattern emerges from the figure 8.10. Compared with the LSA output, ^{194}Pt and ^{195}Pt are measured to be systematically lower while similarly ^{196}Pt and ^{198}Pt are deemed to be higher. A mass dependent "systematic" error is present in these measurements. This is probably due to a slight misalignment of the trap axis to the magnetic field. To correct for this effect, a "wide" calibration using an organic species, C_5H_8 (A~68) is performed and the corrected results are shown (Table 8.9, fig. 8.11).

Table 8.9. Final "Wide" Calibrated Results

Isotopes	^{194}Pt	^{195}Pt	^{196}Pt	^{198}Pt
0-39 ions	193,962,675.45(2.54)	194,964,786.49(1.97)	195,964,956.42(2.10)	197,967,893.67(2.37)
0-24 ions	193,962,678.11(2.68)	194,964,788.92(2.24)	195,964,956.72(2.28)	197,967,895.26(2.07)
0-19 ions	193,962,678.87(2.89)	194,964,788.70(2.21)	195,964,956.72(1.98)	197,967,896.11(1.94)
0-14 ions	193,962,681.27(3.12)	194,964,789.38(2.31)	195,964,957.12(2.18)	197,967,896.49(2.44)
LSA	193,962,678.56(0.97)	194,964,789.42(0.97)	195,964,949.92(0.96)	197,967,891.33(3.35)
AME 95	193,962,663.58(3.00)	194,964,774.45(3.00)	195,964,934.88(3.00)	197,967,876.01(4.00)
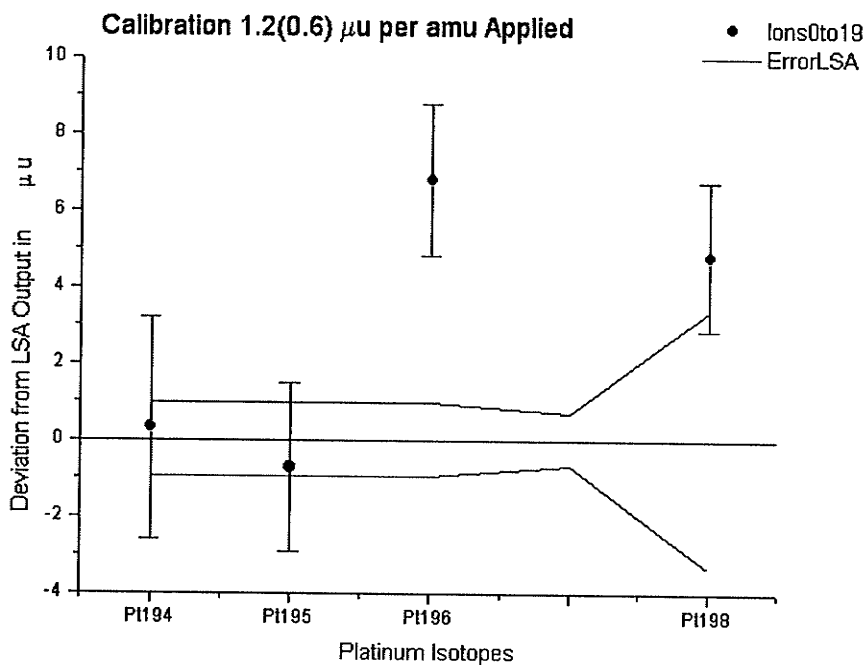
Fig. 8.11. Final calibrated results shown as deviation from LSA.

Table 8.10. Deviation of masses from LSA

Nuclide	Measured (μu)	δ_{Meas} (μu)	σ_{ext} (μu)	σ_{int} (μu)	Deviation from LSA (μu)	Deviation from LSA (σ)
^{194}Pt	193,962,678.87	2.90	2.80	3.08	0.31	<σ
^{195}Pt	194,964,788.70	2.21	2.19	2.77	-0.72	<σ
^{196}Pt	195,964,956.72	1.98	2.01	2.52	6.80	3.5σ
^{198}Pt	197,967,896.11	1.94	1.87	2.52	4.78	2.3σ

Final mass values for the four Pt isotopes are stated in Table 8.10. The deviations from the Least Squares Adjustment output values are also given. The reader is directed to fig. 8.6b where the relative deviation from AME is illustrated. The 16 keV shift in the results of this work is evident.

Chapter 8. References

- Audi, G., Davies, W. G. and Whiting-Lee, G. E. (1986). *Nuclear Instruments and Methods in Physics Research*, A249, pg. 443-450.
- Barber, R. C. (2002). Private communication.
- Barillari, D. K. (1999). *PhD Thesis. University of Manitoba*. Winnipeg, Canada.
- Bergstrom, I. *et al.* (2001). *Exotic Nuclei and Measurements (ENAM) 2001*, Helsinki, Proceedings, in print.
- Kozier, K. S., Sharma, K. S., Barber, R. C., Barnard, J. W., Ellis, R. J. and Derenchuk, V. P. (1980). Canadian Journal of Physics, Volume 58, Number 9, pg. 1311.
- Sharma, K. S., Meredith, J. O., Barber, R. C., Kozier, K. S., Haque, S. S., Barnard, J. W., Southon, F. C. G. and Williams, P. (1977). *Canadian Journal of Physics*, Volume 55, pg. 1360.
- Wapstra, A. and Audi, G. (1985). *The 1983 Atomic Mass Evaluation, (I). Atomic Mass Table*, Nuclear Physics, **A432**, pg. 1-11.
- WebElements. (2002). *www.webelements.com*.

9. Conclusion

High accuracy mass measurements have been performed on the CPT mass spectrometer for four platinum isotopes. For these isotopes a measurement precision of 10-15ppb has been attained corresponding to about 3keV. The attainable precision to some extent is limited by the magnetic field homogeneity, which deviates from the design specifications (see Appendix I). The complex task of magnetic field correction/compensation remains a pressing concern for mass measurements, with precision in the ppb (~1keV) regime. Progress on the magnetic field correction is not expected in the immediate future as the primary role of the CPT MS involves mass measurements of exotic nuclei. For these experiments a precision in the region of 20ppb is considered "excellent".

The author restates that results obtained in this work were largely due to the effective "cleaning" scheme, where only very cold ions were pre-selected for mass measurement, even with a less than ideal energy bunching mechanism. It would thus be incorrect to expect results of similar precision for online experiments, where very low production yields prevents the use of the "ring raising" process. The energy bunching process prior to Penning trap injection must now be refined, as the original goal to place an ion cloud tightly bunched in energy, very near the bottom of the trapping potential, cannot be circumvented.

A linear trap has recently replaced the RFQ buncher trap in an effort to improve collection efficiency, a factor crucial in online mass measurements. The linear trap offers an acceptance that is a better match to the emittance of the incoming beam. The ion bunch ejected from the linear trap also possesses a smaller energy spread. This spread is calculated to be small enough that the energy-bunching cavity has been deemed redundant in this new setup. Currently, tests are being conducted on the new configuration.

The results obtained in this work are largely satisfactory. The requirement for these measurements was relatively straightforward, that is, a pure, small and cool ion cloud orbiting near the trap center. The scatter of 40ppb in the "raw" resonance frequencies of the platinum isotopes over a period of two weeks (Fig. 8.3) illustrates the benefits of adhering to this "requirement".

The limited LSA procedure has provided a "new" mass value for ^{197}Au. This has been independently confirmed by more than one source. The root of this lies in a "new" mass for ^{198}Hg and ^{204}Hg presented by the Stockholm/Mainz TRAP group. These results compare very well with Manitoba's 1980 and 1999 Hg mass measurements. The Pt measurements in this work with the "new" reference ^{197}Au mass, closely match the LSA output values. Three very different mass measurement facilities performing mass measurements separated by a time period of almost 20 years have produced results that agree very well with each other. The only exception is ^{196}Pt, which is determined to be systematically heavier when compared to the LSA output values. This might be due to local reaction Q value inconsistencies.

Further stable mass measurements in the higher end of the mass table are planned. The author would consider absolute mass measurements to be performed in this region as a high priority. Similar to the Manitoba II, reference species of hydro/chlorocarbons will dispense with the need to "qualify" the reference itself! The CPTMS has already been measuring hydrocarbons originating from organic contaminants as the reference species during online experiments.

The present precision limit of 10ppb is adequate for a systematic study of "heavy" masses between 180-200amu. A series of Hg measurements with the CPT MS would be considered ideal if not for ionization difficulties. Attempting "laser desorption" with a sample of liquid Hg would not be prudent with regards to safety. The author proposes a simple scheme, adopted from the Manitoba II high-resolution mass measurement system. Simple heating of externally housed vials of $HgCl_2$ and C_2Cl_6 will introduce vapors into the cooler confines (Barillari 1999). An ionization gauge could then be used to ionize the vapors. The principle of ionization is similar to that used to introduce gas samples (*e.g.* Xenon) into the CPT MS. Mass measurements can then be performed on $Hg^+(A\sim200)$ isotopes with $C_2Cl_5^+$ as the reference species. The only problem might be the difficulty in Hg ionization. In this instance, the only option would be to feed Hg^+ ions directly into the cooler using some configuration of an external electron bombardment source. A simpler experiment, not to be nostalgic, would be a measurement of ^{197}Au itself in conjunction with $C_2Cl_5^+$. No prior logistic planning is needed except for the ionization of the reference chlorocarbon. It would be prudent however to firstly, completely characterize the "mass dependence" of the spectrometer through a series of widely spaced hydrocarbon mass measurements.

The thrust towards "high precision" online mass measurements is currently the focus of the CPT research group. Though this work predominantly involves offline stable mass measurements, improvements were made with "online compatibility" in mind. Current status shows the "Gas Cooler" collection system in excellent operational condition. The installation of the magnetic quadrupole triplet in conjunction with the velocity filter has increased the signal to noise ratio by a factor of seven (Savard 2001). The pioneering effort of the CPT research group has made the stopping, collection and post acceleration of fast beams a reality! A "Penning Trap" isobar separator is presently being developed to ensure "clean" beam injection into the CPT MS. The presence of isobaric organic contaminants is the only factor hindering high precision exotic nuclei mass measurements at the moment.

Chapter 9 References

- Barillari, D. K. (1999). *PhD Thesis*, University of Manitoba, Winnipeg, Canada.
- Savard, G. (2001) – private communication.

Appendix I   The Superconducting Magnet System

The superconducting magnet system is an integral part of the CPTMS. This magnet until now has been a closed system sealed in a black box. The complexity, coupled with the immense cost of superconducting systems does not provide for the occasional tinkering by graduate students not skilled in this field. Nalorac Cryogenics Corporation (NCC) constructed the CPTMS 5.9 Tesla magnet under strict specifications from the CPT design team. The need for strict guidelines is warranted as the homogeneity over a dsv (diameter spherical volume) of 1cm at the coil center was pegged at 100ppb. The CPT magnet is a standard LTS system (Low Temperature Superconducting), using metallic conductors as opposed to exotic HTS (High Temperature Superconducting) oxide/ceramic conductors. The intrinsic difference between the two classes is the all-important critical temperature or T_c. LTS system operate at a temperature of 4.2-20K while HTS system achieve superconducting state at a temperature of 20K-110K. HTS is a burgeoning field on its own, propelled by the search for the Holy Grail of room temperature superconductivity!

LTS magnet systems use superconduction to maintain the currents that are required to generate large magnetic fields with no power loss. Liquid Helium (LHe) is used to cool the conducting elements down to the transition temperature where they exhibit no resistance. The absence of resistance enables large currents to be passed through very thin wires. The thin wires provide for thousands of turns to be wound over a small section giving rise to a relatively compact high field magnet system. This can be compared to the traditional copper conductor, water-cooled magnets systems (up to 2 T max), which require a much larger installation area.

The initial powering up, or energizing of the superconducting coils, is the only time that power is fed into the system. Once the cryogenic chamber is sufficiently cooled with the influx of LHe, and the required currents has been established in the coils, the external driving power supply is disengaged and the current circulates without loss. The only periodic maintenance required is the quarterly filling of LHe that is done with the coils energized. Minor field corrections are required if severe inhomogeneity is suspected. This is done by changing the currents in the superconducting corrective shim coils with the use of the external driver supply. This section will serve as a primer to LTS magnet system design and operation. Emphasis will be directed towards field mapping and the use of active shimming components to correct inhomogeneities.

A1.1 General Internal assembly

The cryogenic nature of the magnet system places the innermost section at LHe temperature (4.2K) while the entire magnet assembly is situated at room temp (300K). This is an insulation nightmare, as any oversight in thermal protection will result in excessive LHe boil off, increasing the operational cost. The LTS elements are housed within three layers of "insulation". The outer layer with one end at room temperature is made of a composite superinsulative material. This is followed by a 95 liter LN_2 jacket that ensures a temperature of 77K at the junction. The innermost cavity, housing the superconducting elements, is filled with LHe with a helium vapor jacket (Fig. A1.1).
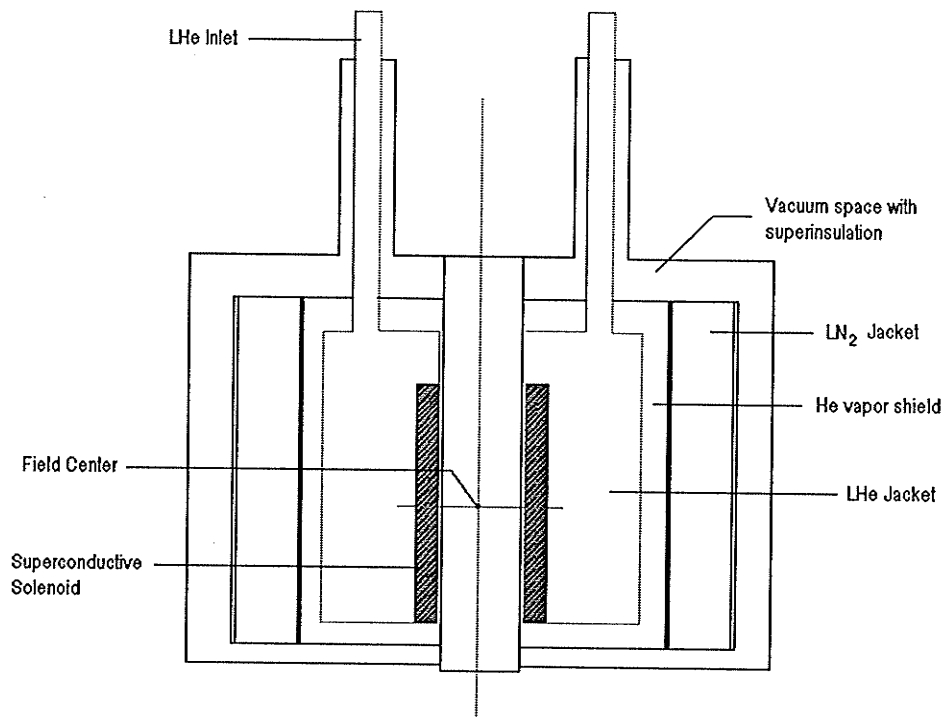
Fig. A1.1 Nalorac 5.9T superconducting magnet

The LTS elements are a series of specially wound Niobium-Titanium (Ni_3Ti) coils, which define the magnetic field within the region. The coils are wound around a bobbin in which sits the 8.9cm diameter bore, which will houses the precision Penning trap. The coils are a stand-alone system once the "persistent" superconducting currents (*i.e., they maintain constant current flow without additional power*) are established during initial power-up. The energizing is performed with the coils connected to a power supply at room temperature. A set of special switches is placed within the enclosure to allow for current entry (during power-up) and current exit (during power-down) to the LTS coil system. One switch is placed in series with the superconducting load and the other is placed in parallel. During external current drive connection (e.g. during power-up), the series switch is closed while the other switch is open. This allows for current to flow through the coils from the driver source. The parallel switching device serves as a shunt in that when the series switch is open and the shunt switch is closed, current recirculates through the persistent superconducting load (Fig. A1.2). The switches are special thermally activated superconductive devices of material that is conductive at LTS temperature but not conductive at higher temperatures. The transition between closed and open states in achieved through small resistive elements interspersed around the switches, which is activated via thin low-current leads passing into the chamber. All the coils (main coil and active shim coils) are activated through a single switching trigger mechanism in that when the load is persistent, all coils are superconducting. This has the implication that during the field corrective shimming process, the main coil is being driven by the external supply and care must be taken not to alter this current.
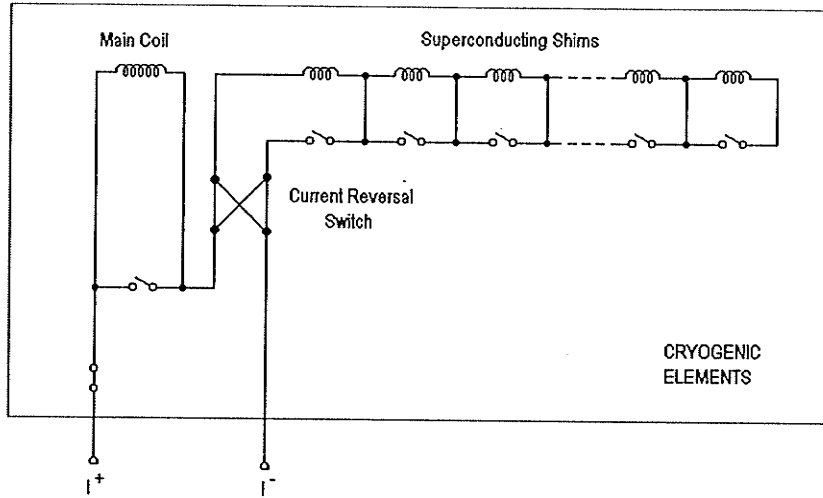
Fig. A1.2 Internal coil configuration. The switch positions correspond to "external supply drive".

A1.2 *The Coil Assembly*

The LTS solenoid consists of a 2-section main coil plus a series of correction coils wound around the main coil. Each coil is independent in a sense that different currents flow through individual coils. The correction or auxiliary coils are used to produce fields to compensate for the inhomogeneities present in the field produced by the main coil B_0. In this particular magnet system, the total coil count is 10. The main Z^0 coil plus nine correction coils z^1, z^2, z^3, x, y, xz, yz, xy and $x^2 - y^2$. The optimum corrective currents in these coils must be determined experimentally through an iterative field mapping technique. It would be instructive to first perform a simple mathematical treatment of the field present within the bore in the vicinity of the magnet center before the field correction principle is explored. A general scheme is to write the field as an expansion of spherical harmonic functions as follows:

$$H(r,z,\phi) = \sum_{l=0} \sum_{m=0}^{l} \left(\frac{r}{a}\right)^l [A_{lm} \cos m\phi + B_{lm} \sin m\phi] P_l^m \cos\theta. \qquad (A1.1)$$

At this juncture, no symmetry is assumed as the sum is over all general components. The variable a denotes the radius of the main coil and:

$$P_{lm}(x) = \frac{(-1)^m}{2^l l!} (1 - x^2)^{m/2} (d/dx)^{l+m} [(x^2 - 1)^l], \qquad (A1.2)$$

are the associated Legendre polynomials. The terms in A_{lm} and B_{lm} denote the gradient strength of the field. The above expansion can be rewritten using cylindrical coordinates so as to separate the z components from the off-axis components:

$$H(r,z,\phi) = H_0 + 0(z, z^2, z^3 ....) + A_{11} r \cos\phi +$$

$$B_{11} r \sin\phi + A_{21} zr \cos\phi + B_{21} zr \sin\phi +$$

$$A_{22}r^2 \cos 2\phi + B_{22}r^2 \sin 2\phi + \text{.......} \qquad \text{(A1.3)}$$

Re-inserting the Cartesian components with $x = r\,cos\phi$ and $y = r\,sin\phi$, attain:

$$H(x, y, z) = H_0 + 0(z, z^2, z^3 ....) + A_{11}x +$$

$$B_{11}y + A_{21}zx + B_{21}zy +$$

$$A_{22}(x^2 - y^2) + B_{22}xy + \text{.......} \qquad \text{(A1.4)}$$

The field now has been decomposed into the main component H_0 and nine other components (eqn. A1.4). It would be instructive to note that each individual shim coil can correct or compensate for a particular component (Marek 1994). The discussion has been restricted to second order in off axis elements as the CPT magnet is fitted with only second order off axis corrective coils.
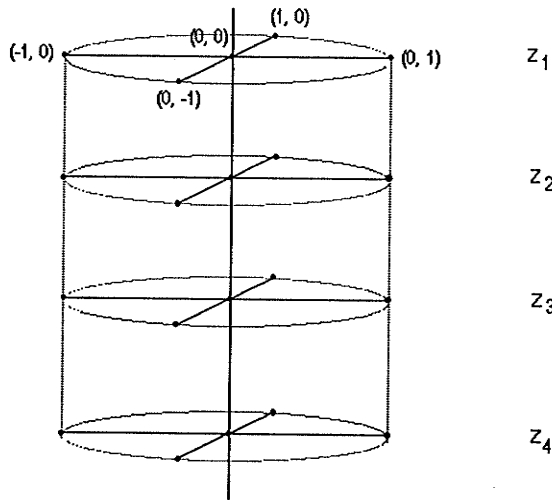
A1.3 *Field Mapping and Correction*

Fig. A1.3 Field mapping point scheme.

The especially simple arrangements of the shim coils make any field correction process rather trivial. The shimming process used is active as opposed to the passive shimming process. Active shims are current carrying coils wound around the main coil while passive shim are magnetic materials placed in special housings placed at strategic locations. The basic principle in active shimming is to generate small auxiliary fields to cancel out any inhomogeneities present from the various off axis components. Firstly, field mapping is required to ascertain the degree of inhomogeneity. The map would also provide crucial information that would enable the operator to "plot" a shim solution. The map is done around a volume of interest, say, a cylinder of radius 1cm and a height of 4 cm. "Extreme" field mapping is done with a couple of hundred points and the solution is plotted using special computer code. To illustrate the process, the author has decided to simplify the rigor to just a couple of points. The spirit, however remains and the reader can go forth and extend the mapping detail. The mapping scheme is such that for every z position,

four points are taken. These are (1, 0), (0, 1), (-1, 0) and (0, -1). The reference frame is arbitrary and can be set by the operator. In azimuthal angle ϕ, these points translate to 0, 90, 180 and 270 degrees respectively. The z position map is of course (0, 0). Thus 5 field values are taken as a set. In matrix form, equation (A1.4) can be written as:

$$
\begin{pmatrix}
r & 0 & zr & 0 & r^2 & 0 \\
0 & r & 0 & r & -r^2 & 0 \\
-r & 0 & -zr & 0 & r^2 & 0 \\
0 & -r & 0 & -zr & -r^2 & 0
\end{pmatrix}
\begin{pmatrix}
A_{11} \\
B_{11} \\
A_{21} \\
B_{21} \\
A_{22} \\
B_{22}
\end{pmatrix}
=
\begin{pmatrix}
\Delta_1 \\
\Delta_2 \\
\Delta_3 \\
\Delta_4
\end{pmatrix}
\qquad (A1.5)
$$

where Δ_I denotes $B_i - B_{oi}$, with B_i as the field at a particular off axis point and B_o is the field on axis at the same z coordinate. The above matrix equation consists of six unknowns and four independent equations. To achieve a self-consistent solution space, it might be recommended that a few more map points be used, for example at different z coordinates, in order for the number of equations to exceed the number of unknowns. The procedure used is not perfect as no information on the B_{22} can be obtained from the map points. The user can include another map point where $\phi = 45°$, which would give a non-vanishing component for B_{22}. The solution attained for the field gradients can be related to the shim coil current almost linearly and will serve as a starting point for any iterative active shimming procedure.
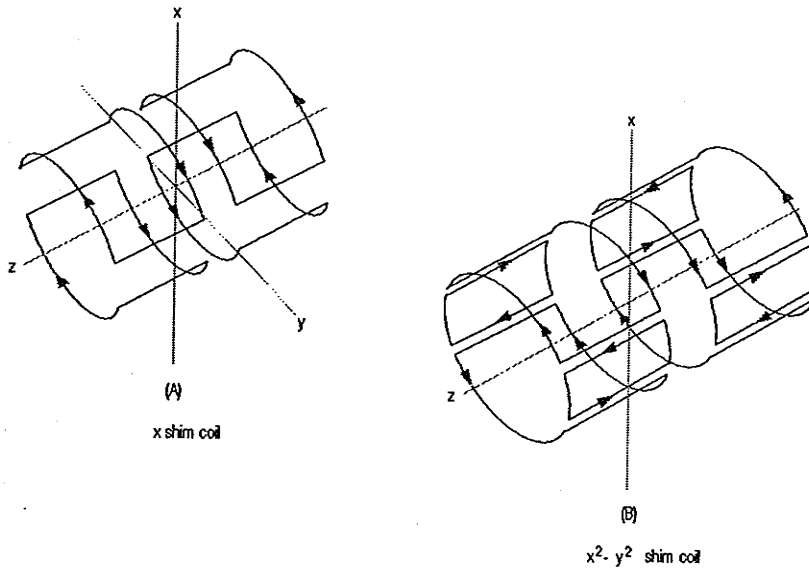

Fig. A1.4 Shim coil patterns. (A) x shim and (B) $x^2 - y^2$ shim.

The independent nature of the shim coil configuration entails that all shim coils are operational to achieve a high degree of homogeneity within the dsv in question. No amount of hard driving one particular shim can correct for another shim. Thus a system with inactive shim coils will never perform to design

specifications. The CPT magnet-shimming configuration currently is performing far below optimum. The last shimming exercise conducted in February 2001 has determined that the xz and yz shim coils are not operational. The third order axial shim, z^3 and the x shim are severely current limited. Field variation on axis is 0.9ppm/cm. A measurement at the field center z position (trap center), along the x and y-axis, puts a variation of 7.8ppm/cm along the y-axis and 10.5ppm/cm in the x direction.

The superconducting nature of the shim coils does not allow for any in-house attempt at maintenance. The proposed solution was to install non-cryogenic correction coils coaxially around the magnet, coupled to an external current driver. The use of shim coil technology is common in medical NMR instruments. NMR industrial research groups regularly patent external field compensation techniques. One such technique involves field compensation using coil patterns etched on flexible insulating material (Sakakura 1997). The coils are then "wrapped" over a portion of the magnet bore. This provides an elegant solution to the otherwise complex task of dealing with field corrections for superconducting magnet systems.

Coil geometries for the various configurations are well known (Yamaguchi 1987). The figure A1.4 shows the geometries for x and x^2-y^2 coils. The current flow direction is indicated and the coil will be etched so that this "order" is preserved on the 2 dimensional patterns. A "possible" etch pattern is shown for the simple x shim coil (Fig. A1.5). The reader can observe that the current flow has been followed faithfully on the etched coil through a series of strategically placed jumpers. The jumpers are sections where currents cross in 2 directions (dark and light arrows). In practice, the coils are multi-layer insulated conductors. This is similar to printed circuit fabrication using stacked conducting tracks separated by an insulating oxide layer.
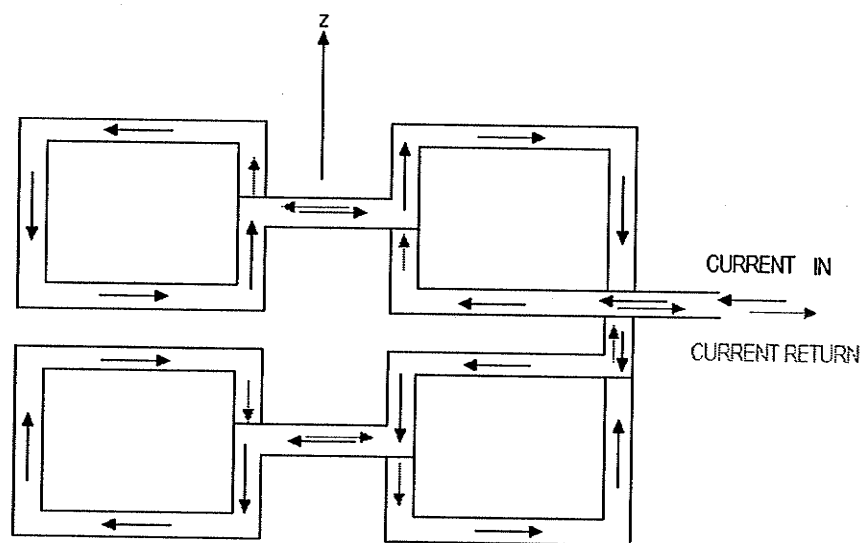

Fig. A1.5 X shim coil 2D etching pattern

FourPhd defensePhdPhD defense external shim coils are required, each with its own variable current driver. The current source needs to operate at a maximum load of 5A with long-term stability in the milliamp range. No water-cooling of the conducting tracks is possible, so thermal stresses must be

considered at the design stage. The various shim coil sheets would be wrapped over the magnet bore, in a concentric pattern. This might pose a problem as the space between the magnet bore and the existing bore tube is limited. Present technology enables a system of 5 shims coils to be stacked (2 coils per circuit, etched back to back) with a total thickness not exceeding 3mm (Fig. A1.6). This technique was the subject of a patent filed by Sakakura and his team at Toshiba, Kawasaki, Japan, in 1998.
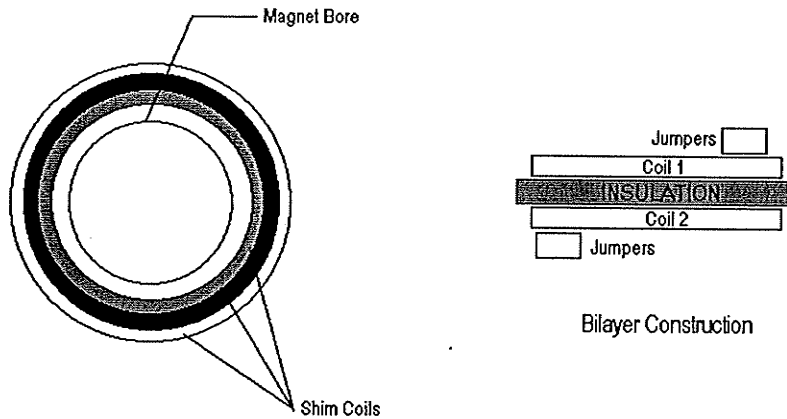

Fig. A1.6 Shim coil installation and construction.

Appendix A1 References

- Marek, D, Haberli, M, Burgers, M and Riboulet, J.C. (1994). *United States Patent*, 5,373,239.
- Nalorac Cryogenic Corporation (NCC) User Handbook.
- Sakakura, Y, Hiromi, N-M, Kawamoto, Y and Masafumi, K.S. (1998). *United States Patent*, 5,773,976.
- Yamaguchi, K, Iwaoko, H, Sugiyama, T and Inoue, Y. (1987). *United States Patent*, 4,700,136.